Aus dem Institut für Centrum für Schlaganfallforschung Berlin

der Medizinischen Fakultät Charité – Universitätsmedizin Berlin

DISSERTATION

Exploring Novel Magnetic Resonance Imaging Markers for Ischemic Stroke in the Application of Vessel Size Imaging and Amide Proton Transfer Imaging

zur Erlangung des akademischen Grades
Doctor of Philosophy (PhD)
im Rahmen des
International Graduate Program Medical Neurosciences

vorgelegt der Medizinischen Fakultät
Charité – Universitätsmedizin Berlin

von

Chao Xu

aus Hebei, China

Gutachter: 1. PD. Dr. med. Jochen B. Fiebach

2. Prof. Dr. rer. nat. habil. Harald E. Möller

3. Prof. Dr. rer. nat. Ingolf Sack

Datum der Promotion: 07.09.2012

Contents

List of Abbreviations

3D	three-dimensional
ADC	apparent diffusion coefficient
AIF	arterial input function
APT	amide proton transfer
APTR	amide proton transfer ratio
ASL	arterial spin labelling
CA	contrast agent
CBF	cerebral blood flow
CBV	cerebral blood volume
CEST	chemical exchange saturation transfer
CSF	cerebrospinal fluid
DNR	diffusional narrowing regime
DSC	dynamic susceptibility contrast
DWI	diffusion-weighted imaging
EPI	echo planar imaging
FID	free induced decay
FLAIR	fluid attenuation inversion recovery
FLASH	turbo fast low angle shot
FWHM	full-width at half-maximum
GE	gradient echo
GM	gray matter
HEA	healthy tissue
IGR	infarct growth
INF	initial infarct
IPE	ischemic penumbra
IQR	interquartile range
MRA	magnetic resonance angiography

MRI	magnetic resonance imaging
MT	magnetic transfer
MTR	magnetic transfer ratio
MTT	mean transit time
MVD	microvessel density
NMR	nuclear magnetic resonance
OLI	oligemic area
PI	perfusion imaging
ppm	parts per million
RF	radio frequency
RD	relative dispersion
ROC	receiver operating characteristic
ROI	region of interest
SAR	specific absorption rate
SDR	static dephasing regime
SE	spin echo
SNR	signal-to-noise ratio
ssCE-MRI	steady-state susceptibility contrast-enhanced magnetic resonance imaging
T_E	echo time
T_I	invention time
Tmax	time to reach the maximum
TOAST	trial of Org 10172 in acute stroke treatment
TOF	time-of-flight
t-PA	tissue plasminogen activator
T_R	repetition time
TTP	time to the peak
VOI	voxel of interest
VSI	vessel size index
WM	white matter

Chapter 1

Introduction

Stroke is a life-threatening disease that causes 9% of all deaths around the world [1]. About 87% stroke is caused by ischemia [1], which can be treated with the thrombolytic therapy within a narrow time window to restore the blood perfusion [2–4]. This treatment requires an accurate patient selection due to the risk of causing haemorrhage [5]. Therefore, developments of diagnostic methods for locating the ischemic region and assessing the severity are of great interest in stroke research.

Since introduced in 1973 [6], magnetic resonance imaging (MRI) has become one of the most important imaging techniques in modern radiology due to its non-invasive and non-radioactive methodology. Its usage in acute stroke management has widely and rapidly increased during the last decades due to its capability of early detection of ischemic lesions in multiple modalities, such as perfusion imaging (PI) [7] and diffusion-weighted imaging (DWI) [8]. Nowadays, clinicians employ the PI-DWI mismatch [9–12] to approximate the ischemic penumbra, which is the tissue at risk of infarction but still being salvageable [13]. However, this mismatch concept is challenged by the recoverable acute diffusion lesion and the overestimation of the ischemia in PI [14–17].

Two MRI techniques have been recently reported to provide novel imaging markers in the brain: 1) vessel size imaging, estimating the microvessel density (MVD) [18] and the mean vessel size [19, 20]; 2) amide proton transfer (APT) imaging, providing a pH-weighted contrast [21]. Both of them demonstrate the potential in describing pathologies of cerebrovascular diseases. However, neither of them has so far been utilized in the clinical stroke application.

Given that ischemia is a complex and multi-factored process, pathological changes of the microvasculature and the metabolic mechanism are expected in the ischemic tissue [22–24]. Therefore, this work aims at the development of vessel size imaging and APT imaging in clinical stroke application, as well as the evaluation of the corresponding imaging markers for penumbra description.

This thesis is structured in five parts:

In the first part **Background and Motivation**, principal concepts of MRI, which are involved in this study, are covered in Chapter 2. Fundamental knowledge of ischemic stroke, such as its causes, classification and pathophysiology is introduced in Chapter 3. The current stroke MRI techniques, as the powerful diagnostic tool to identify the ischemic penumbra, are reviewed in Chapter 4 according to the on-going 1000Plus study performed in our imaging center (Center for Stroke Research Berlin at the Campus Benjamin Franklin of the Charité University Hospital Berlin). Chapter 5 addresses the motivation of this work for a better description of the ischemic penumbra.

The second part **Vessel Size Imaging** describes first the state of the art of this technique in Chapter 6. Chapter 7 demonstrates the feasibility of this technique in clinical acute stroke studies by applying it in healthy subjects and a small patient cohort. The contribution of this technique in ischemic stroke research is evaluated in a group study in Chapter 8.

The third part **New Concept on Dynamic Susceptibility Contrast Imaging** demonstrates an extended work about an observation during the study of vessel size imaging, which is a hysteresis loop formed by the dynamic changes of transverse relaxation rates during the passage of the contrast agent (CA) bolus through the vasculature. This observation is introduced in Chapter 9. The formation of the loop is studied in Chapter 10 by simulating nuclear magnetic resonance (NMR) signals in a vascular tree model. To characterize the shape and the direction of the loop, Chapter 11 proposes an imaging marker and demonstrates its potential usage in cerebrovascular diseases.

The other novel imaging technique **Amide Proton Transfer Imaging** is introduced in the fourth part. The background of this technique, as well as its limitation in clinical application, is described in Chapter 12. The development of a pulse sequence with embedded field map and its preliminary application in subacute stroke patients are demonstrated

in Chapter 13.

The final part **Summary and Outlook** summarizes the current work in Chapter 14 and gives an outlook of further research topics in Chapter 15.

Part I

Background and Motivation

Chapter 2

Magnetic Resonance Imaging

MRI is a medical imaging technique used in radiology to visualize detailed internal structures by making use of the property of NMR to image nuclei of atoms inside the body. In this chapter, we briefly introduce the fundamental concepts of the NMR [25, 26] and the basic MRI sequence schemes [27, 28] to cover the background knowledge of MRI referenced in the following chapters. We note that the NMR physics introduced in this chapter is based on the classical Bloch formalism without including the interpretation in quantum mechanics.

2.1 Fundamental Concepts of Nuclear Magnetic Resonance

NMR is a physical phenomenon in which magnetic nuclei in a magnetic field absorb and re-emit electromagnetic radiation. In the biological tissue with large content of water molecules, the NMR of the protons in hydrogen atoms (^{1}H) contributes to the contrast of MRI.

2.1.1 Proton Spins and Magnetization

A proton spinning around its axis results in an intrinsic magnetic dipole moment $\vec{\mu}$. It also interacts with an external magnetic field $\vec{B_0}$ to experience the precession about the

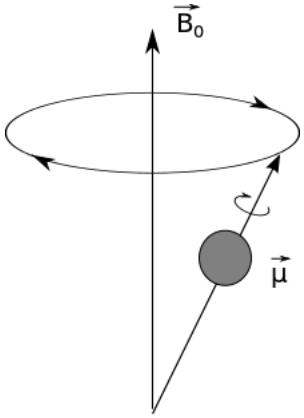

Figure 2.1: By definition, precession is the circular motion of the axis of rotation of a spinning body about another fixed axis caused by the application of a torque in the direction of the precession. The interaction of the proton's spin with the magnetic field produces the torque, causing it to precess about $\vec{B_0}$ as the fixed axis. Figure is modified from [28].

direction of the field (see Fig. 2.1). The precession angular frequency for the proton magnetic moment is given by

$$\omega_0 = \gamma B_0, \tag{2.1}$$

where ω_0 is referred to as the Larmor frequency, and γ is the constant named as the gyromagnetic ratio. The hydrogen proton in water has a γ of 2.68×10^8 rad/s/T, which results in a Larmor frequency of 127.8 MHz for a 3 T magnetic field. The magnetic moment vector for a spin aligns in either parallel (lower energy) or anti-parallel (higher energy) direction along the external magnetic field due to thermal energy kT, where k is the Boltzmann's constant and T is the absolute temperature. The number of spins in a parallel alignment exceeds that in an anti-parallel alignment with a fraction of $\hbar\omega_0/2kT$ in the total number of spins in the sample. Here, $\hbar \equiv h/(2\pi)$ is in terms of the Planck's quantum constant h. Although the fraction of spin excess is in the order of one in millions, it is enough to achieve a significant magnetization $\vec{M}$ per unit volume as the composition of all the spin moment vectors as

$$\vec{M} = \frac{1}{V} \sum_i \vec{\mu_i} \tag{2.2}$$

in a macroscopic sample size V because of the large abundance of spins in biological tissue. For a sample with a spin density of ρ_0, the longitudinal equilibrium magnetization M_0

along the external field $\vec{B_0}$ direction is given by

$$M_0 = \frac{\rho_0 \gamma^2 \hbar^2}{4kT} B_0. \tag{2.3}$$

2.1.2 Relaxation

Similar to the effect of the gravitational field on a spinning top, the torque on a macroscopic magnetization $\vec{M}$ due to an external magnetic field $\vec{B}$ follows the differential equation

$$\frac{d\vec{M}}{dt} = \gamma \vec{M} \times \vec{B}, \tag{2.4}$$

if no interaction between spins and the neighbourhood environment is considered. Eq. (2.4) can be separated into two decoupled equations for a longitudinal magnetization component M_z parallel to the external magnetic field $\vec{B}$ and a transverse magnetization component $M_\perp$ in the plane perpendicular to $\vec{B}$:

$$\frac{dM_z}{dt} = 0, \tag{2.5}$$

$$\frac{d\vec{M}_\perp}{dt} = \gamma \vec{M}_\perp \times \vec{B}. \tag{2.6}$$

Interactions of protons with their neighbourhood lead to additional terms in Eq. (2.4), which are discussed as follows.

Introduction of T_1

A macroscopic magnetization $\vec{M}$ that has been tilted by a radio frequency (RF) pulse in a static field will return to its macroscopic statistical equilibrium M_0. This process is called "spin-lattice relaxation". Nuclei held within a lattice structure are in constant vibrational and rotational motion, creating a complex magnetic field. The magnetic field caused by thermal motion of nuclei within the lattice is called the lattice field. The lattice field of a nucleus in a lower energy state can interact with nuclei in a higher energy state, causing the energy of the higher energy state to distribute itself between the two nuclei. Therefore, the energy gained by nuclei from the RF pulse is dissipated as increased vibration and rotation within the lattice, which can slightly increase the

temperature of the sample. The rate of change of the longitudinal magnetization M_z can be characterized by a empirically-determined constant referred as the longitudinal relaxation rate R_1. Its inverse $T_1 \equiv 1/R_1$ is the experimental longitudinal relaxation time. So the component M_z in Eq. (2.5) takes the form of

$$\frac{dM_z}{dt} = \frac{1}{T_1}\left(M_0 - M_z\right), \tag{2.7}$$

where M_0 is the equilibrium magnetization.

Introduction of T_2

The mechanism that the transverse magnetization $M_\perp$ decays towards its equilibrium value of zero due to the dephasing of spins is called "spin-spin relaxation". The same mechanism that is active in spin-lattice relaxation is active for spin-spin relaxation. Additionally, spins interact with each other through coupling or chemical exchange. During the spin-spin relaxation, the individual spins dephase with time and thus reduce the net magnetization vector. The rate of reduction in transverse magnetization is characterized by another experimental parameter R_2, referred to as the transverse relaxation rate. Its inverse $T_2 \equiv 1/R_2$ is named as the transverse relaxation time. The differential equation in terms of the transverse magnetization $M_\perp$ is changed by the addition of term with a transverse relaxation time as

$$\frac{d\vec{M}_\perp}{dt} = \gamma\vec{M}_\perp \times \vec{B} - \frac{1}{T_2}\vec{M}_\perp. \tag{2.8}$$

Introduction of T_2^* and T_2'

In practice, there are additional dephasing mechanisms affecting the transverse relaxation in biological tissue. First, spins at different positions in a sample may experience different field strength. The magnetic field inhomogeneity can be either due to a variation of the static magnetic field, or induced by biological tissue structures, such as blood vessels and nerve fibres. This decay is principally reversible by RF rephasing if spins stay within the same scale of field strength before and after the RF refocusing. On the other hand, spins may diffuse to other places in a magnetic gradient field. This decay is irreversible since

it is impossible to restore the position of spins.

The decay of magnetization affected by field inhomogeneity and diffusion is characterized by a rate R_2'. So the total effective relaxation rate, defined as R_2^*, is the sum of the spin-spin interaction relaxation rate and the additional relaxation rate as

$$R_2^* = R_2 + R_2'. \tag{2.9}$$

Its inverse $T_2^* \equiv 1/R_2^*$ takes the form of

$$\frac{1}{T_2^*} = \frac{1}{T_2} + \frac{1}{T_2'}. \tag{2.10}$$

Bloch Equation

The differential Eqs. (2.7) and (2.8) can be combined into one vector equation as

$$\frac{d\vec{M}}{dt} = \gamma \vec{M}_\perp \times \vec{B} + \frac{1}{T_1}\left(M_0 - M_z\right)\hat{z} - \frac{1}{T_2}\vec{M}_\perp, \tag{2.11}$$

which is referred to as the Bloch equation. For a constant field case $\vec{B} = B_0\hat{z}$, the corresponding solutions in a rotation frame about z-axis with the Larmor frequency are

$$M_z(t) = M_z(0)e^{-t/T_1} + M_0\left(1 - e^{-t/T_1}\right), \tag{2.12}$$

$$M_\perp(t) = M_\perp(0)e^{-t/T_2}. \tag{2.13}$$

2.2 Imaging Techniques

2.2.1 Gradient Echo and T_2^*

The simplest MRI experiment can be done by the application of a 90° RF pulse to rotate the longitudinal magnetization M_0 into the transverse plane and the measurement of the induced signal decay. This experiment is called the free induced decay (FID).

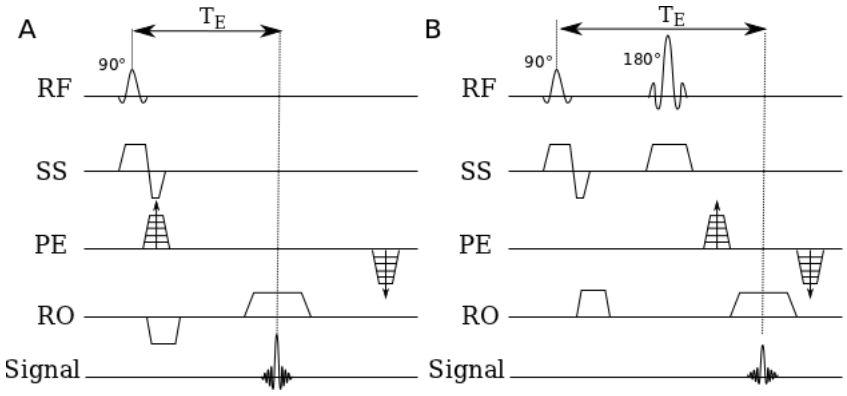

Figure 2.2: Sequence schemes of basic (A) gradient echo (GE) and (B) spin echo (SE) sequences. T_E indicates the echo time; RF, radio-frequency pulse; SS, slice selection; PE, phase encoding; RO, readout.

According to Eq. (2.13), the recorded signal in the rotation frame takes the form of

$$M_{\perp}(t) = M_0 e^{-t/T_2^*}. \tag{2.14}$$

We note that the relaxation is characterized by T_2^* rather than T_2, since magnetic field inhomogeneities affect the decay in practice.

A gradient echo (GE) is generated by using a pair of bipolar gradient pulses. In Fig. 2.2A, the basic GE sequence is illustrated. The data are sampled during a GE, which is achieved by dephasing the spins with a negatively pulsed gradient before they are rephased by an opposite gradient with opposite polarity to generate the echo. Essentially, the signal acquired corresponds to the FID, as the echo producing gradients only compensate for the applied imaging gradients.

In an MRI experiment, the scheme in Fig.2.2A is played repeatedly to acquire multiple lines in k-space with an interval of repetition time (T_R), so that the start magnetization for FID from the second T_R on is $M_0\left(1 - e^{-T_R/T_1}\right)$ instead of M_0. Therefore, the magnetization vector contributing to the GE is

$$M_{\perp}(T_E) = M_0\left(1 - e^{-T_R/T_1}\right) e^{-T_E/T_2^*}, \tag{2.15}$$

where T_E is the echo time. For a long T_R (relative to T_1) and T_E comparable with T_2^*, the image is weighted by both spin density and T_2^*. The contrast between tissues with different T_2 is enhanced. For a sequence with such parameter settings, we call it

T_2^*-weighted imaging. Its usage in stroke research is introduced in Section 4.2.2.

2.2.2 Spin Echo

A spin echo (SE) sequence is illustrated in Fig. 2.2B. The 90° excitation pulse rotates the longitudinal magnetization into the xy-plane and the dephasing of the transverse magnetization $M_\perp$ starts. The following application of a 180° refocusing pulse generates signal echoes. The purpose of the 180° pulse is to rephase the spins, causing them to regain coherence and thereby to recover the transverse magnetization, producing an SE.

A multiple SE experiment (e.g. Carr-Purcell-Melboom-Gill sequence [29, 30]) applying multiple 180° pulses after a single 90° pulse can be a way to approach the intrinsic T_2, if the refocusing is effective over the whole sample and the irreversible dephasing caused by spatial diffusion of spins is minimized. This condition is hard to achieve since it requires the exact performance of RF pulses and the minimized inter-echo time. Therefore, the measured SE relaxation time T_{2SE} is shorter than the intrinsic T_2 and depends on the sequence parameters used in the experiment.

2.2.3 Inversion Recovery

The inversion recovery experiment produces imaging contrasts sensitive to T_1. The application of an initial 180° inversion pulse before a basic GE or SE sequence (see Fig. 2.3) rotates the longitudinal magnetization first into the negative $\hat{z}$ direction, so that M_z starts with a negative of the equilibrium value

$$M_z(0) = -M_0. \tag{2.16}$$

The inversion time (T_I) is defined as the time between the inversion pulse and the 90° excitation pulse. The magnetization regrows to its equilibrium value in the interval of T_I according to Eq. (2.12)

$$M_z(t) = M_0\left(1 - 2e^{-t/T_1}\right), \text{ when } 0 < t < T_I. \tag{2.17}$$

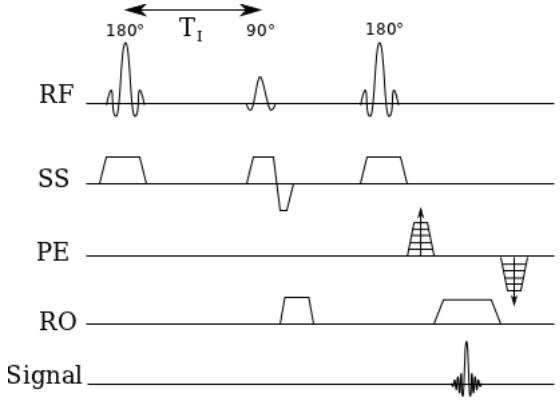

Figure 2.3: The diagram of inversion recovery sequence. RF indicates the radio frequency pulses; SS, slice selection; PE, phase encoding; RO, readout; T_I, inversion time.

After the longitudinal magnetization is tipped into the transverse plan to provide the initial signal, the magnitude of the transverse magnetization evolves as

$$M_{\perp}(t) = \left|M_0\left(1-2e^{-T_I/T_1}\right)\right| e^{-(t-T_I)/T_2}, \text{ when } t > T_I. \tag{2.18}$$

We note that the factor $\left|M_0\left(1-2e^{-T_I/T_1}\right)\right|$ is zero if T_I is selected as

$$T_I = T_1 \ln 2. \tag{2.19}$$

For a uniform sample, T_1 can be precisely measured by varying T_I to achieve a zero in signal.

2.3 Magnetic Properties of Tissue and Contrast Agents

The magnetic susceptibility χ is an intrinsic property of a material, which is the degree of magnetization of a material in response to a magnetic field. Susceptibility variations in body tissue and exogenous CAs can be useful in contributing imaging contrasts in MRI.

All materials have induced dipole moments in the presence of external magnetic fields. The electrons pair up to cancel their spin magnetic moments. This effect is called diamagnetism. The macroscopic sum of the induced moments is roughly anti-parallel to the external magnetic field, so that its associated macroscopic field weakly opposes the external field. The susceptibility is negative $\chi < 0$ for diamagnetic materials.

An atom with an unpaired electron has a non-vanishing permanent magnetic moment with an associated non-zero dipole magnetic field. Those atom moments in a material would tend to align with an external magnetic field, producing a bulk magnetic moment and a corresponding macroscopic magnetic field augmenting the external field. This effect is referred to as paramagnetism, which is a much stronger effect than diamagnetism. The susceptibility is positive $\chi > 0$ for paramagnetic materials.

Metal ions show a suitable paramagnetic effect which depends on the number of unpaired electrons in the ion. The Fe^{3+} and Gd^{3+} ions are suitable candidates for a relaxation agent, since their electron-spin relaxation time matches the Larmor frequency of the protons (about 10^{-8} - 10^{-10} s). A deoxyhemoglobin molecule consisting of a Fe^{3+} ion with unpaired electrons is paramagnetic and is served as an endogenous CA in functional blood-oxygen-level dependence imaging [31]. Since free Gd^{3+} ions are extremely toxic, they are bound into a chelate complex in intravenous CAs for clinical use.

Paramagnetic CAs affect the MRI contrast in two ways: dipolar relaxation effects and susceptibility induced relaxation effects [32].

In the former process, the relaxation of tissue is enhanced by the dipole-dipole interaction between the free electron spins of the paramagnetic ion in a CA molecule and the proton spins in water [33]. A linear relationship between the CA concentration and the increase in relaxation rates [34, 35] can be defined in terms of the relaxivity of the CA as

$$R_1 = R_1^0 + r_1 C, \tag{2.20}$$

$$R_2 = R_2^0 + r_2 C, \tag{2.21}$$

where R_1^0 and R_2^0 are the relaxation rates without the presence of the CA, r_1 and r_2 are the relaxivity constants of the CA, and C is the molar concentration of the CA.

The latter process can be understood as the magnetic field inhomogeneity induced by a paramagnetic CA. The induced magnetic field $\vec{B_i}$ of a material in an external magnetic field $\vec{B_0}$ is

$$\vec{B_i} = (1 + \chi)\vec{B_0}. \tag{2.22}$$

Therefore, a paramagnetic CA with a susceptibility change $\Delta\chi$ compared to the surrounding tissue will induce a local field difference of $\Delta B = \Delta\chi B_0$. This leads to a shift

of Larmor frequency

$$\Delta\omega = \gamma\Delta\chi B_0, \tag{2.23}$$

and thus shortens T_2/T_2^* with a consequent dephasing of spins during the transverse relaxation.

Chapter 3

Ischemic Stroke

A stroke is the rapidly developing loss of brain functions due to the disturbance in the blood supply to the brain, and causes 9% of all deaths around the world as the second most common cause of death after ischemic heart disease [1]. Stroke can be either ischemic or haemorrhagic (see Fig. 3.1). Ischemic strokes are those that are caused by interruption of the blood supply, while haemorrhagic strokes are the ones which result from the rupture of a blood vessel or an abnormal vascular structure. About 87% of strokes are caused by ischemia [1]. In this chapter, we review the fundamental knowledge of ischemic stroke, such as its causes, classification and pathophysiology.

3.1 Causes and Classification

Cerebral ischemia is a restriction of the blood supply to the brain, leading to the dysfunction and death of the brain tissue. The restriction of the blood can be thrombosis or embolism.

The thrombosis is the obstruction of a blood vessel by a thrombus forming locally in an artery directly leading to the brain. The thrombosis can arise from the large vessels (e.g. the internal carotid artery, the vertebral artery and the circle of Willis), or the small arteries inside the brain (e.g. branches of circle of Willis and middle cerebral artery, and the arteries arising from the distal vertebral and basilar artery) [36]. In rare cases, the thrombosis originates from the dural venous sinuses, where the thrombus is formed due to the locally increased venous pressure exceeding the pressure generated by the

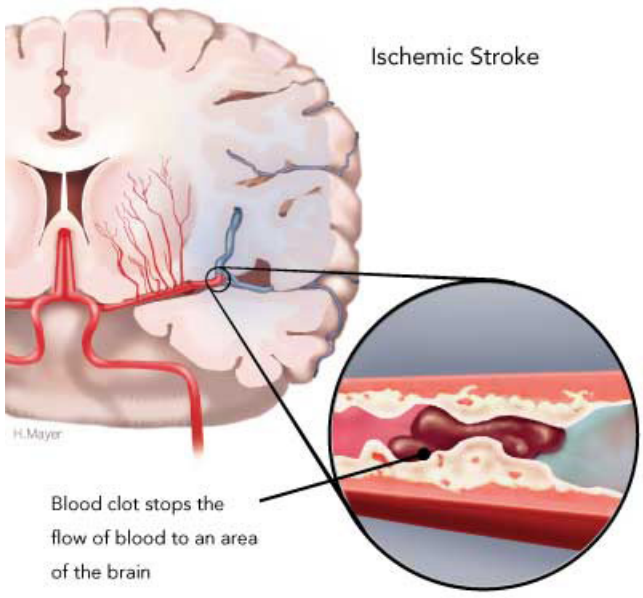

A ©Heart and Stroke Foundation of Canada

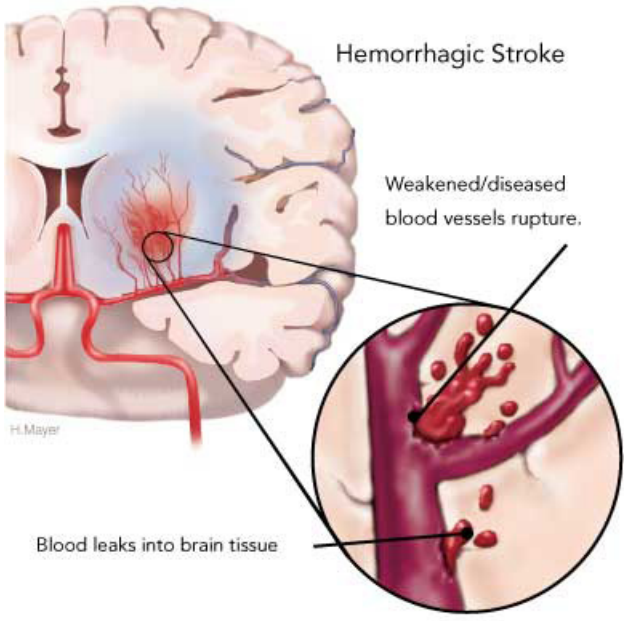

B ©Heart and Stroke Foundation of Canada

Figure 3.1: Subtypes of stroke: (A) ischemic and (B) haemorrhagic stroke. (A) Ischemic stroke is caused by the interruption of blood flow to the brain due to a clot, which stops the flow of the blood to the tissue. The shortage of oxygen and nutrients results in tissue damage. (B) Haemorrhagic stroke is caused by the rupture of a blood vessel or an abnormal vascular structure. Blood leaks into brain tissue and causes the cell death. Images are from the Heart and Stroke Foundation of Canada.

arteries [37, 38].

The embolism is the blockage of an artery due to an embolus travelling in the arterial bloodstream originating from elsewhere of the body, most commonly from the heart. Emboli of cardiac origin are a frequent cause of large brain infarcts and haemorrhagic brain infarcts with often initial severe symptoms [39]. On the other hand, the embolism linked with the system hypoperfusion is associated with less severe clinical deficits. The borderzone infarction between the territories of two major arteries is often seen in this case [40].

The trial of Org 10172 in acute stroke treatment (TOAST) classification based mainly on the aetiology differentiates cerebral ischemia into large-artery atherosclerosis from embolus or thrombosis, cardioembolism, small-vessel occlusion, stroke of other determined aetiology and stroke of undetermined aetiology [36]. This classification aids clinicians to monitor the prognosis, the outcome and the management of stroke patients [41–43].

3.2 Pathophysiology

The reduction of blood flow and energy supply to the brain during ischemia triggers several mechanisms, which lead to cell death. The evolution of these pathophysiological processes spreads from hours to days (Fig. 3.2) and mediates the injury of neurons, glial cells and microvessels [23].

The first consequence of perfusion deficit is the depletion of oxygen and glucose, which causes the accumulation of lactate via anaerobic glycolysis. The acidosis modifies the activity of antioxidant enzymes, enhances the free-radical formation and worsens the brain injury by triggering the inflammation and the apoptosis [44–46].

Energy failure on Na^+/K^+ -ATPase and Ca^{2+}/H-ATPase pumps leads to the elevation of intracellular Na^+, Ca^{2+} and Cl^- and the increase of extracellular K^+ [47]. This leads to the loss of the osmotic pressure and the cytotoxic edema consequently. The loss of the membrane potential results in the depolarization of neuron and glia. The excitotoxic amino acids, especially glutamate, are discharged into the extracellular space, which harm the neurons and cause the necrosis [23].

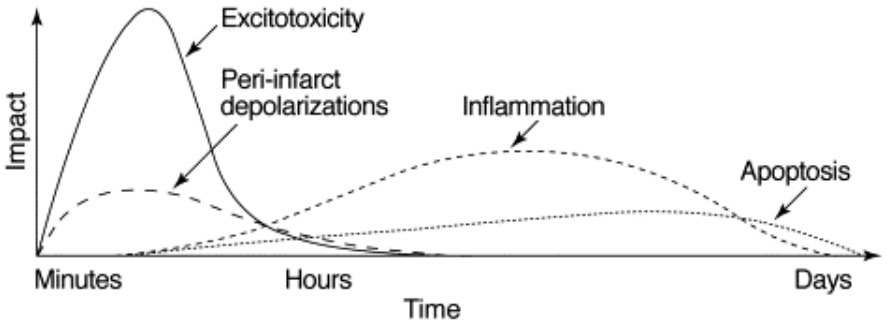

Figure 3.2: Putative cascade of damaging events in focal cerebral ischemia. Very early after the onset of the focal perfusion deficit, excitotoxic mechanisms can damage neurones and glia lethally. In addition, excitotoxicity triggers a number of events that can further contribute to the demise of the tissue. Such events include peri-infarct depolarizations and the more-delayed mechanisms of inflammation and programmed cell death. The x-axis reflects the evolution of the cascade over time, while the y-axis aims to illustrate the impact of each element of the cascade on final outcome. The figure is from [23].

Within minutes of occlusion, there occurs the upregulation of proinflammatory genes, which produces mediators of inflammation. After the expression of adhesion molecules at the vascular endothelium, neutrophils transmigrate from the blood into the brain parenchyma, followed by macrophages and monocytes [48]. Whereas the microvascular obstruction by neutrophils can worsen the degree of ischemia, production of toxic mediators by activated inflammatory cells and injured neurons can amplify tissue damage [49].

All the pathological processes mentioned above trigger the apoptosis, which occurs particularly in the tissue with milder ischemic injury, defined as ischemic penumbra (see Section 4.1). The apoptotic process can last for days after the ischemia onset and is mediated by two general signal pathways involving either the disruption of mitochondria or the activation of death receptors located on the plasma membrane [50].

Apart from the neuron injury, microvessels undergo the mechanical or hypoxic damage of vascular endothelium. Toxic damage of inflammatory molecules and free radicals, the destruction of the basal lamina by matrix metalloproteinases, and the compression of swollen astrocytic end-feet are potential causes of microvessel obstruction and blood-brain-barrier disruption during ischemia [24, 51].

Chapter 4

Stroke Magnetic Resonance Imaging

The delineation of ischemic penumbra from normal tissue and infarction at the acute stage is of great importance for targeting the patients for therapy and thus is the main focus of stroke imaging research. MRI techniques provide not only the early detection of ischemic lesion with high sensitivity, but also the capability of imaging the lesion with multi-modalities. Therefore, its usage has widely and rapidly increased in acute stroke management during the last decades. In this chapter, we review the concept of ischemic penumbra as an imaging diagnostic target and introduce the 1000Plus study performed in our imaging center, as well as the imaging sequences utilized in the protocols along this study.

4.1 Ischemic Penumbra

Within areas of severely reduced blood flow, which is termed as the core of the ischemic territory, excitotoxic and necrotic cell death occurs within minutes, and the tissue undergoes irreversible damage in the absence of prompt and adequate reperfusion [23]. However, cells in the peripheral zones are supported by collateral circulation, and their fate is determined by factors including the severity of ischemia and the timing of reperfusion. In this peripheral region, termed as the ischemic penumbra, cell death occurs relatively slowly. This region is considered to be potentially salvageable [52]. However, the extent of penumbral tissue diminishes rapidly with time, thus the therapeutic time window is narrow [53]. The thrombolytic therapy, which is the intravenous tissue plasminogen acti-

vator (t-PA), currently restricts the treatment window to 4.5 hours [54], since the delayed therapy increases the risk of haemorrhage [55]. The identification of ischemic penumbra for a better patient selection is thus of great importance in stroke research.

The most relevant definition of ischemic penumbra for clinical practice is based on neuroimaging techniques. With the modern MRI techniques, the PI identifies the brain tissue with reduced blood perfusion and the DWI locates the severe ischemic core [10–12, 56]. The PI-DWI mismatch regions indicate the ischemic penumbra, which serves as the target for thrombolytic therapy. Several clinical trials (the DIAS [57] and the DEDAS trial [58]) employing MRI to select patients on the basis of the PI-DWI mismatch have shown that patients treated in an extended time window have significantly higher rates of reperfusion and improved 90th day clinical outcome.

On the other hand, this mismatch concept is challenged by the observation that the DWI lesion may not be restricted to the infarct core [59] and the perfusion deficit often overestimates the final infarction [17, 60]. Furthermore, the definition of mismatch region is complicated by the selection of perfusion parameters [61], processing methods [62] and delineation thresholds [63–65]. Further investigations are certainly needed for profiling the mismatch concept. The on-going 1000Plus study performed in our stroke imaging center was designed to validate the PI parameter for infarct prediction and is introduced in the following Section 4.2.

Moreover, given that the ischemic tissue damage is complex and multi-factorial [23, 24], novel imaging markers can augment existing penumbral imaging and provide great insights into disease pathophysiology and perhaps, if validated, serve to help guide treatment decisions.

4.2 1000Plus Study

The 1000Plus study is an on-going trial designed as a prospective, single center observational study conducted by our stroke imaging center to describe the incidence of mismatch and the predictive value of PI for final lesion volume depending on door-to-imaging time and vascular recanalization [66].

4.2.1 Study Design

The study aims to include 1200 patients and cover their MRI examinations from the acute stroke onset to one-week follow-ups. The inclusion criteria and study design are shown in Fig. 4.1.

All the examinations are performed with a 3 T MRI scanner (Tim Trio; Siemens AG, Erlangen, Germany). Our MRI protocol for acute stroke patients contains the following sequences for the day of admission (day 1) and day 2: T_2^*-weighted imaging to screen for intracerebral haemorrhage; DWI to assess cerebral infarction; time-of-flight magnetic resonance angiography (TOF-MRA) to detect vessel occlusion; fluid attenuation inversion recovery (FLAIR) to estimate microangiopathic lesions load and to investigate the age of the recent lesion; PI to determine the tissue at risk. On day 5 - 7, a third measurement with a shorter protocol excluding PI is performed to assess the final infarct size on FLAIR. An example of images obtained along the examination protocols is illustrated in Fig. 4.2.

Each imaging technique involved in the 1000Plus study is described in detail as follows.

4.2.2 T_2^*-weighted Imaging

T_2^*-weighted imaging uses a basic GE sequence with a T_E between the longest and shortest tissue T_2 of interest and a long T_R compared to T_1. According to

$$M_\perp(T_E) = M_0 \left(1 - e^{-T_R/T_1}\right) e^{-T_E/T_2^*}, \tag{2.15}$$

the contrast between tissue with different T_2^*s is enhanced. The T_2^*-weighted contrast is sensitive to susceptibility changes. The haemorrhage appears dark in T_2^*-weighted image due to the ferric iron deposition (see Fig. 4.2 on day 2 and day 6). The T_2^*-weighted imaging is performed in priority of other scans for exclusion of patients with bleeds for the thrombolytic therapy.

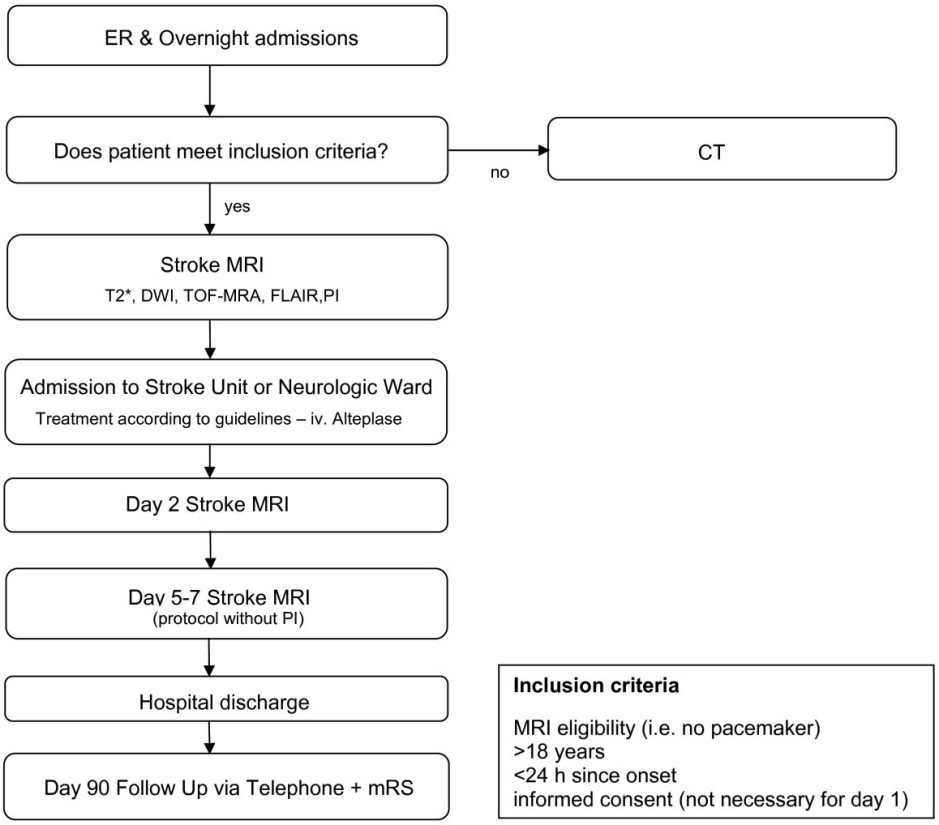

Figure 4.1: Study design and inclusion criteria of the 1000Plus Study. The figure is from [66]. ER indicates emergency room; CT, computer tomography; MRI, magnetic resonance imaging; DWI, diffusion-weighted imaging; TOF-MRA, time-of-flight magnetic resonance angiography; FLAIR, fluid attenuation inversion recovery; mRS, modified ranking scale to assess functional recovery in randomized stroke trials.

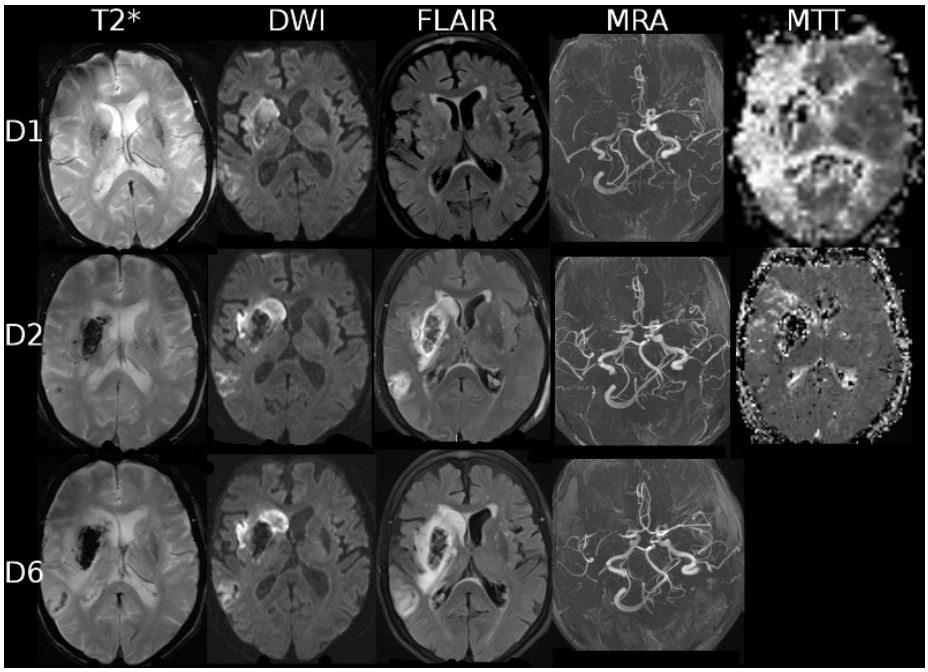

Figure 4.2: Example of images from a patient (female, 85 years) included in the 1000Plus study. The patient had a right middle cerebral artery infarct, M1 artery occlusion and perfusion imaging (PI) - diffusion-weighted imaging (DWI) mismatch on day 1, haemorrhagic transformation in the infarction on day 2, and increased infarction volume on day 6. FLAIR indicates fluid attenuation inversion recovery; MRA, magnetic resonance angiography; MTT, mean transit time; D1, first day after symptom onset; D2, second day after symptom onset; D6, sixth day after symptom onset.

4.2.3 Time-of-Flight Magnetic Resonance Angiography

The TOF-MRA enables the delineation of the vessel lumen by using the blood flow effects [67]. The blood flow is assumed to be perpendicular to the imaging plane or volume in the case of a three-dimensional (3D) study. For T_R shorter than the T_1 of the stationary spins within the slice, the signal will be reduced due to partial saturation effects. Blood flow in the vessel will move spins from outside the slice which have not been subjected to the spatially selective RF pulses into the imaging slice. These unsaturated or fully relaxed spins have full equilibrium magnetization, and therefore upon entering the slice will produce a much stronger signal than stationary spins assuming that a GE sequence is applied. This effect is referred to as inflow enhancement [68]. A 3D reconstruction is performed to extract the vessel lumen from the plane images [69].

4.2.4 Fluid Attenuation Inversion Recovery

The FLAIR pulse sequence is a derivative of the inversion recovery sequence illustrated in Fig. 2.3. The 180° inversion pulse is attached prior to the 90° excitation pulse of an SE acquisition, so that the longitudinal magnetization rotates into the negative plane after the inversion pulse. According to Eq. (2.18), the transversal magnetization $M_\perp$ recorded at the time of T_E is

$$M_\perp(T_E) = \left| M_0 \left(1 - 2e^{-T_I/T_1}\right) \right| e^{-(T_E - T_I)/T_2}, \tag{4.1}$$

where T_I is the inversion time. According to Eq. 2.19, the effects of the fluid from the resulting image can be removed by selecting an appropriate T_I as

$$T_I = T_{1CSF} \ln 2, \tag{4.2}$$

where T_{1CSF} is the T_1 of the cerebrospinal fluid (CSF). The $M_\perp$ of the CSF in Eq. (4.1) is nulled.

This technique suppresses the signal of fluid, which appears very bright in a normal T_2 contrast. Therefore, the lesions adjacent to the cerebral cortex and ventricles, which are normally covered by the CSF signal, are visible by the dark fluid technique. The FLAIR

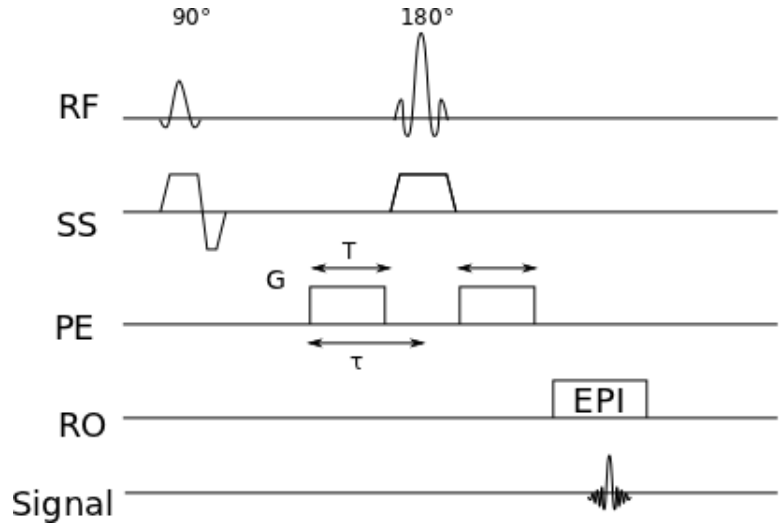

Figure 4.3: The diagram of an SE diffusion imaging sequence with the diffusion gradient (amplitude, G; duration, T) added in the phase-encoding direction. RF indicates the radio frequency pulses; SS, slice selection; PE, phase encoding; RO, readout; EPI, echo planar imaging.

sequence is widely used in detecting lesions with a long T_2, for example, the vasogenic edema surrounding a brain tumour [70, 71] and multiple sclerosis plaques [72] within the periventricular white matter. In stroke imaging, FLAIR images are used to identify the final infarction (see Fig. 4.2 on day 6).

4.2.5 Diffusion-weighted Imaging

The diffusion imaging sequence is able to measure the signal attenuation from the molecular motion in a certain direction by adding diffusion gradients to a basic sequence [73]. An example of the SE diffusion imaging sequence measuring the diffusion in the phase-encoding direction is shown in Fig. 4.3 with the gradient amplitude of G and the duration of T. According to the diffusion theory, the protons following the random walk will bring the signal decay as

$$S(G) = S(0)e^{-bD}, \tag{4.3}$$

where $S(G)$ is the MRI signal intensity with the amplitude of the diffusion gradient G, $S(0)$ is the MRI signal density without performing the diffusion gradient, and D is the diffusion coefficient. The gradient configuration factor b is defined as

$$b = 2\gamma^2 T^2 G^2 (\tau - T/3), \tag{4.4}$$

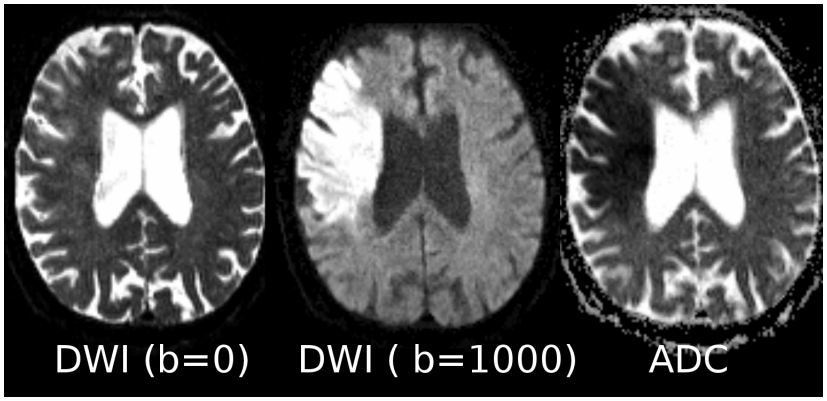

Figure 4.4: Image modalities of diffusion imaging techniques in a stroke patient (female, 73 years) with right middle cerebral artery infarct. DWI indicates diffusion-weighted imaging; ADC, apparent diffusion coefficient; b, a gradient configuration factor described in Eq. (4.4) with the unit of s/mm^2.

where γ is the gyromagnetic ratio, and τ is the time from the start point of the diffusion gradient to the centerline of refocusing RF pulse.

Hence, the different coefficient $D(x, y)$ in a certain direction (x, y) is obtain from a slope fitting as following:

$$D(x, y) = -\frac{1}{b} \ln \frac{S(x, y, G)}{S(x, y, 0)}, \tag{4.5}$$

where the $S(x, y, G)$ indicates a diffusion-weighted signal in the direction of (x, y). In our imaging center, diffusion gradients were performed in six different directions with $b = 1000$ s/mm^2 and $b = 0$ s/mm^2 (Fig. 4.4). The magnitude of the vector $\vec{D}$ is conventionally named as the apparent diffusion coefficient (ADC).

As described in Section 3.2, the membrane pumps become short of energy and stop functioning within minutes of ischemia. Osmotic pressure is consequently lost between the extracellular fluid and the cytoplasm. This results the movement of water from the extracellular space to the cells, which get swelling. The extracellular motion of water molecules is restricted due to the shortage of the extracellular space. This leads to a reduction of the ADC. Therefore, the ADC enables an early detection of the ischemic region, which appears a dark area in the ADC map (Fig. 4.4). Clinicians often employ diffusion-weighted images for lesion identification, since the ischemia is more recognizable as a clearly demarcated hyperintensity.

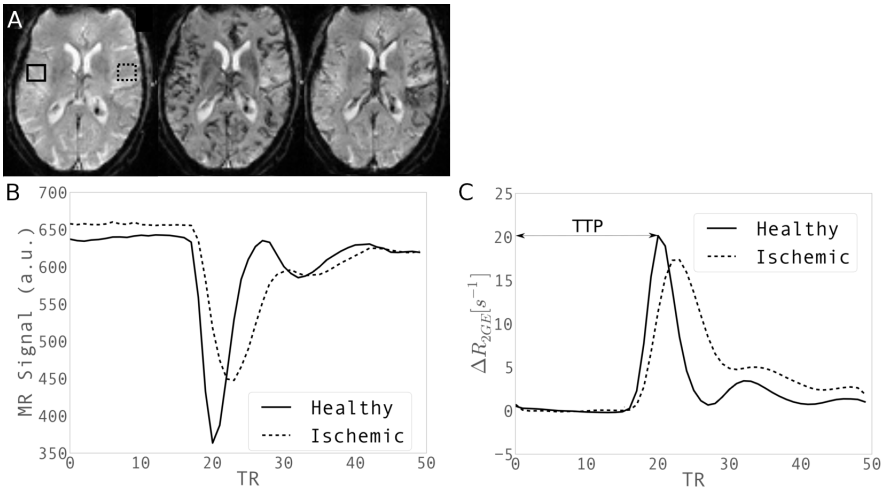

Figure 4.5: Illustration of process method in perfusion imaging in a patient (male, 78 years) with left internal carotid artery occlusion measured 20 hours after symptom onset. (A) Three echo planar imaging (EPI) images demonstrate the contrast change before, during, and after the bolus passage. (B) The curve of the signal intensity for comparison between the region of ischemic tissue and the contralateral healthy tissue. (C) The ΔR_2 curve and the definition of the parameter time to the peak (TTP).

4.2.6 Perfusion Imaging

In our imaging center, the dynamic susceptibility contrast (DSC) imaging is used to quantify the hemodynamic perfusion. It requires the injection of a bolus of the CA and employ a dynamic GE echo planar imaging (EPI) sequence to track the susceptibility-induced signal loss during the bolus passage through the brain (Fig. 4.5A) [74].

The change in transverse relaxation rate measured by GE ΔR_{2GE} is converted from the raw MRI signal $S(t)$ according to

$$\Delta R_2(t) = -\frac{1}{T_E} \ln \frac{S(t)}{S_0}, \tag{4.6}$$

where T_E is the echo time and S_0 is the baseline signal without CA injection.

According to Eq. (2.21), a linear dependence between the the change of transverse rate and the concentration of the CA inside the tissue $C_t(t)$ is assumed, so that

$$\Delta R_{2GE} = rC_t(t), \tag{4.7}$$

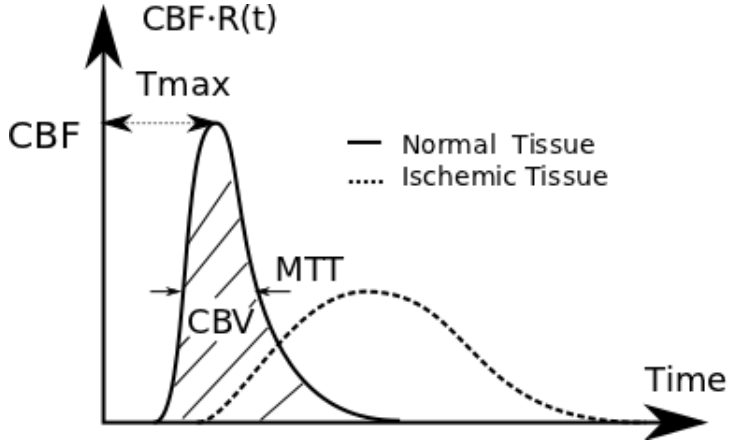

Figure 4.6: Illustration of the definition of perfusion parameters. CBV indicates cerebral blood volume; CBF, cerebral blood flow; MTT, mean transit time; Tmax, time to reach the maximum.

where r is the relaxivity of the CA. The ΔR_{2GE} curve can present as the scaled tracer-concentration curve, on which the time to the peak (TTP) is defined as the time from the starting point of the measurement to the peak of the curve (Fig. 4.5C).

If we know the arterial input function (AIF) to the brain $C_i(t)$, which is manually or automatically selected from a voxel or from the averaged curve of several voxels, the tissue impulse response curve $R(t)$ can be calculated by deconvoluting $C_i(t)$ from the tracer-concentration curve $C_t(t)$ according to

$$C_t(t) = f \cdot C_i(t) \otimes R(t), \tag{4.8}$$

where f is the cerebral blood flow (CBF) [75]. Several perfusion parameters are defined on the scaled tissue impulse response curve $R(t)$ after the deconvolution (see Fig. 4.6). The CBF is the maximum of the curve. The area under the curve is defined as cerebral blood volume (CBV). The time to reach the maximum (Tmax) shows the delay. The ratio between CBV and CBF is defined as mean transit time (MTT). The ischemic tissue demonstrate a decreased CBV and CBF, and a prolonged MTT and Tmax (Fig. 4.7), because the vessel blockage causes a delay and dispersion in blood transportation.

All these parameters have been evaluated by clinicians to delineate the penumbra. However, issues on the selection [61], the processing methods [62] and the delineation thresholds [63–65] of these perfusion maps are still under debate.

Besides the DSC imaging, another perfusion imaging technique, named arterial spin

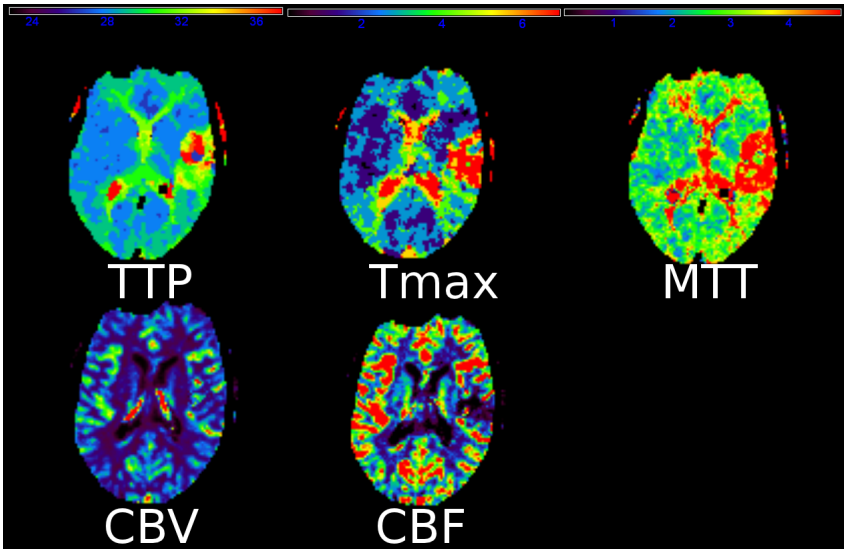

Figure 4.7: Perfusion maps of the patient shown in Fig. 4.5. TTP indicates time to the peak; Tmax, time to reach the maximum; MTT, mean transit time; CBV, cerebral blood volume; CBF, cerebral blood flow.

labelling (ASL), is also capable of the CBF estimation by using the endogenous CA, which is the magnetically labelled protons within water molecules in arterial blood before flowing to the imaged portion of the brain [76]. It measures the signal attenuation dependent upon the rates of the labelled spin flowing into the voxel and compares the contrast with a baseline image without labelling. Although ASL offers advantages over the CA injection and a potential absolute measurement of CBF, its intrinsic technical limitations causing a lower signal-to-noise ratio (SNR), longer measurement time and less resistance to patient motion compared to the DSC measurements restrict its current usages in acute stroke diagnosis [77–79].

Chapter 5

Motivation

An important focus of imaging research in the ischemic stroke is the differentiation of the ischemic penumbra from the infarct core and the normal tissue. Especially in patients presenting beyond the established time window of 4.5 hours after the stroke, in candidates for endovascular treatment, and in patients older than 80 years, a precise characterization of brain ischemia is required [80]. The mismatch between ischemic areas measured by PI and DWI has been considered to be a good approximation of the ischemic penumbra, yet it tends to overestimate it by containing regions of benign oligemia [17, 60] (Fig. 5.1). The overestimation afflicts the clinical routine as the final infarct volume is not predicted by the acute PI-DWI mismatch [11, 81]. Therefore, despite its widespread use at present, the PI-DWI mismatch is not a complete approach for imaging the penumbra [82–84]. As the thrombolytic therapy is accompanied by a considerable risk of haemorrhage, it is necessary to develop complementary imaging modalities that can characterize the ischemic penumbra in more detail.

Cerebral microvessels, which include capillaries, arterioles, and venules, express multiple dynamic responses to ischemia together with their neighbouring neurons [22]. The effects of ischemia on the microvasculature have so far mainly been described from the functional aspect [51, 85]. Because various vasomodulators are involved in this process [86–88], changes in microvascular morphology are apparently expected. Therefore, we hypothesize that the morphological variation of the microvascular network under ischemic conditions could be an effective way to describe the pathology of ischemic tissue and might provide useful information for describing the ischemic penumbra.

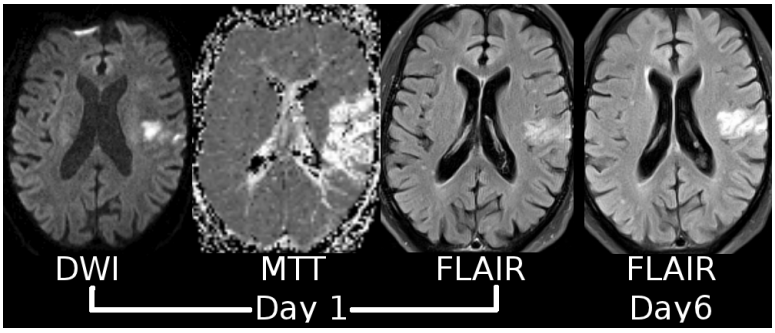

Figure 5.1: The acute perfusion imaging (PI) - diffusion-weighted imaging (DWI) mismatch on day 1 overestimates the final infarction on day 6 in a patient (male, 78 years, left internal carotid artery occlusion, without recanalization). MTT indicates mean transit time; FLAIR, fluid attenuation inversion recovery.

Considering different orders between the common clinical imaging resolution in millimeters and microvascular scale of micrometers, there is no way to image the microvascular network directly. Parameters reflecting properties of the local microvascular network in the imaging scale are used instead. Vessel size imaging, which provides a measure of MVD and a mean vessel size, was proposed as a novel approach to map the cerebral microvascular structure quantitatively [19]. Attempts have been made to apply this technique in animals stroke models [89, 90] and tumour patients [20, 91].

In this thesis, we aim to integrate vessel size imaging in clinical stroke study and evaluate the parameters provided by this technique in ischemic tissue.

As described in Section 3.2, the restriction of blood supply causes the immediate accumulation of lactate, which leads to the ischemic acidosis, i.e. a decrease in pH. The acidic environment modifies the activity of antioxidant enzymes, enhances the free-radical formation and causes the cell death. Therefore, tissue pH value may serve as an important physiological marker for the easy detection of the tissue at risk.

Although the lactate magnetic resonance spectroscopy is able to assess the tissue acidosis *in vivo* [92], its spatial resolution is not yet appropriate for mapping the acute stroke patients. Recently, Zhou et al. [21] has proposed a technique, named amide proton transfer (APT) imaging, to differentiate the pH value by detecting the chemical exchange process between the amide protons in the mobile proteins and the protons in the water. This technique has so far demonstrated decreased pH values in the ischemic tissue of stroke rat brain [21, 93]. However, its usage is limited in clinical stroke studies due to

the strict time and the safety restriction of patient management.

As the second focus of our work, an APT imaging sequence is designed and implemented in the clinical scanner to overcome the technique limitation, and is applied to a pilot group of patients.

Part II

Vessel Size Imaging

Chapter 6

Vessel Size Imaging - State of the Art

Vessel size imaging was proposed as a novel approach to quantitatively map the cerebral microvascular morphology via introducing two quantities [19]: (1) the MRI-measured MVD Q which correlates to histological estimates; (2) the vessel size index (VSI) which is an averaged radius of all the microvessels contained within a voxel. It shows great potentials in characterizing the microvascularature in cerebrovascular diseases. This chapter provides an overview of this approach in state of the art, which includes the analytical modelling, mathematical definition of Q and VSI, the imaging techniques and the applications in both animal and clinical studies.

6.1 Theory

6.1.1 Transverse Relaxation in Brain Tissue

The NMR effective transverse relaxation with the characteristic relaxation time T_2^*, is the process by which the component of the nuclear magnetization perpendicular to the external magnetic field B_0 returns to the equilibrium distribution. The transverse relaxation is a complex phenomenon, which consists of processes in several scopes.

First, the spin-spin interaction of protons in water molecules, and if a paramagnetic CA

is administrated, the interaction of proton spins from water molecules and electron spins of the CA, cause a very fast relaxation with a characteristic time in the order of 10^{-12} s. This process is generally referred as "microscopic", since the acting distance is very short, which is in the order of molecule size. This is generally referred to as the T_2 relaxation, which is a irreversible relaxation and does not depend on the pulse sequence.

Additional relaxation mechanisms generally characterized by a relaxation time T_2' can be further divided in two scopes: macrosopic and mesoscopic. The gradients of the magnetic field across over the samples cause a "macrosopic" process, which is pulse-sequence dependent and completely reversible. On the other hand, the magnetic gradients induced by the susceptibility difference between the tissue compartments, such as plasma and erythorocytes in blood, and intra- and extravascular space in the tissues, result in a "mesoscopic" relaxation, which acts over the distance comparable to a vessel or a cell size, and has a characteristic time of tens of milliseconds. The mesoscopic relaxation is partially reversible to the susceptibility gradients and depends strongly on the sequence T_E, which is in the magnitude of the characteristic time of mesoscopic dephasing.

For a sample with macroscopic magnetic field homogeneity, the transverse relaxation measured by a GE and an SE depends highly on the mesoscopic tissue structure. Both Monte Carlo simulation and analytical modelling of a mono-sized vessel distribution with a fixed blood volume fraction have suggested that, the transverse relaxation rates measured by the GE and the SE, R_{2GE} and R_{2SE}, respectively, depend on the vessel size in a different manner (see Fig. 6.1).

The GE signal is constant at large radii since the spatial pattern of the Larmor frequency shift can be rescaled following the increased vessel size. The SE attenuation is determined by the gradients of the field induced by the vessels over the diffusion length of water molecules. The fact that these gradients are smaller for larger vessels explains the vanishing relaxation for large radii. This makes it possible to estimate the averaged vessel size in a vessel distribution by using the transverse relaxation rates measured by SE and GE.

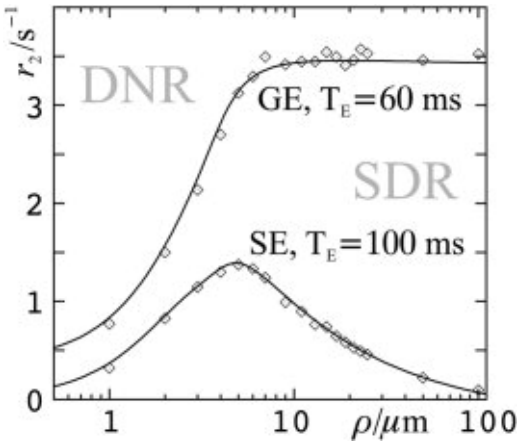

Figure 6.1: Transverse relaxation rates r_2 as a function of the radius ρ of a monosized vessel population for gradient echo (GE) and spin echo (SE) measurements with echo time (TE) of 60 ms and 100 ms, respectively. The points show the result of a Monte Carlo simulation. The simulation parameters are: magnetic field strength, 1.5 T; blood fraction, 2 %; magnetic susceptibility of the blood, 10^{-7}. DNR indicates diffusional narrowing regime; SDR, static dephasing regime. The results are from [94].

6.1.2 Tissue Model

We consider a tissue voxel in which the vasculature is formed by a large number of small voxels and does not contain any large vessels. This voxel is modelled with two compartments: blood in vessels occupying a volume fraction ζ and brain parenchyma. The vascular network consists of three types of vessels: arterioles, capillaries and venules with the volume fractions of ζ_a, ζ_c, and ζ_v, respectively. The vessel distribution with a radius ρ in blood type α occupies a volume fraction $\zeta_\alpha(\rho)$ and obeys the normalization condition:

$$\int_0^\infty \zeta_\alpha(\rho) d\rho = \zeta_\alpha, \tag{6.1}$$

where α labels the three blood types: $\alpha = a, c, v$. Hence, the total blood volume fraction is the sum of the three contributions:

$$\zeta = \zeta_a + \zeta_c + \zeta_v. \tag{6.2}$$

The blood in vessels is considered as a homogeneous medium with the magnetic susceptibility χ, which consists of two contributions:

$$\chi = \chi_0 + \chi_1, \tag{6.3}$$

where χ_0 is the native susceptibility of the blood, which is zero in arterioles, non-zero in venules, and interpolates between the two pools in capillaries. The χ_1 is the susceptibility induced by the presence of the CA.

6.1.3 Signal Calculation

In either SE or GE experiments, the total NMR signal s from the voxel takes the form of the combination of the intravascular signal s_i and the extravascular signal s_e weighted by their volume fraction

$$s = \zeta s_i + (1 - \zeta) s_e. \tag{6.4}$$

The intravascular signal is a sum from three blood pools and can be replaced as

$$\zeta s_i = \sum_{\alpha} \zeta_\alpha s_{i\alpha}, \tag{6.5}$$

where s_{ia} is the signal contribution in blood type α. The signal from the blood in arterial or venous pool s_{ia} and s_{iv} follows the exponential decay as

$$s_{i\alpha} = \exp\left[-\left(R_{2\alpha 0} + rC_\alpha\right) T_E\right], \tag{6.6}$$

where $\alpha = a$ or v, and T_E is the echo time. The R_{2a0} and R_{2v0} are the relaxation rate in arterial and venous blood without the CA, respectively, which are taken from *in vitro* measurements. The term rC_α describes the relaxation induced by the CA with the concentration of C_α, where r is the relaxivity of the CA. The signal from the capillary pool s_c is calculated by a linear interpolation of the relaxation rate between the arterial and venous ends. This yields

$$s_c = \zeta_c \frac{\exp(-R_{2a0}T_E) - \exp(-R_{2v0}T_E)}{(R_{2v0} - R_{2a0})T_E} \exp[-rC_cT_E]. \tag{6.7}$$

The extravascular signal in Eq. (6.4) is contributed by two exponential relaxations as

$$s_e = \exp[-(R_{2p0} + R_{2p})T_E], \tag{6.8}$$

where R_{2p0} is the rate of relaxation in parenchyma caused by the spin-spin interactions

at the molecular scale, which can be measured with the Carr-Purcell-Meiboom-Gill sequence. In turn, the relaxation rate R_{2p} in the extravascular space is caused by the susceptibility effects of vessels, which take the form of the sum of relaxivity in each vessel levels:

$$R_{2p} = \int d\rho \zeta_\alpha(\rho) r_{2\alpha}, \tag{6.9}$$

where $r_{2\alpha}$ are functions to characterize the relaxivities of a vessel with a given type α and radius ρ. These functions are vessel-specific, since the relaxation effect depends on two parameters: 1) the diffusion time across the vessel $t_D = \rho^2/D$, where D is the diffusion coefficient; 2) the characteristic shift of the Larmor frequency on the surface of the vessel $\omega = 2\pi\chi\gamma B_0$, where γ is the gyromagnetic ratio, B_0 is the magnetic field strength, and χ is the magnetic susceptibility of the blood as a combination of the susceptibility contributed by the CA and the one of natural blood depending on its type α.

The dephasing mechanism of nuclear magnetization described by $r_{2\alpha}$ depends crucially on the value of the typical phase acquired by water protons when a water molecule diffuses past a vessel, ωt_D. Dephasing falls in the so-called diffusional narrowing regime (DNR) [95] when this phase is small, $\omega t_D \ll 1$. This case can be realized as fast diffusion that results in an effective averaging of the inhomogeneous magnetic field induced by blood vessels. The averaging results in a small dephasing effect, which is nearly the same for the GE and SE amplitudes. The opposite limit, $\omega t_D \gg 1$, is commonly referred to as the static dephasing regime (SDR) [96, 97]. This case can be realized as slow diffusion such that the diffusion length $l_D = (DT_E)^{1/2}$ is short on the scale of magnetic field variations. The latter scale can be estimated to be in the condition of ωt_D larger than the vessel size ρ. This estimate is based on the following scenario of dephasing induced by a blood vessel. Spins, which are excited in a close vicinity of the vessel are rapidly dephased and do not contribute to the signal unless the echo time T_E is very short. In this way, an area with dephased magnetization is formed around the vessel and grows with time. The SDR takes place when the diffusion length l_D of water molecules is much shorter than the size of this area. This results in the above estimation. Spins outside this area experience a magnetic field, which is nearly constant within one T_E. This results in effective rephasing of nuclear magnetization in the SE acquisition, which is more effective when the vessels are larger.

The crossover between the two regimes at $B_0 = 1.5$ T takes place for dimensions in the order of the size of capillaries with the native magnetic susceptibility of blood χ_0 [98].

For a higher magnetic field, e.g. $B_0 = 3$ T, the crossover takes place for even smaller dimension. Moreover, the signal attenuation during the bolus passage is shifted toward the SDR due to the increase in susceptibility of χ. This justifies the restriction of the following analysis of vessel size imaging to the SDR.

6.1.4 Assessment of Vessel Size Index

Within the SDR frame, the GE relaxation rate remains constant while the SE relaxation decreases with the vessel size (see Fig. 6.1). For a long echo time, both $\omega T_E \gg 1$ and $\omega T_E/(\omega t_D)^{1/3} \gg 1$ are fulfilled. The relaxivity of a monosized vessel population shows different dependencies for the GE and the SE [95, 97]:

$$r_{2GE} = \frac{2}{3}\omega - \frac{1}{T_E} \qquad \text{for } \omega T_E \gg 1, \tag{6.10}$$

$$r_{2SE} = 0.6940\frac{\omega}{(\omega t_D)^{1/3}} - \frac{1}{T_E} \qquad \text{for } \frac{\omega T_E}{(\omega t_D)^{1/3}} \gg 1. \tag{6.11}$$

For a vessel population with blood volume distribution $\zeta(\rho)$, the relaxation rate changes from the introduction of a susceptibility distribution are

$$\Delta R_{2GE} = \frac{2}{3}\zeta\omega, \tag{6.12}$$

$$\begin{aligned}\Delta R_{2SE} &= 0.6940\int_0^\infty \left(\frac{D\omega^2}{\rho}\right)^{1/3}\zeta(\rho)d\rho \\ &\equiv 0.6940\zeta\left(\frac{D\omega^2}{\Re^2}\right)^{1/3},\end{aligned} \tag{6.13}$$

where $\Re$ is the mean vessel radius in the vessel population according to

$$\Re^{-2/3} = \frac{1}{\zeta}\int_0^\infty \rho^{-2/3}\zeta(\rho)d\rho. \tag{6.14}$$

The mean vessel radius is conventionally referred to as the VSI and can be determined from Eq. (6.12) and Eq. (6.13) given the measure values of ΔR_{2GE} and ΔR_{2SE}. The assessment of VSI can be written as

$$\text{VSI} = \Re = 0.867(\zeta D)^{1/2}\frac{\Delta R_{2GE}}{\Delta R_{2SE}^{3/2}}, \tag{6.15}$$

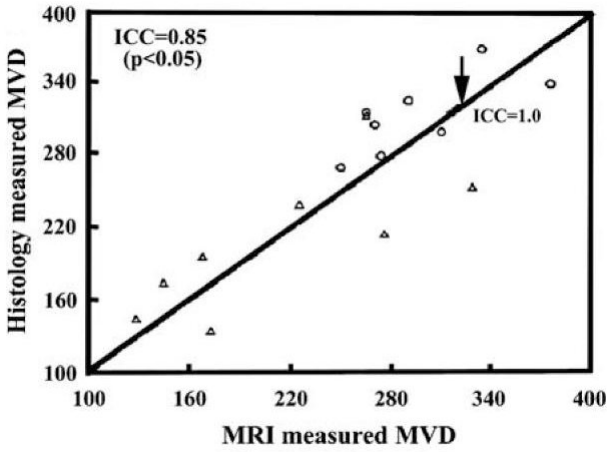

Figure 6.2: Excellent agreement between histological microvessel density (MVD) and magnetic resonance imaging (MRI)-measured MVD (Q^3) was observed (ICC = 0.85; 95% lower bound = 0.78). ICC indicates intraclass correlation coefficient. The figure is from [89].

where ζ as the blood volume fraction and D as the diffusion coefficient can be measured or predefined.

6.1.5 Microvessel Density Related Quantity Q

Given the fact that the mesoscopic effects of ΔR_{2GE} and ΔR_{2SE} are related to the microvascular structure, another quantity Q is proposed to correlate with the MVD and takes the form of

$$Q \equiv \frac{\Delta R_{2SE}}{\Delta R_{2GE}^{2/3}}. \tag{6.16}$$

Excellent agreement between the histological MVD and the cubic quantity Q^3 has been found in rat brains (see Fig. 6.2). This correlation can be written as

$$\text{MVD} = kQ^3 \tag{6.17}$$

with $k = 329$ s/mm^2 in mouse brain [99]. However, the k value in the human brain is so far not available. Jensen et al. [100] showed a possible way to calculate the lower and upper bounds of MVD *in vivo* by using Q. However, the lower and upper boundaries, which differ by two orders of magnitude, do not allow an accurate estimate of MVD. Therefore, Q served as the parameter indicating the relative change of MVD is used for *in vivo* imaging marker instead of a quantitative MVD.

We note that the ratio of $\Delta R_{2GE}/\Delta R_{2SE}^{3/2}$ in the definition of VSI is the fractional power of the Q. Thus, the VSI can be derived from Q as

$$\mathrm{VSI} = 0.867(\zeta D)^{1/2} Q^{-3/2}. \tag{6.18}$$

6.2 Imaging Techniques

The imaging technique for vessel size imaging, which requires both SE and GE measurements, has so far three implementations:

- Steady-state susceptibility contrast-enhanced MRI (ssCE-MRI), which performs the GE and SE measurements before and after the CA administration to derive the ΔR_{2GE} and ΔR_{2SE} from the CA residues [18]. This technique was used in most of studies because of its relatively low technical requirements. However, it requires a high dose of the CA to reach the steady state and does not allow CBV mapping due to the lack of tracking the dynamic bolus passage. The VSI qualification can only be achieved by additionally performing a blood test to define the contrast concentration.

- Dynamic bolus tracking by a special double-echo EPI sequence, which tracks the dynamic signal changes in both GE and SE contrasts with a time resolution around 2 s (see the sequence diagram in Fig. 6.3). The dynamic method enables the CBV evaluation, and thus is more suitable for clinical examination as a substitution of the standard PI measurement. However, this technique is so far not a standard installation in clinical scanners.

- Separate GE and SE acquisitions with dual injection of CA, which are a derivative method to record dynamic GE and SE changes when the double-echo EPI sequence is not available in the study group. Although this method may reach a higher imaging resolution than the double-echo implementation, the dual CA injections lead to a temporary misregistration and the CA residual dose between two time series.

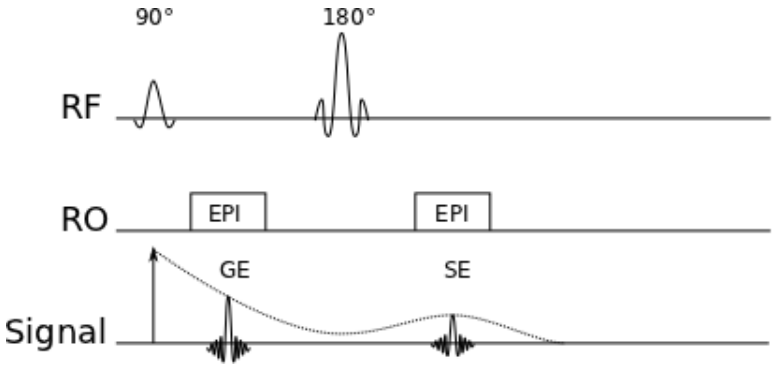

Figure 6.3: The diagram of double-echo echo planar imaging (EPI) sequence used for vessel size imaging. GE indicates gradient echo; SE, spin echo; RF, radio frequency pulse; RO, readout.

6.3 Applications

By means of the techniques mentioned in Section 6.2, vessel size imaging has been applied in both animal and human studies to map morphological properties of the microvasculature under both normal and pathological conditions.

Although the quantification of MVD in human by estimating Q is not possible due to the lack of intra-subject histological data, the lower- and upper-bound MVDs derived by Q were found to be in reasonable accordance with the previously cited values determined by histology [100]. The VSI of the normal-appearing tissue studied by Hsu et al. [91] and Kiselev et al. [20] showed an overestimate of vessel sizes, which may arise from the systemic overestimation of the modelling or the high CBV fraction scaling.

It has been reported that vessel size imaging can successfully characterize cerebral tumour vascularization with an elevated Q and a relatively stable VSI in both animal [101, 102] and human studies [20, 103]. This may help to monitor the metastatic angiogenesis and assess the vascular remodeling under antiangiogenic therapy.

Vessel size imaging has recently been applied to animal ischemic stroke models [89, 90]. Because of a much faster blood circulation in rodent models, these two studies used ssCE-MRI, which uses ΔR_{2GE} and ΔR_{2SE} before and after administration of an intravascular CA, and thus fails to provide the CBV evaluation and the VSI validation. The variation in vascular density has been reported in acute (day 1) and subacute (day 3 to 21) ischemia in rats with a focus on assessing angiogenesis. However, no data were presented in the hyperacute phase (< 4.5 hours), which is especially important for clinical diagnosis.

The application of vessel size imaging in clinical stroke studies is described in detail in the following Chapter 7 and Chapter 8.

Chapter 7

Feasibility of Vessel Size Imaging in Clinical Stroke Application

Despite the great potential of vessel size imaging in the assessment of pathological vascular morphology, dynamic vessel size imaging has not been so far applied in clinical stroke imaging because of its high technological requirement and extremely challenging execution of imaging acute stroke patients. Therefore, this chapter aims to adapt the technique of vessel size imaging for clinical stroke application. The imaging and post-processing methods are described here. The present work tests the feasibility of vessel size imaging in 9 healthy subjects and applies this technique in 13 patients with acute ischemic stroke to reveal the pathological microvascular morphology in the hyperacute stage.

7.1 Materials and methods

7.1.1 Healthy Volunteers and Patients

Nine healthy volunteers (female 5; mean age 28 years, age range 25 to 40 years) were recruited in compliance with the regulations of the local ethics committee.

From October 2009 to April 2010, 15 consecutive patients with acute stroke within a time window of 4.5 hours fulfilling the criteria of having middle cerebral artery, anterior cerebral artery, or posterior cerebral artery occlusion identified by MRA images were ex-

amined with the vessel size imaging protocol. In all, 13 patients had a PI-DWI mismatch and were included for further analysis. The clinical data of these 13 patients are listed in Table 7.1.

7.1.2 Imaging

All studies were performed using a 3 T clinical scanner (Tim Trio, Siemens AG, Erlangen, Germany). Vessel size imaging was performed with a hybrid single-shot GE and SE sequence with 50 repetitions (T_E(GE/SE) 22/85 ms; T_R, 1880 ms; field-of-view, 230 mm; slice thickness, 5 mm; slice number, 16; matrix size, 64×64). A dose of 0.13 mL Gadovist (Bayer Schering Pharma AG, Berlin, Germany) per kg body weight was injected at a speed of 5 mL/s with a time delay of 18 s. The ADC map was obtained from a six-directional DWI sequence with $b = 1000$ s/mm^2 performed before the vessel size imaging sequence. All the measurements in stroke patients were embedded into the existing clinical imaging routine without additional time extension [66].

7.1.3 Data Processing

Q calculation

As shown in Fig. 7.1A and B, the dynamic changes in relaxation rates ΔR_{2GE} and ΔR_{2SE} were converted from the exponential signal drops during the bolus passage, respectively, following

$$\Delta R_2(t) = -\frac{1}{T_E} \ln \frac{S(t)}{S_0}, \tag{4.6}$$

where T_E is the echo time, S_0 is the average baseline signal intensity before CA administration, and $S(t)$ is the signal intensity along the timeline.

According to

$$Q \equiv \frac{\Delta R_{2SE}}{\Delta R_{2GE}^{2/3}}, \tag{6.16}$$

Q was obtained by fitting the linear dependence between $\Delta R_{2SE}(t)$ and $\Delta R_{2GE}^{2/3}(t)$ by using the least-square procedure (see Fig. 7.1C).

Vessel size index calculation

ID	Age (years) /Sex	Time from symptom onset (hours)	Site of ischemia	NIHSS administration	NIHSS discharge	Recanali-zation	Acute MTT lesion volume [mL]	Acute DWI lesion volume [mL]
1	87/F	1.5	R/MCA	12	3	–	150.39	7.58
2	71/M	1.5	R/MCA	4	4	NA	57.15	4.5
3	75/M	4	R/MCA	2	1	–	44.6	0.14
4	74/M	2	R/PCA	2	1	+	30.69	0.04
5	79/F	1.5	L/MCA	18	16	NA	209.39	2.41
6	90/F	3	R/MCA	18	9	NA	199.21	50.02
7	71/M	3	R/MCA	5	4	+	77.26	0.65
8	86/F	1	L/MCA	5	0	+	53.73	4.05
9	62/M	1	R/MCA	13	0	+	96.26	2.85
10	77/F	3	R/MCA,ACA	20	20	+	79.97	54.9
11	87/F	1.5	R/MCA	6	2	+	29.57	0.01
12	89/F	1.5	L/MCA	14	13	NA	141.53	1.09
13	55/M	2	L/MCA	3	0	+	190.4	0.37
Median (IQR)	77 (71 - 87)	1.5 (1.5 - 3)	–	6 (4 - 14)	3 (1 - 9)	–	79.97 (53.73 - 150.39)	2.41 (0.37 - 4.5)

Table 7.1: The clinical data in 13 acute stroke patients. F indicates female; IQR, interquartile range; L, left; M, male; MCA, middle cerebral artery; MTT, mean transit time; NA, no follow-up examination was available; NIHSS, national institutes of health stroke scale; R, right; +, recanalization happened in the follow-up examination; –, no recanalization.

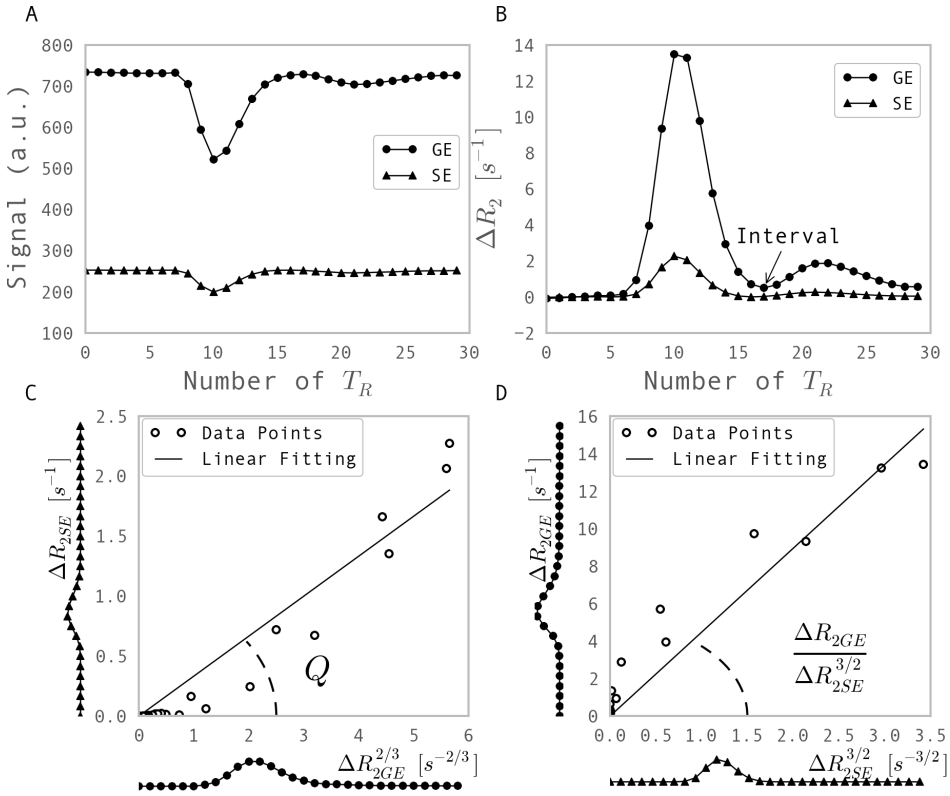

Figure 7.1: Illustration of the calculation of Q and VSI. (A) The dynamic signal measured by a gradient echo (GE) and a spin echo (SE) during bolus passage. (B) Signal intensities are converted into relaxation rates ΔR_{2GE} and ΔR_{2SE}. (C) Q is calculated as the slope obtained from linear fitting of data points on the ($\Delta R_{2GE}^{2/3}$, ΔR_{2SE}) plane. (D) The ratio $\Delta R_{2GE}/\Delta R_{2SE}^{3/2}$ is calculated as the slope obtained from linear fitting of data points on the ($\Delta R_{2SE}^{3/2}$, ΔR_{2GE}) plane, and used to calculate VSI.

The VSI map was calculated by

$$\mathrm{VSI} = 0.867(\zeta D)^{1/2}\frac{\Delta R_{2GE}}{\Delta R_{2SE}^{3/2}}, \tag{6.15}$$

where ζ and D are the CBV and the ADC, respectively.

Similar to the calculation of Q, the ratio of $\Delta R_{2GE}/\Delta R_{2SE}^{3/2}$ was obtained by fitting the linear dependence between $\Delta R_{2GE}(t)$ and $\Delta R_{2SE}^{3/2}(t)$ (see Fig. 7.1D).

The ADC maps from the diffusion measurement were coregistered to the baseline SE images by using SPM8 (Welcome Department of Imaging Neuroscience, University College London, London, UK). The dynamic $\Delta R_{2GE}(t)$, which is proportional to tracer concentration $C_t(t)$, i.e. $\Delta R_{2GE}(t) \propto C_t(t)$ according to Eq. (4.7), was used to calculate the CBV map [75]. The CBV can be determined from area under the tissue impulse response curve $R(t)$:

$$CBV = \int_0^\infty R(t) \cdot dt. \tag{7.1}$$

It is well known in perfusion theory that tracer-concentration curve $C_t(t)$ is the tissue response to the AIF:

$$C_t(t) = f \cdot C_i(t) \otimes R(t), \tag{4.8}$$

where f is the CBF, $\otimes$ indicates convolution, and $C_i(t)$ is the AIF.

In this study, AIFs were selected manually in the M3 segment at the top of the ventricle contralateral to the suspected ischemia to yield a relatively high SNR [104]. The deconvolution of $R(t)$ from Eq. (4.8) was accomplished in Fourier domain by applying the Tikhonov regularization with a control parameter optimized according to the voxel-wise baseline SNR as $\lambda = 10^{3.7}/\mathrm{SNR}^{2.7}$ by the following equation:

$$R(\omega) = \frac{1}{CBF} \cdot \frac{C_t(\omega)C_i^*(\omega)}{C_i(\omega)C_i^*(\omega) + \lambda^2\omega^4}, \tag{7.2}$$

where $R(\omega)$, $C_t(\omega)$, and $C_i(\omega)$ are the transformation of $R(t)$, $C_t(t)$, and $C_i(t)$ in Fourier domain, respectively, and $C_i^*(\omega)$ is the conjugate of $C_i(\omega)$ [105]. Finally, CBV was normalized to a global average in the healthy tissue of 3% [106] and used in Eq. (6.15) to derive VSI.

7.1.4 Regions of Interest Selection

For each healthy volunteer, the regions of interest (ROIs) of gray matter (GM) and white matter (WM) were generated from probability maps by using the segmentation method in SPM8, with the probability value being higher than 0.5. The ROIs of thalamus were manually drawn on pre-processed SE images. For each stroke patient, DWI lesion was manually delineated by a human rater masked to other images. The derived ROI was then mapped to ADC images to ensure ADC hypointensities (ADC < 0.7 μm^2/ms) and exclude the false-positive region automatically. The MTT > 5.3 s was set to be the initial threshold for hypoperfused tissue [107]. The selected MTT ROI was corrected manually to exclude areas that were not part of a credible perfusion deficit. An example from patient 8 is shown to illustrate the procedures to generate ROIs in Fig. 7.2. All the ROIs and postprocessed maps were normalized to the standard space to derive two spatially symmetric hemispheres. The ROI of the ischemic tissue, i.e. the tissue at risk, was defined as the subtracted region MTT minus DWI ROI. The ischemic ROI was then mirrored to the contralateral region with normal tissue. The ischemic and mirrored ROI were superimposed on normalized Q and VSI maps for evaluation.

7.1.5 Statistical Analysis

The Shaprio-Wilk test confirmed that Q and VSI in both ischemic ROI and contralateral mirrored ROI did not follow the normal distribution. Therefore, median and full-width at half-maximum (FWHM), rather than mean value and standard deviation, were used to characterize the voxel distribution in each patient, as well as in healthy subjects. The median and the FWHM of VSI and Q in patients between ROIs were tested by Wilcoxon's signed-rank test (n = 13).

7.2 Results

The histogram of voxel-wise Q and VSI values gathered from nine healthy subjects in three selected ROIs of GM, WM, and thalamus are shown in Fig. 7.3.

The Q is higher in GM and thalamus than in WM, i.e. higher MVD is observed in GM

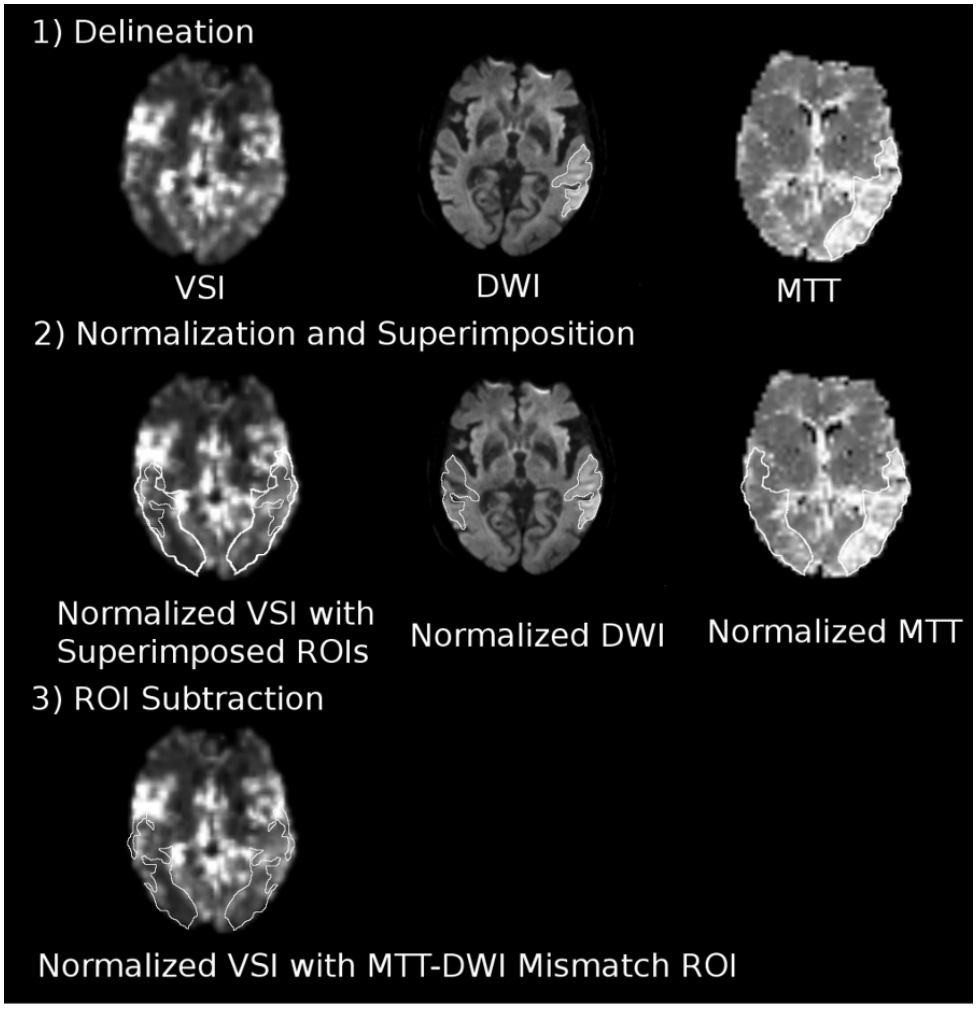

Figure 7.2: Procedures to generate the ischemic and mirrored regions of interest (ROIs). Images are taken from patient 8. (1) Diffusion-weighted imaging (DWI) and mean transit time (MTT) ROIs are delineated while masked to other images. (2) DWI, MTT, and vessel size index (VSI) maps, as well as ROIs derived from step 1, are normalized to the standard brain with two spatially symmetric hemispheres. Normalized DWI and MTT ROIs are mirrored to the contralateral hemisphere. Both pairs of symmetric ROIs were superimposed on normalized VSI maps. (3) The area corresponding to MTT ROI minus DWI ROI is defined as the ischemic tissue. Its mirrored ROI is placed in the contralateral hemisphere with normal tissue.

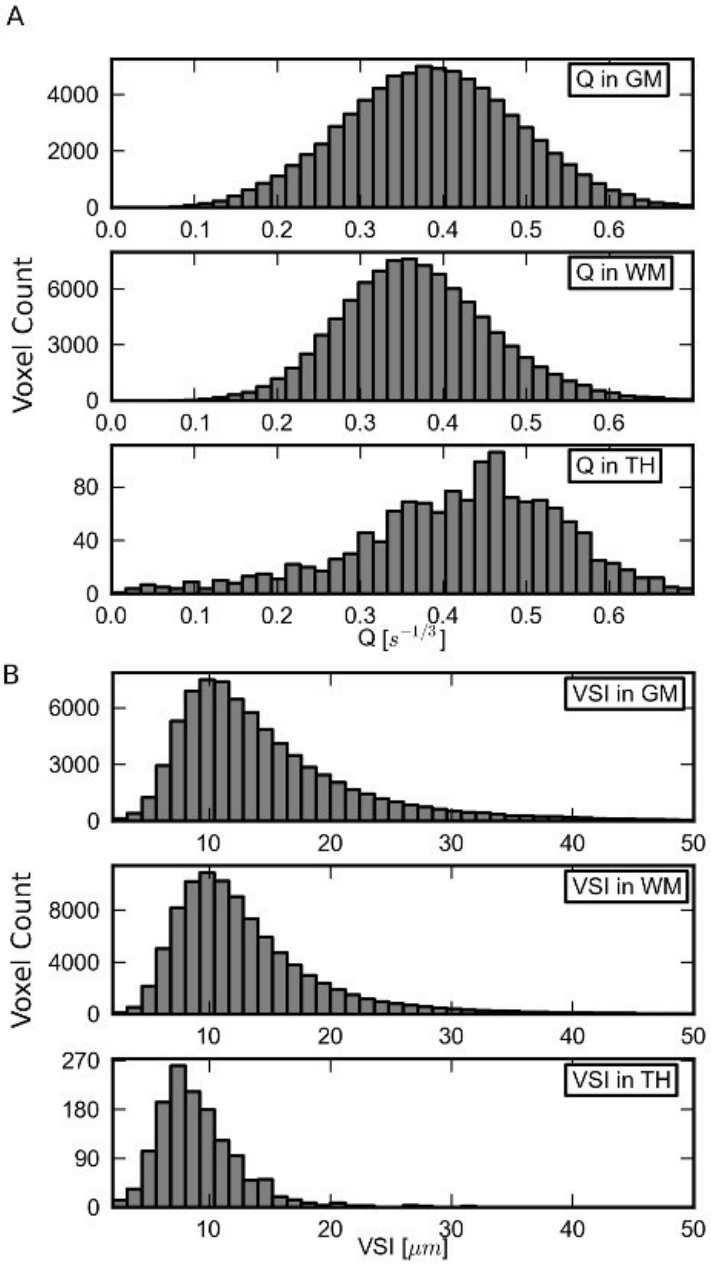

Figure 7.3: Histograms of (A) Q and (B) vessel size index (VSI) values in voxels gathered from nine healthy subjects in the regions of interest of gray matter (GM), white matter (WM), and thalamus (TH).

and thalamus than in WM, according to the linear dependency of MVD and Q^3. Similar vessel sizes are observed in GM (median, 13.8 μm; FWHM, 12.4 μm) and WM (median, 13.1 μm; FWHM, 10.7 μm). In the thalamus with the absence of large vessels, smaller VSI (median, 9.1 μm; FWHM, 8.1 μm) is found.

Fig. 7.3 illustrates the median and the FWHM of Q and VSI distribution in each patient in the ischemic area and its mirrored ROI in the contralateral hemisphere. An elevated median VSI value has been detected in the ischemic tissue compared with the contralateral region (n =13, $p < 0.05$). Changes in the median of Q between ischemic and mirrored ROI are rather heterogeneous. Predominantly reduced median Q (the change of value from the ischemic ROI to the mirrored ROI $> 10\%$) in the ischemic region is found in 2 of 13 patients, whereas the median of Q in the remaining 11 patients does not show an obvious change. The FWHM of the distribution in ischemic tissue is increased in VSI (n = 13, $p < 0.05$) and decreased in Q (n = 13, $p < 0.05$).

Different pathological responses of the microvascular structure to the ischemia seem to emerge. In 11 of the 13 patients (patients 1 to 11), with a typical example shown in Fig. 7.5, the Q map appears rather homogeneous, whereas the hyperintensities on the VSI map are observed in the perfusion deficit. Consistent with the maps, the shape of the Q-value histogram in the hypoperfused region displays no obvious changes compared with the mirrored area, whereas the peak of the VSI histogram in the ischemia shifts toward larger values. In the remaining two patients (patients 12 and 13), hypointensities on the Q map and hyperintensities on the VSI map are shown in the perfusion lesion (see the example in Fig. 7.6). The Q histogram in the ischemic region shifts toward smaller values, whereas the VSI histogram becomes broader and moves toward larger values.

Follow-up results of MRA were available for 8 of the 13 patients and showed recanalization in 6 patients. In the subgroup of patients without recanalization (patients 1 and 3), the VSI map in the hyperacute stage was compared with the FLAIR image on day 6 identifying the final infarct size. Increased VSI and decreased Q values in the subcortical area (arrowed in Fig. 7.7) matched well with the final infarct core.

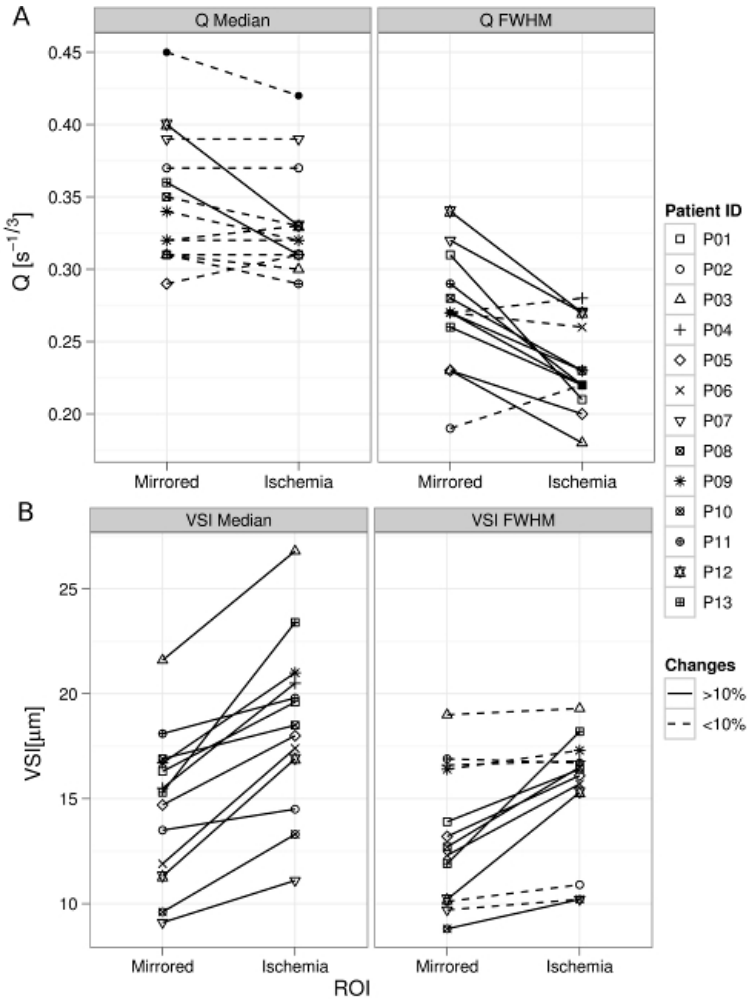

Figure 7.4: Trend plots of median and full-width at half-maximum (FWHM) in (A) Q and (B) vessel size index (VSI) in 13 patients. Data points are labeled by the patient ID corresponding to Table 7.1. Different line styles are used to identify the percentage change of value in the ischemic regions of interest (ROI) compared with the mirrored ROI. The change of value from the ischemic ROI to the mirrored ROI in percentage that is higher than 10% is presented by a solid line, and the change of lower than 10% is labeled by a dash line.

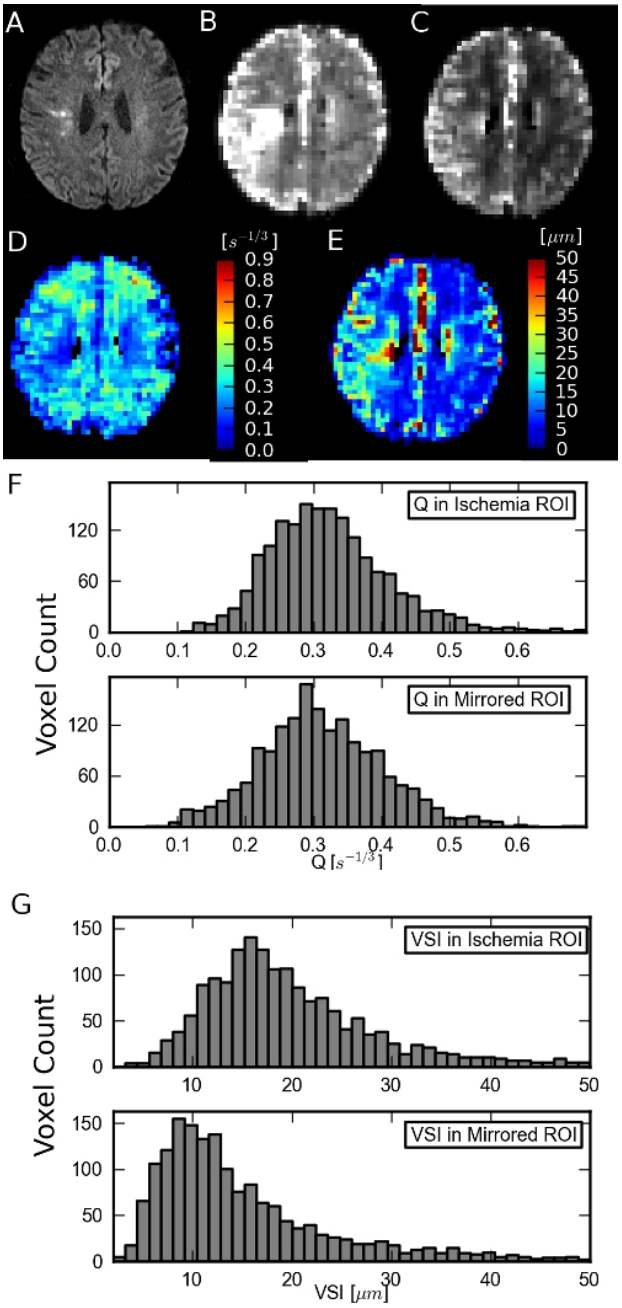

Figure 7.5: Images from patient 9 and histograms of Q and vessel size index (VSI) in ischemia and its mirrored ROI. Images in acute phase: (A) diffusion-weighted imaging (DWI), (B) mean transit time (MTT), (C) cerebral blood volume (CBV), (D) Q, and (E) VSI. Histograms of voxel-wise (F) Q and (G) VSI in the ischemic region (top) and its mirrored ROI in the contralateral hemisphere (bottom).

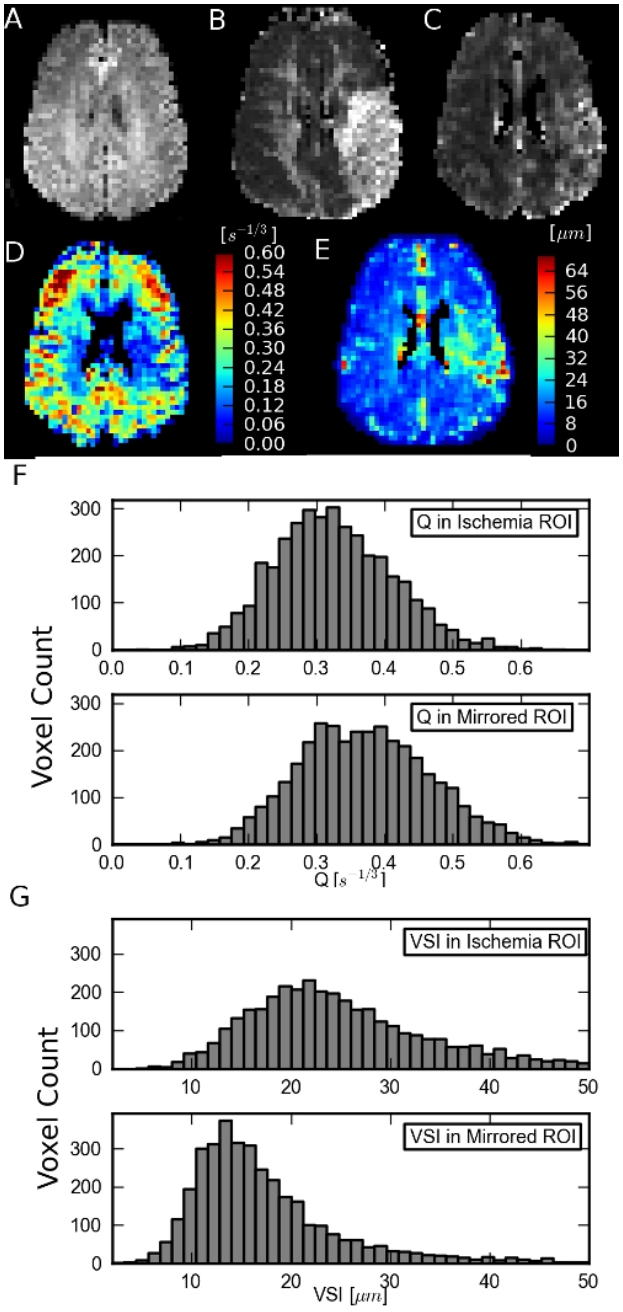

Figure 7.6: Images from patient 9 and histograms of Q and vessel size index (VSI) in ischemia and its mirrored ROI. Images in acute phase: (A) diffusion-weighted imaging (DWI), (B) mean transit time (MTT), (C) cerebral blood volume (CBV), (D) Q, and (E) VSI. Histograms of voxel-wise (F) Q and (G) VSI in the ischemic region (top) and its mirrored ROI in the contralateral hemisphere (bottom).

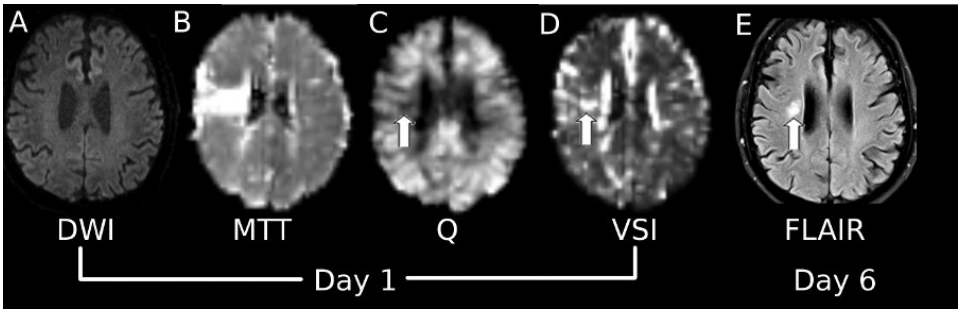

Figure 7.7: Images from patient 3 on day 1 and day 6. (A) Diffusion-weighted imaging (DWI), (B) mean transit time (MTT), (C) Q (D) vessel size index (VSI) on day 1, and (E) fluid attenuation inversion recovery (FLAIR) on day 6. The hypointensity on Q and hyperintensity on VSI matches the final infarction on FLAIR (pointed by the arrow).

7.3 Discussion

7.3.1 Feasibility of Vessel Size Imaging in Acute Stroke

Although the theoretical concept of vessel size imaging has been studied since 1998 [19, 108], the execution has been complicated by the acquisition of both GE and SE contrasts in a single repetition time during the dynamic bolus passage. The ssCE-MRI that uses GE and SE measurements before and after administration of an intravascular CA is a compromised technique to obtain ΔR_{2GE} and ΔR_{2GE} in the steady state and is so far used in most of the tumour and experimental stroke studies. However, this method is not suitable for clinical acute stroke imaging because of time constraints and the high dose of CA required to reach a measurable steady state. It produces VSI quantification by performing an additional blood test, as CBV cannot be assessed without dynamic imaging. Our pilot study has successfully accomplished dynamic GE and SE measurements in acute stroke patients by using a double-echo EPI sequence. The GE acquisition substitutes the standard PI measurement, which is part of the clinical imaging protocol. Therefore, vessel size imaging can be embedded in routine measurements without any time extension. However, this technique limits the time for readout gradients and thus restricts the image matrix to 64×64, which is only half of the resolution of single-echo perfusion images. Although parallel acquisition may overcome this limitation, it will reduce the image quantity to a great extent [109]. To maintain the spatial resolution, some studies performed separate conventional GE and SE acquisitions with dual injection of

CA to enable vessel size imaging [91]. Although the dual injection method avoids the sacrifice of image resolution, it brings other problems into discussion: the possible influence of the residual CA from the first injection on the second one, the potential temporal misregistration between two time series and the increased total dose of the CA. Furthermore, the prolonged measurement time of dual injection does not meet the crucial time limit of acute stroke imaging. The duo-echo technique used in this study with a voxel size of $3.6 \times 3.6 \times 5$ mm^3 is appropriate for acute stroke patients and provides MTT maps with diagnostic value (see MTT map on Fig. 7.2, 7.5, 7.6 and 7.7).

One study has published a quantitative Q assessment in human brain tissue [100]. The Q values in our study are somewhat lower than those found by Jensen et al. [100], in which a triple dose of CA has been administered and only the maximum signal drop points are used to estimate Q. Although such an implementation leads to a smaller underestimation of Q in the circumstance of intrinsic blood paramagnetism, it is not suitable for acute stroke imaging: first, such a high dose of CA is not commonly used in clinical routine; second, maximum signal drops between ischemic and normal tissue are not comparable, as the maximum drop in ischemic tissue is reached much later than in normal tissue with a significantly lower concentration of CA. Therefore, we have fitted the whole dynamic passage for the estimation of Q to achieve a relatively equivalent influence of CA dosage in both the ischemic and the normal tissue. Moreover, linear fitting avoids the accidental errors that often occur in picking a single signal drop.

The method in this study is based on the tissue model introduced by Kiselev et al. [20], which results in a systematic overestimation of vessel sizes. The VSI we measured in the thalamus, where no large vessels are present, is very similar to the value of 7.2 μm proposed by the microscale tissue model [20]. Jochimsen et al. [110] assessed venous VSI in healthy human brains with the administration of carbogen by measuring the induced blood oxygenation level-dependent effect in a 7 T scanner. Despite the different techniques, the vessel radii of GM and WM in our healthy volunteers are very similar to their venous vessel radii. The vessel sizes of the normal-appearing tissue in tumour patients studied by Hsu et al. [91] and Kiselev et al. [20] are almost twice as large as our results in healthy brain tissue. Besides the possible vascular compensation in the normal-appearing tissue around the tumour, the difference in results is mainly because we normalized the global CBV to 3%, which has been found to be a better estimation to the real blood volume fraction than the 6% used by their groups. Moreover, considering

that the VSI quantification depends on the assessment of CBV, the deconvolution with SNR-adapted regularization applied in our study allows an accurate estimation of CBV, which is more advanced than the integration of dynamic bolus passage or the fitting of the gamma function in previous studies.

The variation of MVD and VSI among three cerebral regions found in the healthy volunteers matched very well with general anatomical observations [111], i.e. the diameter of microvessels in WM and GM is very similar and lower vessel density is observed in WM than in GM. It indicates that vessel size imaging is a reliable and feasible technique to assess the microvascular morphology *in vivo*.

7.3.2 Standard Perfusion Parameters and Vessel Size Imaging

Vessel size imaging uses both dynamic GE and SE contrasts, whereas standard PI uses the GE only. It is well known that the GE contrast is sensitive to vessels of all sizes and SE contrast is weighted toward microvascular structure [112]. Therefore, VSI provides an insight into the properties of microvasculature, which are often shielded in the GE perfusion measurement predominated by large vessels. Considering that VSI is a quantitative parameter, it enables a comparison in inter-subject and longitudinal studies. This is an obvious advantage compared with perfusion parameters such as CBV and CBF presenting as relative values and MTT influenced heavily by the injecting condition of CA. However, one has to keep in mind that the change of VSI is inevitably dependent on the variation of CBV. When the MVD remains unchanged, the VSI map has a similar appearance to the relative CBV contrast.

7.3.3 Ischemic Penumbra and Vessel Size Imaging

Fig. 7.7 illustrates the interesting match between the predominant changes in acute VSI and Q maps and the final infarction in patient 3. It may indicate that severe damage of microvasculature obstructs the reperfusion and leads to tissue infarction. However, the possible correlation of increased VSI and decreased Q to the development of irreversible infarct cannot be confirmed. But, the lesions visible in the Q and VSI maps are always confined within the territory of MTT hyperintensities. Typically, in Fig. 7.6,

the hyperintensity on the VSI map only partially matches the MTT lesion, displaying a mismatch at the posterior part. Given the fact of the overestimation of the perfusion map, VSI might provide a better estimate of the ischemic penumbra from the aspect of microvascular structure.

7.3.4 Microvascular Response to Ischemia in the Hyperacute Phase

Given the limitation of a few patients, increased VSI in the ischemic region agrees with the observation from relative measurements of vessel size in rats. Reduced Q values in patients 12 and 13 fit to the decreased Q in the ischemic tissue in rats after transient focal ischemia [90]. The values of Q and VSI vary among patients due to different territories being involved in ischemia for each patient. The varied FWHM of Q and VSI distribution reveals that the changes may be regionally heterogeneous.

According to the observation in a pilot group of patients, we suggest that our data support the serial responses in the microvascular network to ischemia during the cerebral hemodynamic compromise [113]. As cerebral perfusion pressure falls after the occlusion, precapillary resistance vessels dilate to maintain CBF, which may account for our observation of increased vessel sizes. One should notice that the change of VSI is relatively small (at most 50% in our observation), which could be explained by the limited extent to which blood vessels can dilate. Once maximum vasodilatation has been reached, autoregulation fails and progressive increases in cerebral oxygen extraction can temporarily maintain cerebral oxygen metabolism. As perfusion pressure continues to fall, a disruption of cellular metabolism and microvascular obstruction occur [51], which is likely the cause of the decreased MVD within the ischemic region in patients 12 and 13. Moreover, the edema results in a more pronounced compression of small capillaries as compared with arterioles and venules, leading to a shift in the calculated average vessel size to larger values. However, no successive studies are currently available to monitor the extending microvascular changes after ischemic injury and the associated longitudinal vascular responses are not comparable between individual patients.

To sum up, our pilot results show that vessel size imaging is feasible in stroke patients. Further research is required to better understand microvascular response in the acute is-

chemic tissue. Longitudinal MRI examinations might help to correlate vessel size imaging to tissue fate and thus improve treatment tailoring.

Chapter 8

Application of Vessel Size Imaging in Acute Ischemic Stroke

In Chapter 7, we have demonstrated the feasibility of vessel size imaging in clinical stroke for the first time and its capability to detect pathological microvascular morphology in a small cohort of hyperacute stroke patients with a strict inclusion criteria of artery occlusion and the time from symptom onset less than 4.5 hours. As a follow-up research, this chapter is aiming to assess two parameters Q and VSI in a larger patient group (n = 75) and evaluate their potentials in the prediction of lesion growth in the subgroup with sixth-day follow-up measurements (n = 23).

8.1 Materials and Methods

The imaging techniques and data-postprocessing methods are described in Section 7.1.2 and Section 7.1.3, respectively.

8.1.1 Patients

Over a period of two months, patients admitted to the Charité - University Medicine Berlin hospital at campus Benjamin Franklin with a suspected diagnosis of acute stroke were examined with the vessel size imaging protocol on the day of admission. Seventy-five patients without specific selection of ischemic site met the inclusion criteria of a clinically

and radiologically confirmed acute ischemic stroke, a PI-DWI mismatch (the perfusion deficit volume larger than diffusion deficit) and the existence of a complete vessel size imaging measurement within 24 hours from symptom onset. Forty-nine patients (65%) had a clear time from stroke onset with a median of 2 hours (interquartile range (IQR), 1.3 to 4 hours). The exact time from stroke onset was not available in the remaining 26 patients. By checking the last-time-seen-well, we ensured that these patients were examined within the time window.

8.1.2 Regions of Interest

Delineation: The threshold of MTT larger than 5.3 s was set to be the initial threshold for hypoperfused tissue [107]. The MTT ROI was then corrected manually to exclude areas which were not part of a credible perfusion deficit by comparing with the normal perfusion distribution, particularly taking account of any differences between the two hemispheres or in the anteroposterior distribution and GM/WM differences. Acute DWI lesions were the intersected region of manual delineations by two human raters blinded to each other. The derived ROI was then mapped to ADC images to ensure ADC hypointensities (ADC < 0.7 μm^2/ms) and to exclude false positive T_2 shine-through effect [114] automatically. The follow-up FLAIR images on day 6, if applicable, were used to define the final infarct, which was the intersected area of manual delineations by two human raters with a comparison to baseline FLAIR images to avoid the potential misinterpretation of a subacute ischemic lesion or aging-related white matter hyperintensities [115]. Areas of haemorrhagic transformation were excluded from the FLAIR images (see Fig. 8.1). All the delineations and postprocessed maps were normalized to the standard space to derive two spatially symmetric hemispheres.

ROIs for entire population: For all 75 patients with baseline measurements, three areas were obtained for evaluation: (1) the initial infarct contour (INF) corresponding to the acute DWI lesion; (2) the ischemic penumbra (IPE) corresponding to the acute MTT minus the DWI mismatch; (3) the healthy tissue in the contralateral hemisphere (HEA) symmetric to the IPE.

ROIs for subgroup with follow-ups: For the 23 patients with sixth-day follow-up, IPE areas were divided into two regions: the area of infarct growth (IGR) corresponding

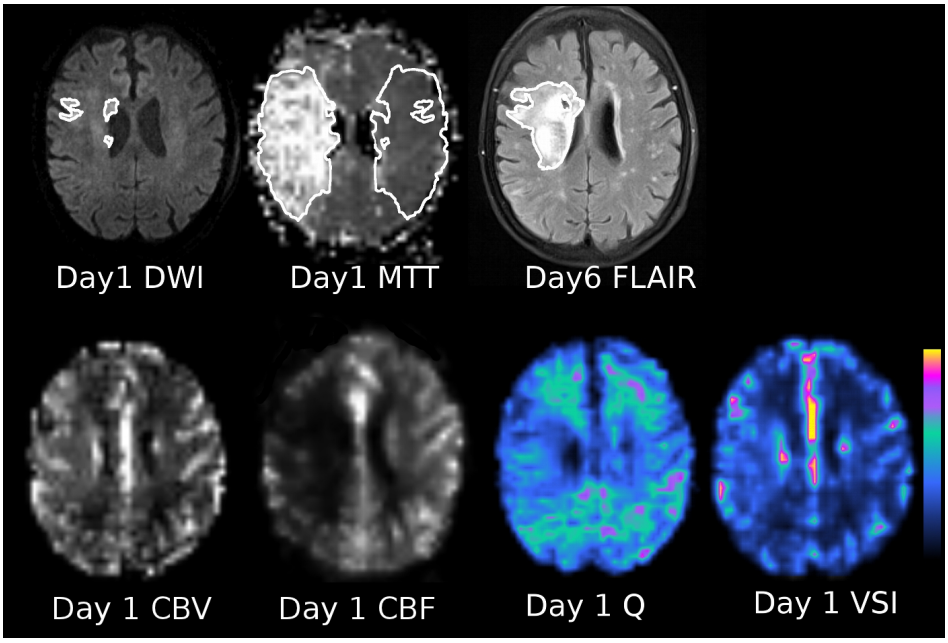

Figure 8.1: An illustration of region of interest (ROI) delineation in a patient (female, 85 years) with a right M1 occlusion, which was partially recanalized on the second day without receiving thrombolytic therapy. The acute diffusion-weighted imaging (DWI), mean transit time (MTT), cerebral blood volume (CBV), cerebral blood flow (CBF), Q and vessel size index (VSI) were taken 3.8 hours after onset of dysarthria and left-sided hemiparesis. The volume of hemodynamic disturbance (ROI on MTT map, 218.45 mL) exceeded the ischemic core (ROI on initial DWI image, 18.98 mL) and the final lesion size on the sixth-day fluid attenuation inversion recovery (FLAIR) images (68.39 mL). On the sixth-day FLAIR images, a haemorrhagic transformation occurred in the area of infarction. The contour of the final infarct was modified to exclude the haemorrhage. The region of healthy tissue (HEA) symmetric to the region of ischemic penumbra (IPE) (MTT minus DWI lesion on day 1) is presented on the contralateral hemisphere of the MTT map.

to the day 6 FLAIR minus day 1 DWI lesion, as well as the oligemic area (OLI), which was hemodynamically disturbed but remained viable, corresponding to the MTT minus day 6 FLAIR lesion. Together with pre-defined INF and HEA, four ROIs were derived for these patients.

8.1.3 Statistical Analysis

The volumes between day 1 DWI and day 6 FLAIR lesions, as well as MTT lesion and day 6 FLAIR lesion, were examined by the Wilcoxon signed-rank test.

The Lilliefors normality test confirmed that Q and VSI in each ROI did not follow the nor-

	Patients with Mismatch (n = 75)	Patients with Day 6 Follow-up (n = 23)
Gender Female (%)	42 (55)	9 (39)
Age in years (IQR)	77.0 (68.5 - 86.0)	71.0 (61.5 - 75.5)
Occlusion (%)	54 (72)	18 (78)
tPA (%)	31 (41)	13 (57)
NIHSS admission (IQR)	7 (3 - 15)	4 (3 - 10)
NIHSS discharge (IQR)	2 (0 - 9)	1 (0 - 2)
Day 1 DWI in mL (IQR)	2.51 (0.36 - 11.99)	0.61 (0.23 - 4.22)
Day 1 MTT in mL (IQR)	60.18 (16.50 - 76.50)	58.57 (24.02 - 98.22)
Day 6 FLAIR in mL (IQR)	—	6.49 (1.82 - 15.04)
Recanalization (%)	—	13 (57)

Table 8.1: Overview of patients' clinical and radiological data. tPA indicates tissue plasminogen activator; IQR, interquartile range; NIHSS, national institutes of health stroke scale; DWI, diffusion-weighted imaging; MTT, mean transit time; FLAIR, fluid attenuation inversion recovery.

mal distribution. Therefore, median and IQR were used to express the distribution. The Q and VSI median values were compared across patients between areas by the Friedman test with the Wilcoxon-Nemenyi-McDonald-Thompson post hoc analysis. The ability of Q and VSI values to discriminate INF and IGR from OLI and HEA was evaluated by using the receiver operating characteristic (ROC) curve analysis.

8.2 Results

From the 75 patients with PI-DWI mismatch, 42 were female (56%) and the median age was 77 years (IQR, 68.5 to 86.0 years). Further clinical and radiological data are presented in Table 8.1.

The values of Q and VSI calculated in HEA, IPE, and INF of all the patients are presented in Fig. 8.2. The Q in the abnormal areas i.e. IPE and INF was significantly smaller than that in the healthy tissue ($p < 0.05$). However, it did not allow us to distinguish INF from IPE. The VSI was significantly different between all the three areas ($p < 0.05$).

In the patient cohort with sixth-day follow-up measurements (n = 23), 20 patients (87%) presented with lesion growth, i.e. sixth-day FLAIR lesion larger than first-day DWI lesion. The volume of MTT hypoperfusion exceeded the volume of sixth-day FLAIR

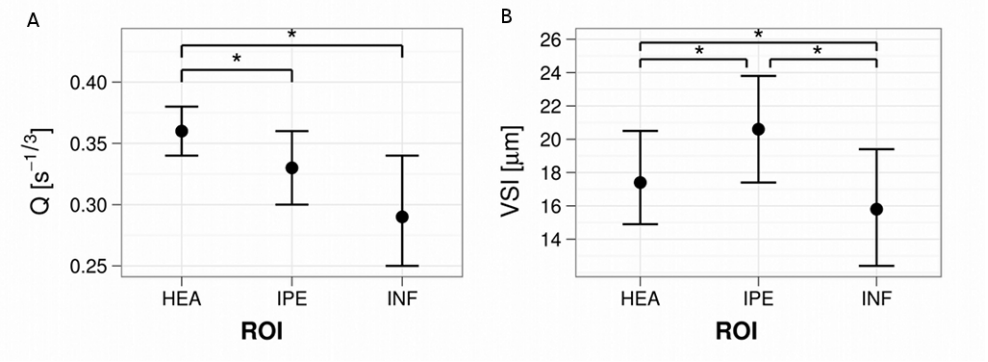

Figure 8.2: The statistic results of Q and vessel size index (VSI) of acute patients in the group study. (A) Q and (B) VSI measured in the three regions defined in our study for the patients with day 1 measurements. Values are presented in the form of median and interquartile range (IQR). For Q, all pair-wise comparisons of subgroups are significantly different, except between IPE and INF; for VSI, all pairwise comparisons of subgroups are significantly different. The significant level labelled by * is set to be $p < 0.05$. ROI indicates region-of-interest; INF, initial infarct; IPE, ischemic penumbra; HEA, healthy tissue.

ROI	Q[s$^{-1/3}$]	VSI [μm]
HEA	0.37 (0.32 - 0.43)	17.0 (12.5 - 24.3)
OLI	0.34 (0.30 - 0.39)	19.3 (14.8 - 25.9)
IGR	0.30 (0.26 - 0.36)	17.1 (12.5 - 24.1)
INF	0.28 (0.23 - 0.34)	14.8 (10.1 - 21.1)

Table 8.2: Q and vessel size index (VSI) measured in the four regions of interest (ROIs) defined in our study for the patients with day 6 follow-up measurements. Values are presented in the form of median (IQR). IQR indicates interquartile range; HEA, healthy tissue; OLI, oligemic area; IGR, infarct growth; INF, initial infarct.

lesion ($p < 0.001$, see Table 8.1). The voxel-wise distributions of Q and VSI in the four ROIs are demonstrated in Fig. 8.3. From top to bottom in Fig. 8.3A, in the order of HEA, OLI, IGR and INF, the distribution of Q shifts to smaller values, indicating a decrease in MVD. In Fig. 8.3B, the VSI values display similarly broad distributions in nonviable areas (INF and IGR) and present with a lagged tail in HEA and OLI. Compared to the distribution in HEA, the VSI in the OLI shifts to larger values. The corresponding median values and IQR of Q and VSI histograms in four regions are listed in Table 8.2.

Fig. 8.4 shows the ROC curve that evaluates the ability of Q and VSI to predict the final lesion area (including INF and IGR) from the recovered and healthy regions (OLI and HEA). The diagnostic performance of Q was acceptable with the area under the curve of ROC equal to 0.72. The threshold 0.32 s$^{-1/3}$ gave the best cut-off with the accuracy of 69% in differentiating INF and IGR from OLI and HEA with a sensitivity of 69% and

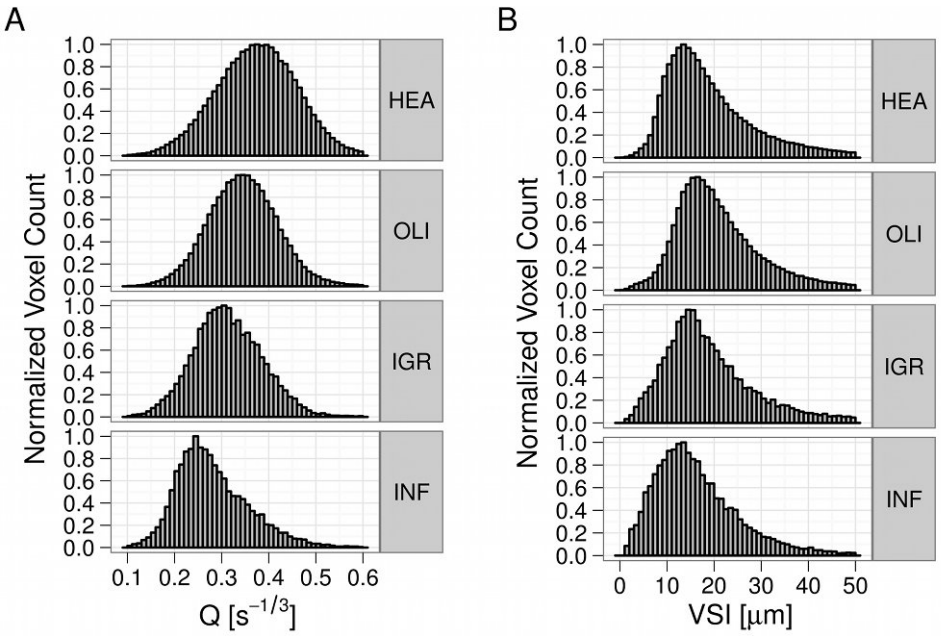

Figure 8.3: Histograms of the Q (A) and vessel size index (VSI) (B) distribution in the four regions of interest (ROIs) and for all 23 patients with sixth-day measurements together. The voxel count for each histogram is presented with the highest column normalized to 1. HEA indicates healthy tissue; OLI, oligemic area; IGR, infarct growth; INF, initial infarct.

a specificity of 64% and is labelled on the ROC curve in Fig. 8.4. The performance of VSI for prediction was worse than Q with the area under the curve of 0.59. The optimal cut-off with the accuracy of 68% for the prediction by VSI was achieved at the threshold of 14.6 μm with a sensitivity of 70% and a specificity of 43% (see Fig. 8.4).

8.3 Discussion

In the current study, we showed that vessel size imaging can image the microvasculature by employing two quantities Q and VSI and that its application is feasible in the clinical stroke study. The application of a dynamic duo-echo sequence substituting the standard PI acquisition provided both GE and SE contrasts and could be embedded into clinical routine without any time extension. Although the matrix size was sacrificed for double contrasts, the image resolution of the derived perfusion maps was still sufficient for clinical diagnosis.

In our patient cohort with baseline measurements, the microvascular network demon-

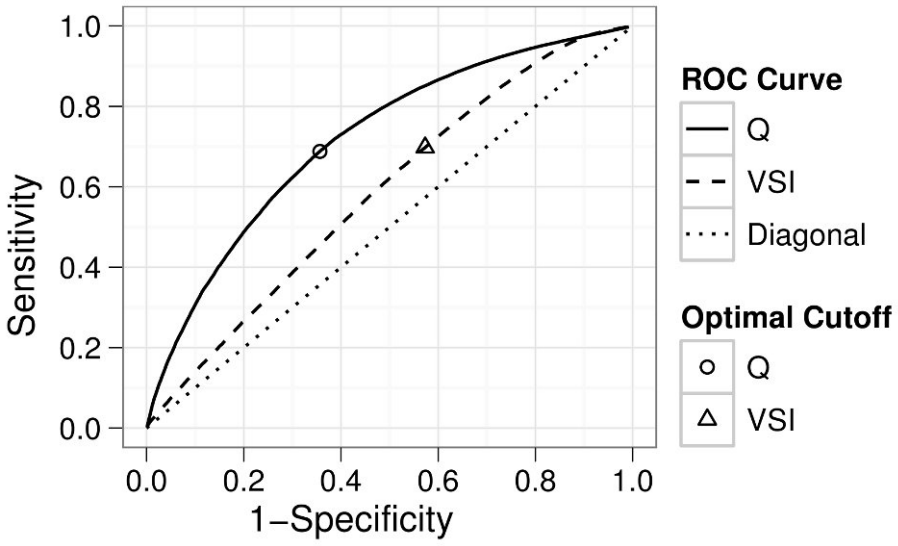

Figure 8.4: The receiver operating characteristic (ROC) curve for evaluating the ability of Q and vessel size index (VSI) to predict final infarction from healthy and recovered tissue. The optimal cutoff thresholds labelled on the curves are 0.32 $s^{-1/3}$ for Q with an accuracy of 69%, a sensitivity of 69% and a specificity of 64%, and 14.6 μm for VSI with an accuracy of 68%, a sensitivity of 70% and a specificity of 43%, respectively.

strated changes within the ischemic penumbra (IPE) in terms of MVD and average vessel size, referring to Q and VSI respectively. The result of this study, with a large patient cohort, a broader time window of 24 hours and a presence of PI-DWI mismatch coincided with our previous pilot study [116] and a rat study [90]: the reduced MVD and the increased mean vessel radius were observed in ischemic penumbra compared to the healthy symmetrical region (Fig. 8.2). These observations could be explained by a more pronounced effect of edema on the compression of small capillaries as compared to larger arterioles and venules, leading to a shift in the calculated average vessel size [51]. The vasodilatation due to the autoregulation of the cerebral vascular network further results in the elevation of the VSI in the ischemic tissue.

Although the individual variations in Q between IGR and OLI did not reach a significant level in our small patient cohort (n = 23) with follow-up measurements, Q tended to shift successively to smaller values in voxel-wise distributions from HEA, OLI and IGR to INF (see Fig. 8.3A). These four distributions are significantly different from each other based on the large number of voxels. The Q map presented in Fig. 8.1 with hypointensities in IGR and INF matches the shifts showed in the histograms. Clear contrast differences

between IGR and OLI can be observed on the Q map in Fig. 8.1. In order to test whether the shift of histogram is due to the pathological effect, we further segmented each ROI into GM and WM. The same trend in both GM and WM confirmed that decreased MVD mainly resulted from the ischemia, rather than the tissue type. The greater drop of the measured MVD in INF and IGR compared to OLI and HEA could be explained by the increased degree of ischemic cell death with more swelled cells compressing the capillaries in the non-viable area [51]. Thus, Q may be a reasonable predictor for the tissue outcome. This also explains the lack of the significance for Q between INF and IPE in the 75 patients with a baseline scan, since IPE also covered the area of IGR, in which Q dropped heavily similar to the drop in the INF. Therefore, Q could be a supplemental imaging maker to acute DWI, which is sensitive to the INF and does not provide the differentiation between IGR and OLI.

The diagnostic performance of Q was fairly good given the area under the curve of ROC with the value of 72%. However, the capability of Q for prediction is not as good as that of CBV, CBF and MTT in terms of sensitivity and specificity [107, 117]. Unlike perfusion parameters that change immediately after vessel occlusion, Q decreases with the evolution of cell death, which could influence the sensitivity of Q. On the other hand, this dependence enables Q to be a reliable evaluator for the tissue fate by possibly preventing the overestimation of penumbra in oligemia, which is commonly seen in the MTT. Moreover, the calculation of Q can be done by a one-step linear fitting thus its value is rather stable. This is an apparent advantage for the clinical use considering that the post-processing of the conventional perfusion parameters is very sophisticated and time-consuming and their values are highly dependent on the methods being used [62].

The prediction accuracy of Q is mainly affected by the heterogeneous structure of the vascular network in different types of tissue. Differences in vessel density between GM and WM have been showed in healthy volunteers in our feasibility study [116]. This explains the broad range of the voxel-wise histograms in Fig. 8.3A. The pathological effects on Q could be partially shielded by the variation between GM and WM. As shown in Fig. 8.1, although Q in the cortex within the contour of lesion growth is decreased compared to the contralateral hemisphere, it appears to have a similar contrast to that in the healthy WM. Furthermore, the viability of the Q threshold might be different according to the location. The accuracy of prediction might benefit from segmentation ROIs to define the specific threshold according to the location. After all, cerebral ischemia is a very

dynamic process and the critical thresholds for viability are dependent on its duration of the ischemia [23]. The originally decreased MVD in the ischemic tissue could elevate again in the subacute stage due to angiogenesis [89] and the tissue may prevent the fate of infarction. It has been proposed that coupling CBV and CBF for thresholding will raise the accuracy for prediction [117]. In future studies, the combination of Q with conventional perfusion parameters can be assessed for identification of lesion growth.

Although the VSI was significantly different between all three regions defined in patients with the baseline measurement, it failed to provide useful information in predicting lesion growth giving a poor area under the curve of 0.59. Besides its heterogeneity in normal brain regions, the VSI is also very sensitive to the presence of large vessels and voxel contamination by CSF. When a voxel is dominated by a large vessel or the CSF, the measured VSI deviates towards much higher values (see Fig. 8.1). This explains the long tails of the VSI distributions in Fig. 8.3B. The shift in the OLI to larger VSI values compared to HEA is very likely due to the vasodilatation of arterioles and venules. In both INF and IGR, the VSI distributions had a wide range. To understand this, we have to keep in mind that the modelling and calculation of VSI is inevitably dependent on CBV. It has been found that CBV decreases significantly in the area of the initial infarct core and lesion growth since the tissue is badly perfused. This drives the decrease of the VSI. On the other hand, both edema and the absence of the CA cause an overestimation of VSI [20]. These two opposite effects result in the broad distribution of the VSI. Moreover, the areas of INF and IGR in our patients were very small compared to other stroke studies [107, 117]. The possible miscoregistration of very small ROIs of INF and IGR could influence the results as well.

The majority of our patients did not receive a sixth-day measurement due to the early discharge. As a two-month experimental study, this study did not have resources to monitor and recruit discharged patients to accomplish the follow-up examination. More than half of patients with follow-up measurements were detected to have recanalization on the second day. It could explain the large overshot of acute MTT deficit to the sixth-day infarction. Although a different prediction model for the final lesion might be expected between patients with and without recanalization, it is difficult to examine this hypothesis in the current cohort ($n = 23$). The time window was defined as 24 hours because ischemic penumbra dynamically evolves during the first day after symptom onset [118]. Moreover, the time window of 24 hours is reasonable to monitor the changes of Q, which is not an

immediate sign after ischemia.

Although the application of perfusion in clinical practice is restrained by unsolved methodical issues and no significant superior performance has been found between conventional parameters, such as MTT, Tmax, CBV and CBF [119], we employed the MTT deficit to identify the tissue at risk due to its high sensitivity and homogeneity, as well as its nature as a microvascular perfusion calibre [65]. Given the fact of unreliable performance of delineation by the automated software [120] or visual assessment [121], we used the combination of thresholding and visual correction to detect the lesion edge. The threshold of 5.3 s in MTT was proposed with good correlation of results in positron emission tomography and appeared reliable in our patient cohort [107]. Additionally, we performed the same study with different MTT thresholds ranging from 4 s to 6 s. There were no differences regarding the statistic results of Q and VSI between these thresholds.

In conclusion, the microvascular network responds to cerebral ischemia with decreased vessel density quantity Q and increased mean vessel size VSI in the hemodynamically disturbed area. Although the Q shows a trend to identify the severity of ischemia in an overall voxel population, its potential in predicting the infarct growth needs to be further tested in a single case level. To confirm this, further studies with a larger patient cohort including clear status of reperfusion and recanalization and complete follow-up measurements are required.

Part III

New Concept on Dynamic Susceptibility Contrast Imaging

Chapter 9

Observation of the loop formed on the ($\Delta R_{2SE}^{3/2}$, ΔR_{2GE}) Plane

The DSC MRI is the most commonly used imaging method to assess cerebral perfusion in clinical studies, for example of tumour and stroke. The rapid dual-echo EPI technique makes it possible to track the CA bolus in both GE and SE contrasts simultaneously. This can be exploited to characterize the cerebral microvasculature *in vivo*, which includes arterioles, capillaries and venules. It is possible because the transverse relaxation rate R_{2GE} measured by a GE and the transverse relaxation rate R_{2SE} measured by an SE are differently affected by the inhomogeneous magnetic field induced by the paramagnetic contrast confined in the local microvascular network [94]. Changes of these rates ΔR_{2GE} and ΔR_{2SE}, measured after the administration of a paramagnetic CA, yield the information of mean vessel size inside an imaging voxel. Attempts have been made to use the dependence between ΔR_{2GE} and ΔR_{2SE} to estimate the vessel size in rats [19, 108], healthy subjects [110, 122], tumour patients [20, 123] and ischemic stroke patients [116].

Analytical models were developed to calculate the signal relaxation due to magnetic field inhomogeneity induced by the microvascular network [95–97, 124]. This theory was used to express an averaged microvessel size in an imaging voxel, referred to as VSI [19, 20] (see Chapter 6 for detail). The VSI is understood as the vessel radius specifically averaged over the microvessel population weighted with its volumetric fraction, and is proportional

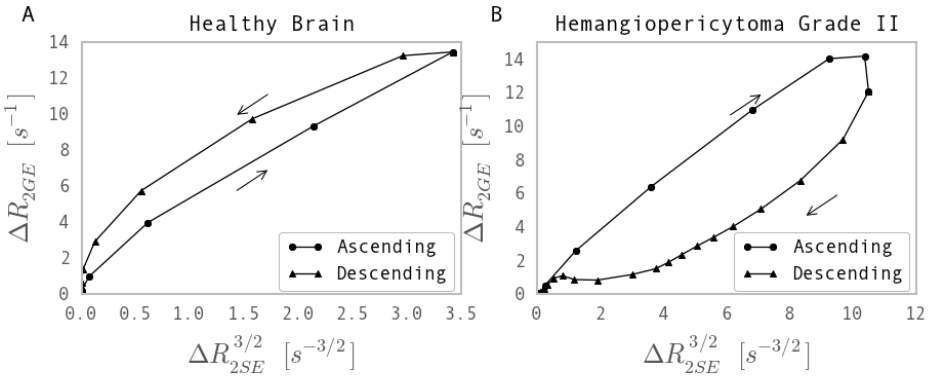

Figure 9.1: Examples of the hysteresis loop on ($\Delta R_{2SE}^{3/2}$, ΔR_{2GE}) plane in (A) a healthy brain and (B) a hemangiopericytoma grade II. The direction of the loop is (A) counter-clockwise in the healthy brain and (B) clockwise in the tumour.

to the ratio of ΔR_{2GE} and $\Delta R_{2SE}^{3/2}$ according to

$$VSI = 0.867(\zeta D)^{1/2} \frac{\Delta R_{2GE}}{\Delta R_{2SE}^{3/2}}, \tag{6.15}$$

where ζ and D are the CBV and the ADC, respectively.

In human studies with a DSC imaging implementation [20, 91, 116], the quantities ΔR_{2GE} and ΔR_{2SE} were converted from the signal drops after the CA administration by following

$$\Delta R_2(t) = -\frac{1}{T_E} \ln \frac{S(t)}{S_0}, \tag{4.6}$$

where $S(t)$ is the signal intensity recorded at time t, and S_0 is the averaged baseline signal over the time before CA administration (see Fig.7.1A and B for illustration). As shown in Fig. 7.1D, the ratio of $\Delta R_{2GE}/\Delta R_{2SE}^{3/2}$ is obtained by fitting the data points on the plane of $\Delta R_{2SE}^{3/2}$ as the x-coordinate versus ΔR_{2GE} as the y-coordinate.

In the ideal case of the model, ΔR_{2GE} is linearly dependent on $\Delta R_{2SE}^{3/2}$. However, the dependence of ΔR_{2GE} on $\Delta R_{2SE}^{3/2}$ during the first pass of the CA bolus often displays a difference between the initial increase and the following decrease of the CA concentration, similar to a hysteresis loop (see Fig. 9.1). Noticeably, it has been reported that the shape of the loop and the direction of its passage may differ between normal brain tissue and tumour tissue [20, 91].

Kiselev et al. [20] interpreted that the formation of the loop is due to the different

involvement of arterial and venous blood pools during the bolus passage . However, detailed investigation was not available and hindered by fitting experimental data with the gamma variate function and by the use of monosized vessel distribution in each microvascular pool. These limitations are to be released for understanding the loop formation.

So far, most studies on DSC modelling have focused on analyzing the MRI signal in the entire cerebrovascular network as a single operator [106, 125]. This is not sufficient for studying the behaviors of vessels in different microvascular pools. Mouridsen et al. [126] presented a parallel capillary system using incomplete gamma variate functions with a distribution of transit times. However, the gamma variation function has been reported to be an incorrect parametrization of the residue function based on a comparison of the simulation and ASL experimental data [127]. Gall and Kiselev [128] have proposed a vascular tree model with the transport function in each vessel generation following the laws of laminar flow, which was found to be in an excellent agreement with ASL measurements [129]. However, the susceptibility effects of CA and intrinsic blood were not considered in this work focused on vessel transport functions.

Understanding the mechanism of the loop formation is the primary aim of Part IV. To achieve this, we further develop the vascular tree model with multiple vessel generations in different blood pools, and simulate the transient variation of ΔR_{2GE} and ΔR_{2SE} during the bolus passage in the vasculature with various blood composition and transport, in order to explore the factors influencing the shape of the loop and the direction of its passage. These details are described in the following Chapter 10. To investigate the potential value of the loop in clinical studies, a post-processing method is proposed for a simple parametric characterization of the loop, and applied to experimental data from a previous study in tumour and stroke patients in Chapter 11.

Chapter 10

Understanding the Formation of the Loop

In this chapter, the modelling and the simulation are described, which are based on the theory of susceptibility-induced MRI signal dephasing in a cerebrovascular network [95–97, 124]. The present work adapts the model introduced in Section 6.1.2 for multiple vessel generations to account for kinetics of the bolus passage through the microvasculature.

10.1 Modelling and Simulation

10.1.1 Tissue Modelling

The tissue in a volume of interest (VOI) is modelled with two compartments: blood in vessels occupying a volume fraction ζ and brain parenchyma. The vascular network consists of three types of vessels: arterioles, capillaries and venules, with the volume fractions of ζ_a, ζ_c, and ζ_v, respectively. The vascular network is modelled by a tree structure with symmetric arterial and venous parts, in which vessel generations are self-similar [130] and follow Murray's law [131], so that the diameter of each vessel generation is reduced by the factor of $2^{1/3}$ at each bifurcation (see Fig. 10.1). There are 55 vessel generations (25 arterioles, 5 capillaries and 25 venules) in the vascular system with the largest diameter of 2.9 mm as the common size of the proximal middle cerebral artery [132] and the smallest diameter of 5.7 μm as the mean size of a capillary population [133]. The

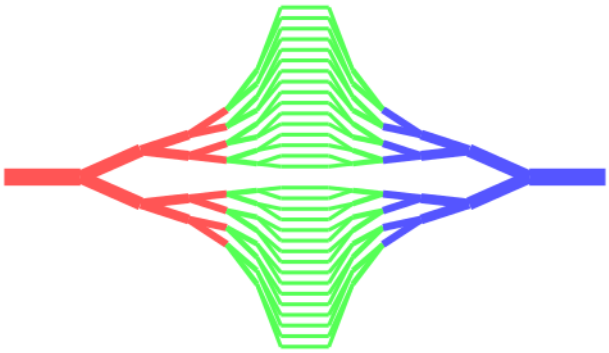

Figure 10.1: Illustration of the vascular tree model. Arterioles are labelled in red, capillaries in green and venules in blue.

vessel generations with a diameter smaller than 10 μm are considered as capillaries [134]. Each vessel generation of the same vessel type, $\alpha = a$ (arterioles), c (capillaries), and v (venules), is assumed to occupy the same volume fraction, so that the blood volume fraction of a vessel generation k can be written as

$$\zeta_{\alpha k} = \zeta_\alpha / N_\alpha, \tag{10.1}$$

where N_α is the number of vessel generations in vessel type α.

10.1.2 Transport Function

The blood flow in the brain vasculature is assumed to be laminar. The vessel segments between bifurcations are considered to be cylindrical pipes. The transport function introduced in [105] is used here for each vessel generation

$$h(t) = \begin{cases} t_0/t^2 & \text{if } t \geq t_0 \\ 0 & \text{otherwise} \end{cases}, \tag{10.2}$$

where t_0 is the transit time of blood in the central streamline. The residue function $R_k(t)$

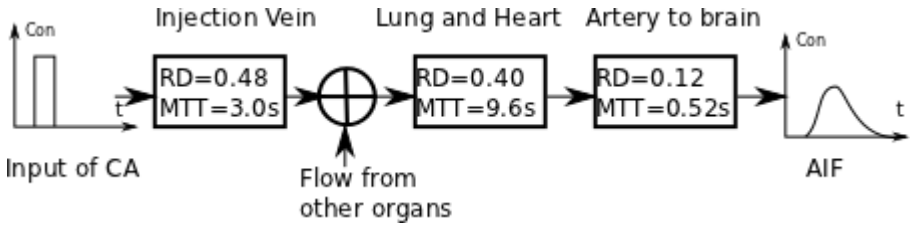

Figure 10.2: Illustration of the transport process from the injection vein to the brain. CA indicates contrast agent; Con, concentration of CA; RD, relative dispersion; MTT, mean transit time; AIF, arterial input function.

of a vessel generation k takes the form of

$$R_k(t) = h_1(t) \otimes h_2(t) \cdots \otimes h_{k-1}(t) \otimes \left(1 - \int_0^t h_k(t')dt'\right), \tag{10.3}$$

where the convolution chain $h_1(t) \otimes h_2(t) \cdots \otimes h_{k-1}(t)$ indicates the blood transport before the vessel generation k. The CA time-concentration curve $C_k(t)$ in the vessel generation k is written as

$$C_k(t) = fC_i(t) \otimes R_k(t), \tag{10.4}$$

where f is the CBF and $C_i(t)$ is the AIF to the brain.

10.1.3 Arterial Input Function to the Brain

The AIF to the brain was calculated from the venous injection site by following the human blood circulation model proposed by van Osch et al. [125], in which the body compartments were modelled as vascular operators with specific MTT and relative dispersion (RD) [135]. Only the first passage was calculated in this study for simplicity. The transport process is illustrated in Fig. 10.2.

10.1.4 Signal Simulation

Signal simulation is performed as in [98]. In either SE or GE experiments, the total MRI signal $s(t)$ from the VOI takes the form of the combination of the intravascular signal

$s_i(t)$ and the extravascular signal $s_e(t)$ weighted by their volume fraction:

$$s(t) = \zeta s_i(t) + (1 - \zeta) s_e(t). \tag{10.5}$$

We note that all signals expressed with low-case s in the equations are normalised on unity for $t = 0$. The intravascular signal is a sum from arterioles, capillary and venules weighted with their volume fractions. Therefore, its contribution in Eq. (10.5) can be replaced as

$$\zeta s_i(t) = \sum_{k=1}^{N_a} \zeta_{ak} s_{ak}(t) + \sum_{k=1}^{N_c} \zeta_{ck} s_{ck}(t) + \sum_{k=1}^{N_v} \zeta_{vk} s_{vk}(t) \equiv \sum_{\alpha} \sum_{k=1}^{N_\alpha} \zeta_{\alpha k} s_{\alpha k}(t), \tag{10.6}$$

where $s_{\alpha k}(t)$ is the signal contribution of the kth vessel generation in vessel type α. The signal from the blood in arterial vessel generations s_{ak} and venous ones s_{vk} decays exponentially with time:

$$s_{\alpha k}(t) = \exp\{-[R_{2\alpha 0} + rC_{\alpha k}(t)]T_E\}, \tag{10.7}$$

where $\alpha = a, v$, and T_E is the echo time. R_{2a0} and R_{2v0} are the relaxation rates in arterial and venous blood without the CA, respectively, which are taken from *in vitro* measurements. The term $rC_{\alpha k}(t)$ describes the relaxation induced by a time-dependent CA concentration $C_{\alpha k}(t)$, where r is the relaxivity of the CA. The signal from capillaries $s_{ck}(t)$ is calculated by a linear interpolation of the relaxation rate between the arterial and venous ends. This yields

$$s_{ck}(t) = \frac{\exp(-R_{2a0}T_E) - \exp(-R_{2v0}T_E)}{(R_{2v0} - R_{2a0})T_E} \exp[-rC_{ck}(t)T_E]. \tag{10.8}$$

Finally, two exponential relaxation processes are considered for the extravascular signal in Eq. (10.5):

$$s_e(t) = \exp\{-[R_{2p0} + R_{2p}(t)]T_E\}, \tag{10.9}$$

where R_{2p0} is the rate of relaxation in parenchyma caused by the spin-spin interactions at the molecular scale, which can be measured at very short echo times. In turn, the relaxation rate $R_{2p}(t)$ is caused by susceptibility effects of vessels, which take the form of

a sum of relaxivities of each vessel generation:

$$R_{2p}(t) = \sum_{\alpha} \sum_{k=1}^{N_\alpha} \zeta_{\alpha k} r_{2\alpha k}(t), \tag{10.10}$$

where $r_{2\alpha k}(t)$ are functions to characterize the relaxivity of vessel generation k of a given type α and radius ρ_0. These functions are vessel-specific, since the relaxation effect depends on two parameters: 1) the diffusion time across the vessel, $t_D = \rho_0^2/D$, where D is the diffusion coefficient; 2) the characteristic shift of the Larmor frequency on the surface of the vessel $\omega = 2\pi\chi\gamma B_0$, where γ is the gyromagnetic ratio, B_0 is the magnetic field strength, and χ is the magnetic susceptibility of the blood as a combination of the susceptibility contributed by the CA and the one contributed by natural blood depending on its type α. These two parameters, together with the T_E of the experiment, determine the relaxation under different conditions: SDR and DNR (see Section 6.1.3 for details).

Analytical theory is available for both the DNR and the SDR, which yields explicit expressions for the case of short and long times. This study uses the signal simulation module described in [98], which is based on interpolations between analytical expressions known for the DNR and the SDR.

The SDR applies when the typical phase acquired by a proton diffusing past a vessel is large, $\omega t_D \gg 1$. For this case, analytical results of the vessel relaxivity for GE measurements are

$$T_E r_{2\alpha GE} = \frac{2}{15}(\omega T_E)^2 \tag{10.11}$$

for $\omega T_E \ll 1$ and

$$T_E r_{2\alpha GE} = \frac{2}{3}\omega T_E - 1 \tag{10.12}$$

for $\omega T_E \gg 1$. Similarly, the relaxivity in the SE measurement takes the form

$$T_E r_{2\alpha SE} = \frac{1}{15}(\omega t_D)^2 \left(\frac{T_E}{t_D}\right)^3 \tag{10.13}$$

for $(\omega t_D)^{2/3} T_E/t_D \ll 1$ and

$$T_E r_{2\alpha SE} = 0.694(\omega t_D)^{2/3} \frac{T_E}{t_D} - 1 \tag{10.14}$$

for $(\omega t_D)^{2/3} T_E/t_D \gg 1$.

In the DNR, the diffusion time is in the order of the time that a water molecule needs to diffuse across a distance comparable with the vessel radius. Hence, the diffusion is so fast that the spins reside in the vicinity of a vessel for only a relatively short time acquiring a small phase $\omega t_D \ll 1$. The vessel relaxivity is then given by

$$T_E r_{2\alpha GE} = \frac{4}{45}(\omega t_D)^2 \left[\frac{T_E}{t_D}\left(\ln\frac{T_E}{t_D} + 0.309\right) + \frac{1}{4}\ln\frac{T_E}{t_D} + 0.619\right] \tag{10.15}$$

for GE measurements and

$$T_E r_{2\alpha SE} = \frac{8}{45}(\omega t_D)^2 \left[\frac{T_E}{2t_D}\left(\ln\frac{T_E}{2t_D} - 0.384\right) + \frac{1}{4}\ln\frac{T_E}{2t_D} + 0.619\right] \tag{10.16}$$

for SE measurements. The crossover between the DNR and the SDR occurs in the range of $\omega t_D \approx 6$ [98].

10.2 Results

To match our experimental voxel size of $3.6 \times 3.6 \times 5$ mm^3, the diameter of the feeding artery and the draining vein was around 290 μm calculated from the scaling rule [130], which resulted in ten vessel generations before reaching the voxel and 35 vessel generations inside the voxel (15 arterioles, 5 capillaries and 15 venules).

The transit time t_0 in Eq. (10.2) was set to 70 ms in each vessel generation for normal blood transport, which is obtained from scaling the reasonable MTT in the entire brain of 4 s [136] by 55 as the number of vessel generations. The transit time $t_0 = 300$ ms was used for the case of strong dispersion when simulating a reduced blood flow in stroke.

We approached the result by a gradual change of the bolus shape from completely unrealistic to a realistic one (see Fig. 10.3 from A to B). The plots in the left column of Fig. 10.3 show the CA concentration curve along the time in different vessel generations. The curves are labelled in red, green and blue for arterioles, capillaries and venules, respectively. The corresponding plots of dynamic changes in ΔR_{2GE} versus $\Delta R_{2SE}^{3/2}$ show a comparison of a voxel with more venous blood ($\zeta_a = 0.5\%$, $\zeta_c = 2\%$, $\zeta_v = 1\%$) in the middle column, and a voxel with more arterial blood ($\zeta_a = 1\%$, $\zeta_c = 2\%$, $\zeta_v = 0.5\%$) in the right column. Note that the capillary blood volume is identical in both cases

($\zeta_c = 2\%$ [134]). These dynamic curves evolving from red, via green, to blue, illustrate the changes of $\Delta R_{2GE}/\Delta R_{2SE}^{3/2}$ during passage of the peak of the bolus from arterioles, to capillaries, to venules.

Considering a scenario of an infinitely long delay in the blood transport and no dispersion, the bolus passage in each generation is completed before the passage to the next generation occurs. Thus, each vessel generation follows an individual line in this case (see Fig. 10.3A). Given the fact that the ratio $\Delta R_{2GE}/\Delta R_{2SE}^{3/2}$ is proportional to the vessel diameter [20], the obtained slopes for capillaries are much smaller than those of arterioles and venules. Since the first two and the last two of capillary generations are symmetric, their lines coincide. Hence, three capillary lines are observed for five capillary generations. Slightly larger slopes for venules than those obtained for arterioles with the same diameter are due to the presence of deoxyhemoglobin in venous blood. Note that the maximum ΔR_{2GE} and ΔR_{2SE} reached at the maximum CA concentration are proportional to the volume fraction for each generation. Therefore, the venous branches (blue) end in higher ΔR_2 values than the arterial ones (red) in the voxel with larger ζ_v (see the middle column of Fig. 10.3A), whereas the opposite is obtained for the voxel with larger ζ_a (see the right column of Fig. 10.3A).

When the bolus passages overlap in each generation as shown in Fig. 10.3B for a transit time delay of 70 ms, the dependence between ΔR_{2GE} and $\Delta R_{2SE}^{3/2}$ forms a loop in both voxels by following the slope of the arterioles at the very beginning, then transiting to the capillaries, and returning back to the venules. The direction of the loop can be changed in simulations by adjusting the relative arterial and venous blood volume fractions. If the arterial blood fraction ζ_a is significantly smaller than the venous one ζ_v as shown in the middle column of Fig. 10.3, the ascending branch has lower values than the descending one and the loop is counter-clockwise. On the other hand, the loop is clockwise in the right column of Fig. 10.3, demonstrating a case with a larger arterial blood fraction ζ_a than the venous one ζ_v.

The role of increased dispersion in pathological tissue is illustrated in Fig. 10.3C with a transit time delay of 300 ms. Due to the increased dispersion, ΔR_2 values are reduced, predominantly for the venules, where the bolus arrives late. This partially compensates for the smaller arterial blood volume fraction in the voxel with the larger ζ_v (middle column of Fig. 10.3C) resulting in an intersection of the ascending and descending branches.

On the other hand, the dispersion causes a "rounder" loop in the voxel with larger ζ_a (right column of Fig. 10.3C).

10.3 Discussion

In this chapter, we interpreted the loop formed by the dynamic dependence of ΔR_{2GE} on $\Delta R_{2SE}^{3/2}$ found during the bolus passage in the double contrast DSC imaging. The complex cerebrovascular network was simplified as a vascular tree with multiple vessel generations. Assuming similarity of the vessel segments in the same generation, a single concentration curve was used for each vessel generation. Although veins were reported in physiological studies to have a different range of diameters than arteries, we used the same distributed diameters for the arterial and venous tree structure for simplifying the modelling and varied the arterial and venous blood volume fractions to introduce the difference between both compartments.

As shown in the results, the transport function in Eq. (10.2) has a low converging speed, which results a long tail. Therefore, a long time range (200 s) is required for calculation so that the integral of the transport function approaches to one. Moreover, the transport model is not applicable to capillaries due to the mixing of blood in the transverse direction by the red blood cells and by the transverse diffusion. Being a potential substitute, the vascular operator with a lagged exponential transport function used in the circulation model has often been assumed in studying vascular transport [106, 135]. However, this tissue-specific vascular operator was not appropriate for a vessel generation with extremely short transit time, e.g. 70 ms. The dispersion was too little in this case for assessing the difference in CA concentration between vessel generations. Although the selected transport function is not a perfect candidate to present the bolus passage in the vascular tree, it is sufficient for qualitative predictions of the loop in our study.

Although many factors are involved in the formation of the loop, the simulation suggested that it results from the chronological transition of the bolus among different blood vessel generations. The inflection point is reached when the bolus passed the capillaries. The capillary distribution is crucial for a large loop area, since their small diameter leads to the efficient relaxation of the SE. The direction of the loop is mainly affected by the relationship between arterial and venous blood volumes, which determines the relative

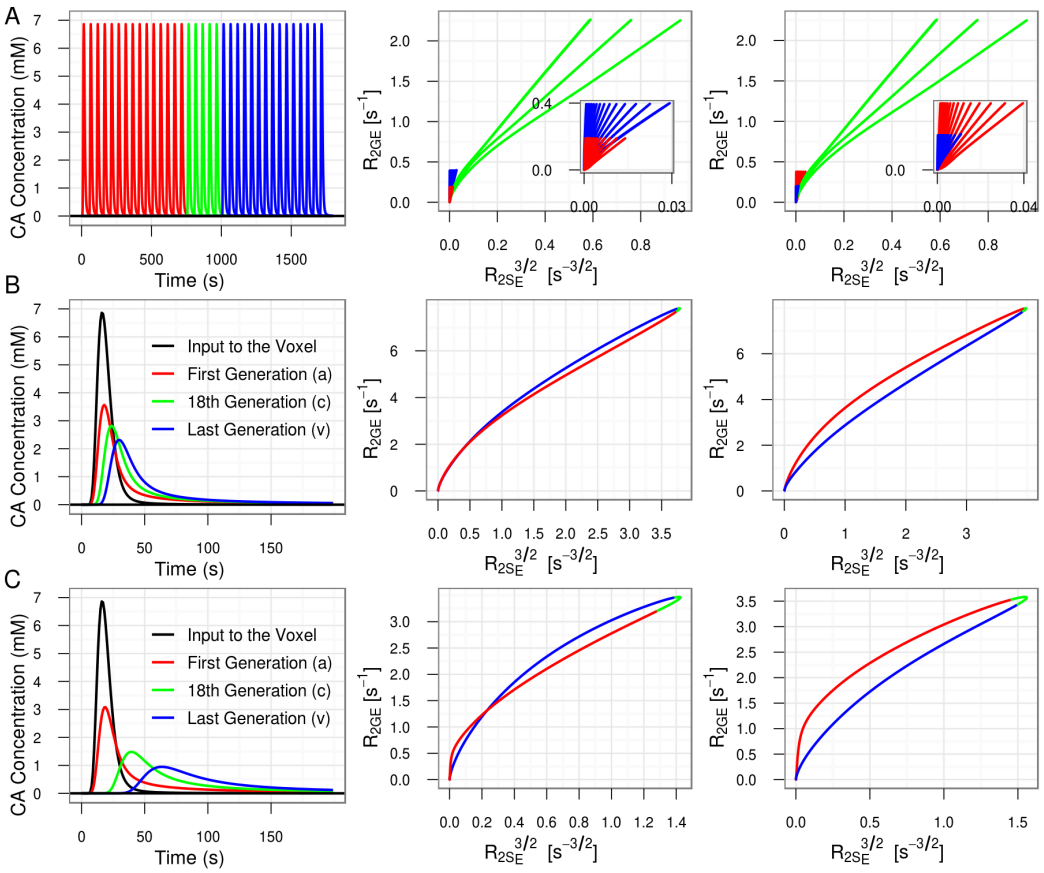

Figure 10.3: Results of the simulation in three transport systems: (A) unrealistic assumption of an infinitely long delay in the blood transport and no dispersion; (B) blood transport with a transit time of 70 ms; (C) blood transport with a transit time of 300 ms. The curves in red, green, and blue indicate that the peak of the bolus reaches an arteriole, a capillary, or a venule, respectively. Left column: the time-concentration curves in selected vessels of successive generations. Middle column: The loop of $\Delta R_{2GE}/\Delta R_{2SE}^{3/2}$ in a voxel with more venous blood ($\zeta_a = 0.5\%$, $\zeta_c = 2\%$, $\zeta_v = 1\%$). Right column: The loop of $\Delta R_{2GE}/\Delta R_{2SE}^{3/2}$ in a voxel with more arterial blood ($\zeta_a = 1\%$, $\zeta_c = 2\%$, $\zeta_v = 0.5\%$). The multiple curves in (A) are run forth and back to zero during the bolus passage through each vessel generation shown in the left column. The insert shows the region near the origin. Dispersion results in merging these trajectories in a single loop (B and C).

positions of the ascending and descending branches. The presence of deoxyhaemoglobin in venous blood only results in a slight change in the slope according to our simulation results. The bolus dispersion affects the shape of the loop in voxels with dominating arterial and venous contributions in a different way. It is not possible to quantify the influence of dispersion on the shape without the knowledge of the exact blood transport function through the vascular network.

Chapter 11

Characterization of the Loop

According to the simulation results in Chapter 10, the shape and direction of the loop depend on the blood composition and the dispersion, both of which vary between voxels. To characterize the voxel-specific loop, we introduce a post-processing method and a mapping parameter Λ, which provide additional information of cerebrovascular pathologies besides the conventional perfusion parameters.

11.1 Materials and Methods

11.1.1 MRI Measurements

Nine healthy volunteers (female 5; mean age 28 years, age range 25 - 40 years), four tumour patients, and thirteen acute stroke patients were included in this pilot study. The tumour pathologies were gemistocytic astrocytoma grade II, glioblastoma multiforme grade IV, hemangiopericytoma grade II, and transitional meningeoma grade I. All 13 acute stroke patients (female 5; mean age 77 years, age range 55 - 90 years) with an artery occlusion and perfusion deficit were examined within 4.5 hours from symptom onset. Detailed clinical data of the stroke patients have been reported in Table 7.1.

All studies were performed using a 3 T clinical scanner (TIM Trio, Siemens AG, Erlangen, Germany). The measurement was performed with a hybrid single-shot GE and SE EPI sequence with 50 repetitions (T_E (GE/SE), 22/85 ms; T_R, 1880 ms; field-of-view, 230 mm;

slice thickness, 5 mm; slice number, 16; matrix size, 64×64). A dose of 0.13 mL Gadovist (Bayer Schering Pharma AG, Berlin, Germany) per kg body weight was injected at a speed of 5 mL/s with a time delay of 18 s.

11.1.2 Data processing

The quantities ΔR_{2GE} and ΔR_{2SE} were converted from the signal drops after the CA administration for each scan by following

$$\Delta R_2(t) = -\frac{1}{T_E} \ln \frac{S(t)}{S_0}, \tag{4.6}$$

where $S(t)$ is the signal intensity recorded at time t, and S_0 is the averaged baseline signal over the time before CA administration (see Fig.7.1A and B for illustration). As shown in Fig. 7.1B, the recirculation results in a second passage in the relaxation rate curve, which is not of interest in characterizing the loop within this work. The extraction of the first bolus passage from the second one requires a minimum search between two subsequent peaks. In order to reduce the error in the temporal direction, both $\Delta R_{2GE}(t)$ and $\Delta R_{2SE}(t)$ curves were smoothed by a Gaussian filter in the Fourier domain, in which the standard deviation was chosen to be 1/3 of the sample rate. The minimum in the interval between two bolus passages can be identified as the first point after the peak where the first derivative computed from three points of the signal is zero [137].

The truncated unsmoothed curves of $\Delta R_{2GE}(t)$ and $\Delta R_{2SE}(t)$ were then used to explore the dynamic dependence of ΔR_{2GE} on $\Delta R_{2SE}^{3/2}$ (see Fig. 11.1). The ascending and descending branches were identified by separating the points before and after the maximum value of ΔR_{2GE}. For each branch, monotonic segments were taken into account for interpolation. Twenty evenly-distributed points were linearly interpolated along the $\Delta R_{2SE}^{3/2}$-axis for each branch. In case of an intersection between ascending and descending branches, the points with large ΔR_2 values beyond the intersection point were selected for further evaluation (Fig. 11.1B). The maximum distance l from the ascending branch to the descending one was calculated after the interpolation. Hence, l was positive if the values of the ascending branch exceeded those of the descending branch, i.e. the loop was clockwise. On the other hand, l was negative when the loop was counter-clockwise.

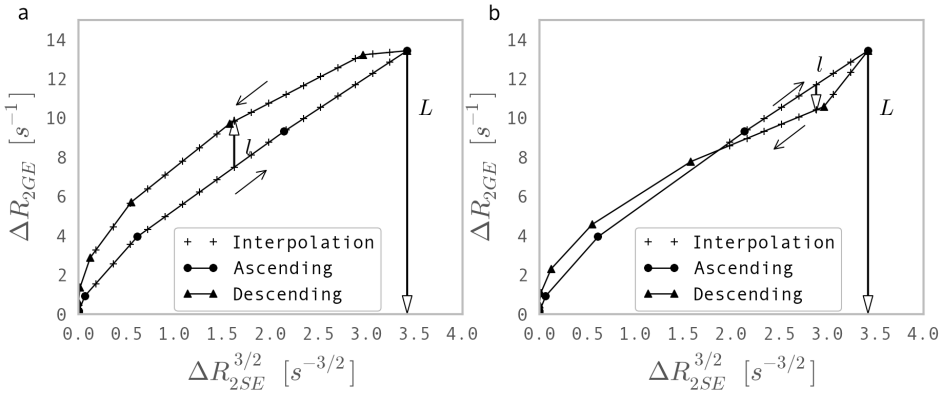

Figure 11.1: Definition of Λ as the maximum distance between ascending and descending branch of the loop (l) normalized by the maximum ΔR_{2GE} (L) in (A) a counter-clockwise loop without intersection and (B) a loop with intersection, for which the points with large ΔR_2 values beyond the intersection points are selected.

To characterize the shape of the loop, we introduced a parameter Λ as

$$\Lambda = \frac{l}{L}, \tag{11.1}$$

where L is the maximum value of ΔR_{2GE}. Therefore, Λ is in the range of (-1, 1) and its sign indicates the direction of the loop.

11.1.3 Volume of Interest

For healthy subjects, the entire brain excluding the space of the CSF was defined as the VOI for further evaluation. In tumour patients, the VOI of tumour tissue was manually delineated on T_1 images and coregistered to SE contrasts. The VOI of ischemic tissue in stroke patients was identified as the hyperintensities on the MTT map. The loops in a healthy brain, the tumour tissue in a tumour patient and the ischemic tissue in an acute stroke patient shown in the Fig. 11.2 were obtained from the averaged $\Delta R_{2GE}(t)$ and $\Delta R_{2SE}(t)$ values over pixels in each VOI.

11.2 Results

Fig. 11.2 shows examples of the averaged loop and the histogram of Λ in a healthy brain, a tumour, and the ischemic tissue from an acute stroke patient. The loop of the averaged $\Delta R_{2GE}(t)$ and $\Delta R_{2SE}^{3/2}(t)$ in a healthy brain is counter-clockwise (Fig. 11.2A). According to our simulation results, it indicates a higher venous blood fraction and a low level of dispersion in the whole brain. The corresponding histogram of Λ in Fig. 11.2A indicates that the majority of voxels had a negative Λ (mean $\pm$ standard deviation, -6.4% $\pm$ 37.6%).

The cerebrovascular pathology influenced the direction and the shape of the loop. Fig. 11.2B presents a clockwise averaged loop inside a tumour (hemangiopericytoma grade II, a patient from study [20]). The corresponding histogram of Λ in the tumour with a mean value of 21.4% $\pm$ 49.2% was shifted to more positive values compared to the healthy brain. The hyperintensity of Λ is displayed in the territory of the tumour in Fig. 11.3A.

In one acute stroke patient (male, 55 years; middle cerebral artery occlusion; time from symptom onset, 1.5 hours), the averaged loop in the ischemic region was also clockwise (Fig. 11.2C). There are more voxels with a positive Λ value than with negative ones in the histogram in Fig. 11.2C with a mean of 2.8% $\pm$ 41.1 %. In the stroke patient, the largest (positive) Λ values were observed in the region of increased CBV and MTT (Fig. 11.3B).

Fig. 11.4 shows the statistical results of three groups: healthy subjects, tumour patients and acute stroke patients. According to the student t-test ($p < 0.05$), the Λ in tumour (16.0 % $\pm$ 13.8 %) was significantly higher than that in the healthy brain (-4.5% $\pm$ 1.5 %) and that in the ischemic tissue of stroke patients (-2.7% $\pm$ 3.9%). No significant difference was found between the healthy brain and the ischemic tissue.

11.3 Discussion

Several ways can be used to characterize the shape of the loop, such as the area under the curve or the maximum distance l between the ascending and descending branches. However, both parameters are strongly influenced by the range of changes in the relaxation rates. Therefore, we introduced Λ as the ratio between l and the maximum ΔR_{2GE} (L)

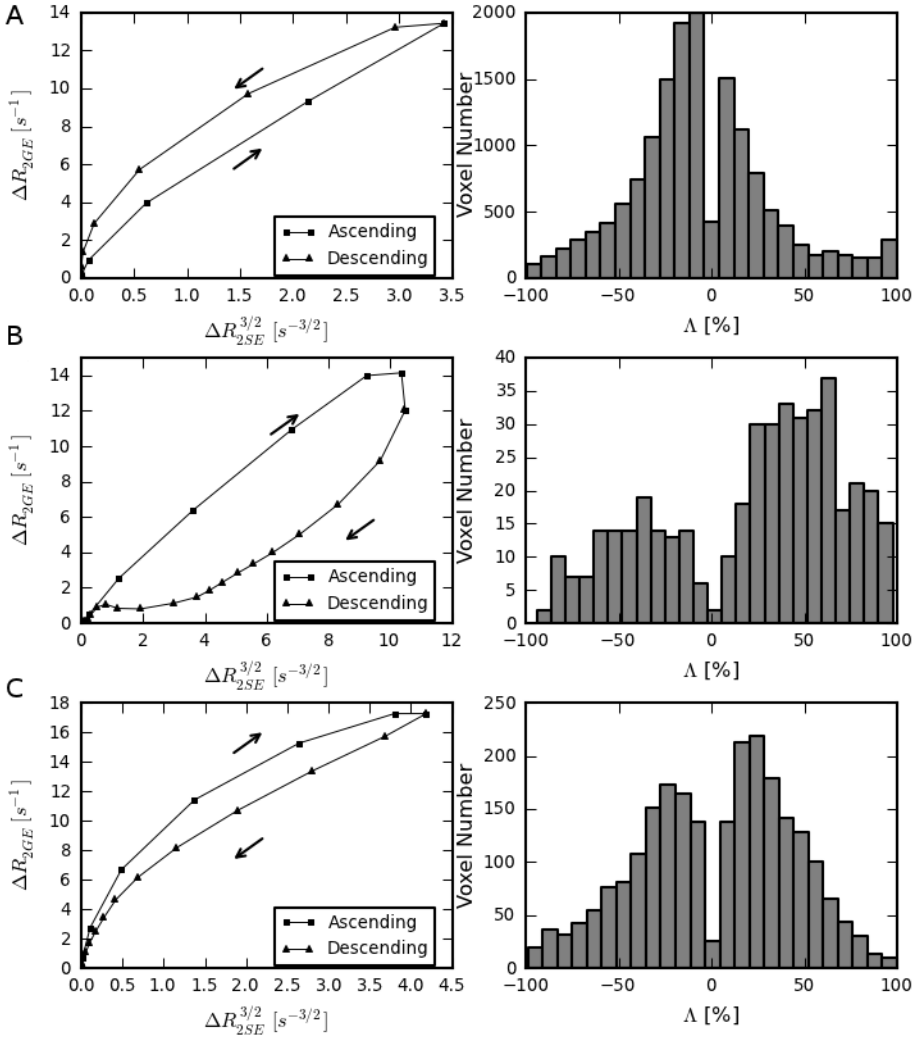

Figure 11.2: Examples of averaged loops (left column) and Λ (right column) in different types of tissue: (A) a healthy brain, (B) a hemangiopericytoma grade II, and (C) the ischemic tissue of an acute stroke patient.

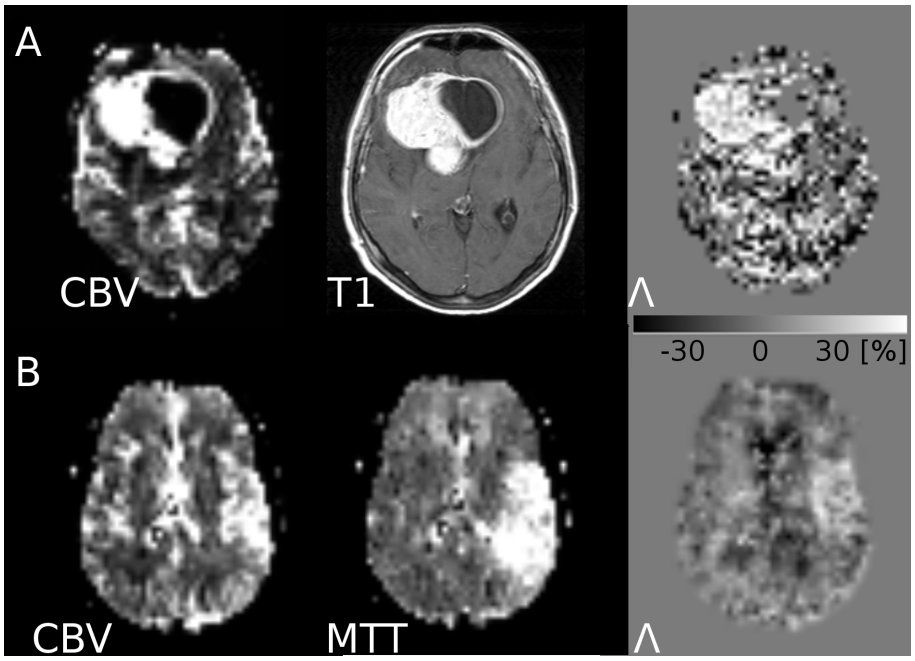

Figure 11.3: Illustration of images in a tumour patient (A) and an acute stroke patient (B) corresponding to the plots in Fig. 11.2B and C, respectively. (A) from left to right: cerebral blood volume (CBV), T_1 and Λ map; (B) from left to right: CBV, mean transit time (MTT) and Λ map.

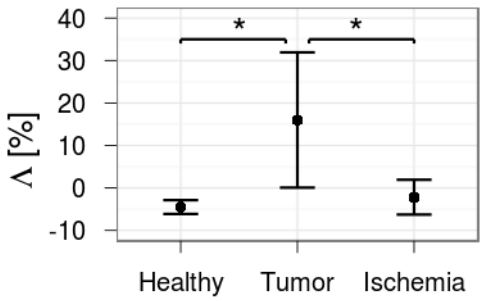

Figure 11.4: The statistic results of Λ values in different types of tissue. * indicates the significance $p < 0.05$. The value Λ in tumour (16.0 % ± 13.8 %) was significantly higher than that in the healthy brain (-4.5% ± 1.5 %) and in the ischemic tissue of stroke patients (-2.7% ± 3.9%)

for a normalization and thereby removed the influence from different degrees of variation in the CA concentration. A sufficient number of data points in the interpolation was necessary for a reliable measurement of Λ. Linear interpolation with 20 points was chosen as a compromise between processing speed and accuracy. The histogram of Λ values showed a wide distribution, since Λ additionally reflects the local vascular composition, which is very heterogeneous between voxels. Hence, if the voxel is dominated by a large vessel, the absolute value of Λ can be very large compared to its neighbours. Another characteristic of the histograms of Λ values is an indentation around $\Lambda = 0$. This is due to our definition of Λ being proportional to the maximum distance between the ascending and descending branch of the loop, which intrinsically favours non-zero values. We finally note that the occurrence of an intersection of both branches (as shown in the simulation results in the middle column of Fig. 10.3C, and the illustration in Fig. 11.1) complicates the assignment of a Λ value. In such cases, the maximum distance was computed for the loop segment of large ΔR_2 values beyond the intersection point because the portion of the loop near the inflection regions is less affected by dispersion.

In normal brain tissue, arterial blood volume is generally 50% smaller than venous blood volume [138]. This explains why the averaged loop in the healthy brain is counterclockwise and the majority of Λ values in the histogram of Fig. 11.2A is negative. The clockwise loop in the tumour that was found along with increased Λ values as compared to the healthy brain (Fig. 11.4) can be explained by an increase in arterial blood volume due to the oncogenic angiogenesis. A stronger dispersion in the pathological vasculartur further results in a larger loop area. The clockwise loop and elevated Λ values in the ischemic region observed in the stroke patients are most likely due to the strong dispersion resulting from a prolonged blood flow due to vessel occlusion. The vasodilatation of arterioles involved in the vasoregulation mechanism after stroke might also contribute to the elevation of the arterial branch of the loop, and thus cause a larger Λ value. However, if this effect is too subtle to compensate for the lower arterial blood volume compared to the venous fraction, it may not be sufficient to change the loop direction. In Fig. 11.4, the variation of Λ in ischemic tissue is larger than that in healthy brain. This might be explained by the different extent of dispersion and vasodilatation among patients. For strong bolus dispersion in voxels with a dominant arterial contribution, the descending (i.e. venous) branch of the loop would be shifted away from the ascending (i.e. arterial) branch towards smaller values, thus forming a clockwise loop, which increases l and leads to relatively large, positive Λ values. On the other hand, an intersection might occur

in the loop for voxels with a dominant venous distribution (subtle vasodilatation), so that the part of the loop beyond the intersection remains counter-clockwise (Fig. 10.3C, middle column) with a negative Λ value. The absolute value of this negative Λ for a strong bolus dispersion is likely larger than the normal blood transport, since l is divided by a reduced L.

As presented in Fig. 11.3, Λ is a novel imaging marker for characterizing the pathology of cerebrovascular structure by showing an increased mean value in tumour and a large variation range in ischemic tissue. The calculation of Λ does not include any complicated deconvolution process and is very intuitive compared to the conventional perfusion parameters. We note that the leakage of CA is often seen in tumour tissue and results in a pronounced tail in ΔR_{2GE} and ΔR_{2SE} after bolus passage. This effect needs to be corrected in the quantification of blood flow. However, the same effect is less important for the calculation of Λ, since the maximum distance between the ascending and descending branches is typically reached before the post-contrast state sets up. However, there are also certain drawbacks of Λ. The heterogeneity of Λ is a natural feature of the tissue, which may complicate the thresholding between the healthy and pathological tissue. For the area of infarction with very little amount of CA, the calculation of Λ often fails due to the non-monotonic changes of $\Delta R_{2GE}/\Delta R_{2SE}^{3/2}$ in the regions with a low SNR.

The quantification of perfusion parameters may also benefit from the calculation of Λ. Since the voxel dominated by an artery is characterized by a large Λ value, the analysis of Λ values may provide useful information for locating the AIF. However, it is to be investigated whether this could improve automated perfusion post-processing algorithms.

To sum up, the dynamic relaxation rates in DSC imaging could be well evaluated by using a simple vascular tree model. The differential blood volume in vessels of different types and the bolus dispersion influence the direction and the shape of the loop formed by the dynamic dependence between ΔR_{2GE} and $\Delta R_{2SE}^{3/2}$. The Λ value, defined as the maximum distance between ascending and descending branches of the loop normalized by the maximum ΔR_{2GE}, yields a simple and effective characterization of the loop, which may provide useful information in the description of cerebrovascular pathologies.

Part IV

Amide Proton Transfer Imaging

Chapter 12

Principles of Amide Proton Transfer Imaging

The APT imaging provides a sensitive detection mechanism that allows characterization of dilute labile protons in amide groups, which are usually undetectable by conventional MRI. In this chapter, we provide a brief review of the principle concepts involved in this technique.

12.1 Magnetization Transfer

In conventional proton MRI, image contrast is generated from the mobile protons in water and depends on their density and relaxation time. The mobile protons have a relatively long T_2 relaxation time in the order of milliseconds, which allows the signal acquisition in MRI after the direct excitation in the water pool. In the biological tissue, protons also exist with a less amount in the form of coupling with macromolecules. The T_2 of these protons with restricted mobility is too short, generally less than 1 ms, to allow the signal detection directly [139]. Since the absorption bandwidth is proportional to the inverse of T_2, the protons existing in macromolecules have a much broader absorption frequency range than those in water (Fig. 12.1).

Protons in different chemical environments have been found to interact and exchange between each other [140–142]. The exchange process between the restricted protons and the mobile ones can influence the spin state of the mobile protons, and thus varies the

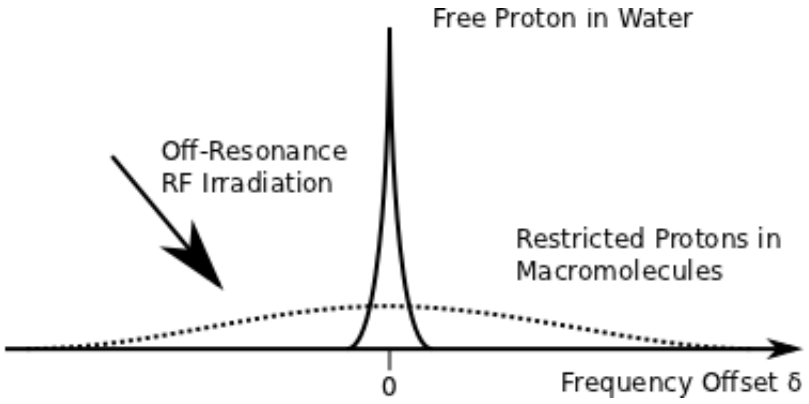

Figure 12.1: The schematic plot of the spectrum of two proton pools. The macromolecular protons, exhibiting much broader absorption range than the water protons, can be preferentially saturated using an off-resonance RF pulse. Image is modified from [139].

tissue contrast during imaging [143, 144]. Since the macromolecular spins have a broader absorption range than the mobile ones, they can be saturated by an off-resonance RF irradiation (Fig. 12.1). The exchange process transfers the saturation from the pool of restricted spins to the water pool and thus it suppresses the contrast obtained from the on-resonance excitation. The technique employing this exchange phenomenon is termed as magnetization transfer (MT), which was introduced by Wolff and Balaban [145] to characterize the exchange process in kidney and skeletal muscle.

In MRI, a magnetization transfer ratio (MTR) is used to quantify the amount of the MT with two sets of images: one without saturation, which has a signal intensity of S_0; one with the saturation of the macromolecular protons with an off-frequency offset δ, which has a signal intensity of S_{sat}. The MTR is defined as

$$\mathrm{MTR}(\delta) = \frac{S_0 - S_{sat}(\delta)}{S_0}. \tag{12.1}$$

We note that the frequency shift δ used through this chapter and the following one is referred to as parts per million (ppm) values with the reference of the resonance frequency of nuclei ^{1}H in water, which is different from the standard reference of tetramethylsilane at 0 ppm in ^{1}H NMR studies. Hence, the frequency shift of $\delta = 0$ ppm for water in this study corresponds to 4.7 ppm with the reference to tetramethylsilane. For a static magnetic field $B_0 = 3\,\mathrm{T}$, 1 ppm corresponds to a frequency shift of 127.8 Hz.

The MTR contrast has been widely used in clinical diagnosis of various diseases. Since

myelin in the brain possesses a large amount of restricted protons [146, 147], reduced MTRs can characterize the demyelinating process in multiple sclerosis [148]. Decreased MTR values have been found to associate with the aging and the cognitive impairment in patients with Alzheimer's disease [149–151].

In the molecular level, the MT effect between macromolecular and free mobile protons can be interpreted via two mechanisms [152, 153], which are illustrated in Fig. 12.2:

- In model A, magnetization passes between a macromolecule and the hydration water on the surface layer through the nuclear Overhauser effect, i.e. dipole-dipole interaction over a very short distance [154]. The hydration water molecules exchange consequently with the free bulk water. The MT interface is restricted to the sites with the relatively long-lived hydration water molecules [155, 156].
- In model B, exchangeable protons from hydroxyl (-OH), amine (-NH), or sulfhydryl (-SH) groups mediate the MT process between the non-exchangeable protons in the macromolecules and the bulk water. The MT interface locates in the site of the exchangeable protons of the macromolecular phase.

The contribution of these two mechanisms to the MT effect in biological tissue is unknown, since the qualification is complicated by the complex tissue structure. Notably, the later pathway is predominant in the MT process from small globular proteins and deoxyribonucleic acids to water due to the abundance of hydroxyl and amide groups in the chemical composition of these molecules. This mechanism is important for the concept of chemical exchange saturation transfer (CEST) that we introduce in the following section.

12.2 Chemical Exchange Saturation Transfer

Whereas the MT contrast originates mainly from the magnetization exchange between protons in the semisolid macromolecules and membranes and water protons, the CEST effect describes the exchange between labile protons and water protons. Labile protons generally locate in the hydrophilic chemical groups of the solute, for example, hydroxyl, amine, and amide protons [157–159]. Similarly to the MT process, the saturation of

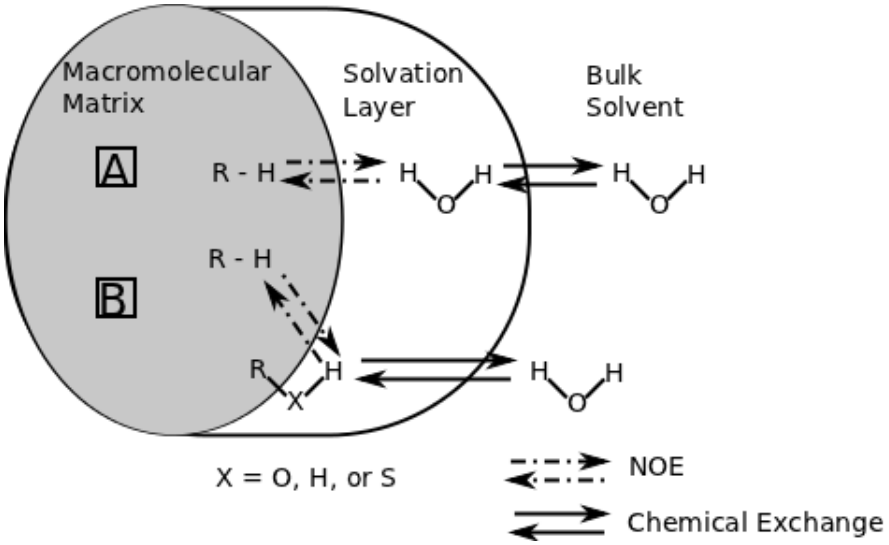

Figure 12.2: The schematic plot of two magnetization transfer (MT) exchange pathways. (A) The MT between the macromolecular phase and the free water via the exchange of hydration water molecules. (B) The MT via exchangeable protons from -OH, -NH, and -SH groups of the macromolecular phase. NOE indicates nuclear Overhauser effect. The figure is modified from [152, 153].

solute protons is first achieved by an off-resonance RF irradiation. The saturated protons accumulate in the water pool by the exchange between solute protons and water protons. This leads to a reduction of water signal after an on-resonance RF irradiation. The detection of the CEST effect replies on a high concentration of the solute and a large exchange rate from solute protons to water protons.

Since the target molecules are different between MT and CEST, the spectrum for RF saturation, conventionally named as the Z-spectrum, is in the different frequency range between these two effects (Fig. 12.3). Both MT and CEST spectrum display as a function of saturation frequency offset relative to water pool, which is defined as 0 ppm and 0 Hz. The MT effect is observed over a large range of offset frequencies in the order of 100 kHz, whereas CEST is usually detectable in a very narrow range of the chemical shift, which varies according to the type of CAs. For diamagnetic biological molecules with exchangeable protons, as an endogenous CEST agent, the chemical shift between exchangeable protons and bulk water is typically smaller than 5 ppm [160]. For some exogenous lanthanide agents, the shift can be several 10 ppm or several 100 ppm [161, 162]. As shown in Fig. 12.3B, the CEST spectrum shows a signal dip at a certain frequency range, which is not available at the opposite frequency. Hence, the asymmetric comparison of the signals at these two opposite frequencies is employed to assess the

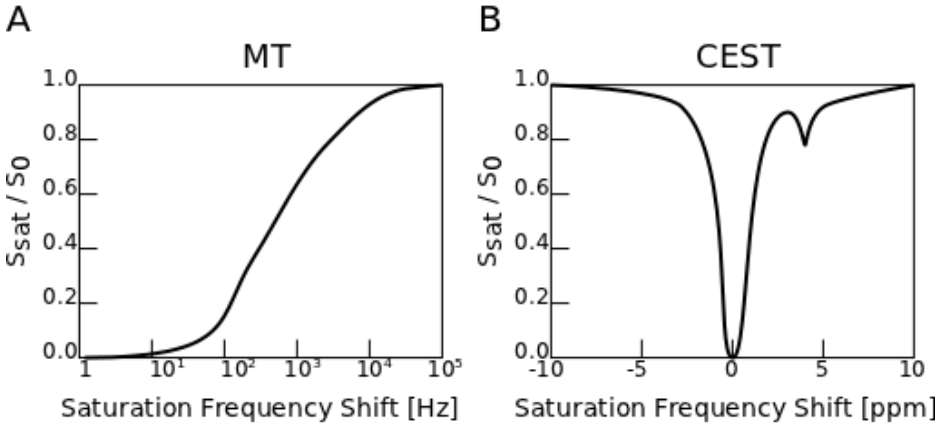

Figure 12.3: Illustration of typical Z-sprectra for magnetization transfer (MT) and chemical exchange saturation transfer (CEST) with a reference to the water resonance frequency. (A) The MT spectrum is generally measured at one side of off-frequency saturation in a broad range. (B) The CEST effect is usually assessed by the asymmetry between two sides of the saturation frequency offset in a narrow range.

CEST effect and is defined as $\mathrm{MTR}_{\mathrm{asym}}$:

$$\mathrm{MTR}_{\mathrm{asym}}(\delta) = \mathrm{MTR}(+\delta) - \mathrm{MTR}(-\delta) = \frac{S_{sat}(-\delta) - S_{sat}(+\delta)}{S_0}, \tag{12.2}$$

where δ is the frequency shift, S_0 is the signal intensity without saturation, and $S_{sat}(\delta)$ is the signal intensity with the saturation at the frequency shift of δ.

CEST is of great physiological interest, as it depends on the biochemical environment of tissue, such as the pH value, the salt and the metal content, and the concentration level of metabolic molecules.

12.3 Two-pool Model

The two-pool exchanging model for describing the MT effect between the restricted protons in macromolecules and the free protons in bulk water by coupled Bloch equations has been proved to be sufficient for a quantitative interpretation of the MT effect [142, 163–165]. Zhou et al. [166] adapted this model to obtain an analytic solution of the CEST process. As shown in Fig. 12.4, pool s represents a small mount of water-exchangeable solute protons, such as amide protons in mobile cellular proteins and peptides with a concentration in the order of mM. Pool w corresponds to the large pool of bulk water

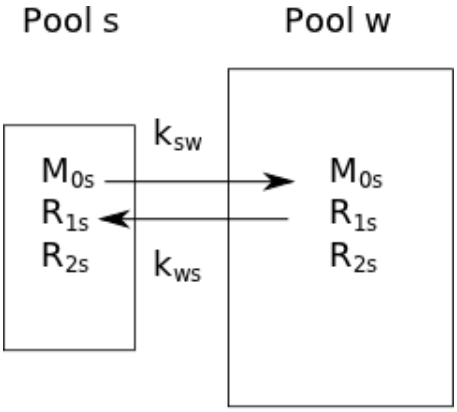

Figure 12.4: Schematic two-pool proton exchange model. The small pool (s) reflects water-exchangeable solute protons. The large pool (w) reflects bulk water protons. For each pool, R_1, R_2, and M_0 stand for spin-lattice relaxation rate, spin-spin relaxation rate, and equilibrium magnetization, respectively. The exchange rate from pool s to pool w is labelled as k_{sw}, and vice versa as k_{ws}. Figure is modified from [166].

protons. For each pool, R_1, R_2, and M_0 stand for spin-lattice relaxation rate, spin-spin relaxation rate, and equilibrium magnetization, respectively. The exchange rate from pool s to pool w is labelled as k_{sw}, and vice versa as k_{ws}. The spin frequency due to the applied RF pulse with a magnetic field strength B_1 corresponds to $\omega_1 = \gamma B_1$, where γ is the gyromagnetic ratio. The frequency offset of the RF pulse to the Larmor frequency of pool w and pool s is expressed as $\Delta\omega_w$ and $\Delta\omega_s$, respectively.

If the RF field is applied along the $\hat{x}$ direction in the rotation frame, the magnetization of both pools in each direction follows the coupled Bloch equations with exchange terms as

$$\frac{dM_{xs}}{dt} = -\Delta\omega_s M_{ys} - R_{2s} M_{xs} - k_{sw} M_{xs} + k_{ws} M_{xs}, \tag{12.3}$$

$$\frac{dM_{ys}}{dt} = \Delta\omega_s M_{xs} + \omega_1 M_{zs} - R_{2s} M_{ys} - k_{sw} M_{ys} + k_{ws} M_{yw}, \tag{12.4}$$

$$\frac{dM_{zs}}{dt} = -\omega_1 M_{ys} - R_{1s}(M_{zs} - M_{0s}) - k_{sw} M_{zs} + k_{ws} M_{zw}, \tag{12.5}$$

$$\frac{dM_{xw}}{dt} = -\Delta\omega_w M_{yw} - R_{2w} M_{xw} + k_{sw} M_{xs} - k_{ws} M_{xw}, \tag{12.6}$$

$$\frac{dM_{yw}}{dt} = \Delta\omega_w M_{xw} + \omega_1 M_{zw} - R_{2w} M_{yw} + k_{sw} M_{ys} - k_{ws} M_{yw}, \tag{12.7}$$

$$\frac{dM_{zw}}{dt} = -\omega_1 M_{yw} - R_{1w}(M_{zw} - M_{0w}) + k_{sw} M_{zs} - k_{ws} M_{zw}. \tag{12.8}$$

Th system under equilibrium obeys the relationship $k_{sw}M_{0s} = k_{ws}M_{0w}$. For MT and CEST experiments, we assume that the RF field is only applied to pool s and does not affect pool w. This leads to $\Delta\omega_s = 0$ and $\Delta\omega_w \to \infty$. Hence the effects of the $\Delta\omega_w$ and ω_1 terms in Eqs. (12.6) - (12.8) can be neglected.

To simplify Eqs. (12.3) - (12.8), several definitions are introduced here as

$$\begin{aligned} m_{zs} &= M_{zs} - M_{0s}, & r_{1s} &= R_{1s} + k_{sw}, & r_{2s} &= R_{2s} + k_{sw}, \\ m_{zw} &= M_{zw} - M_{0w}, & r_{1w} &= R_{1w} + k_{ws}, & r_{2w} &= R_{2w} + k_{ws}. \end{aligned} \tag{12.9}$$

The differential equations of magnetization in $\hat{y}$ and $\hat{z}$ direction in both pools are thus written as

$$\frac{dM_{ys}}{dt} = \omega_1 m_{zs} - r_{2s}M_{ys} + k_{ws}M_{yw} + \omega 1_1 M_{0s}, \tag{12.10}$$

$$\frac{dm_{zs}}{dt} = -\omega_1 M_{ys} - r_{1s}m_{zs} + k_{ws}m_{zw}, \tag{12.11}$$

$$\frac{dM_{yw}}{dt} = -r_{2w}M_{yw} + k_{sw}M_{ys}, \tag{12.12}$$

$$\frac{dm_{zw}}{dt} = -r_{1w}m_{zw} + k_{sw}m_{zs}. \tag{12.13}$$

By setting the left side of Eqs. (12.10) - (12.13) to zero, we get the steady-state (indexed with "ss") solutions of these four equations as following

$$m_{zs}^{ss} = -\frac{\omega_1^2 M_{0s}}{\omega_1^2 + pq}, \tag{12.14}$$

$$M_{ys}^{ss} = -\frac{\omega_1 q M_{0s}}{\omega_1^2 + pq}, \tag{12.15}$$

$$m_{zw}^{ss} = -\frac{k_{sw}}{r_{1w}} \frac{\omega_1^2 M_{0s},}{\omega_1^2 + pq} \tag{12.16}$$

$$M_{yw}^{ss} = -\frac{k_{sw}}{r_{2w}} \frac{\omega_1 q M_{0s}}{\omega_1^2 + pq}, \tag{12.17}$$

where $p = r_{2s} - (k_{sw}k_{ws}/r_{2w})$ and $q = r_{1s} - (k_{sw}k_{ws}/r_{1w})$.

In order to obtain the analytical solutions of Eqs. (12.10) - (12.13), we approximate the magnetization process in the CEST experiment with two separate steps: (1) the complete saturation of pool s, and (2) the transfer process of the saturation to pool w.

Assuming that pool s approaches a steady state m_{zs}^{ss} after the first step, pool w in the dynamic process of the second step can be described by

$$\frac{dm_{zw}}{dt} = -r_{1w}m_{zw} + k_{sw}m_{zs}^{ss}. \tag{12.18}$$

Hence, the solution for pool w takes the form of

$$m_{zw}(t) = \frac{k_{sw}m_{zs}^{ss}}{r_{1w}}[1 - e^{-r_{1w}(t-t_0)}] + m_{zw}(t_0)e^{-r_{1w}(t-t_0)}, \tag{12.19}$$

where t_0 is the initial time point in the second step when the saturation of pool s starts transferring to pool w. At the time of t_0, $M_{zw}(t_0)$ is still at the equilibrium value M_{0w}, thus $m_{zw}(t_0)$ is zero. The solution in Eq. (12.19) is rewritten as

$$m_{zw}(t) = \frac{k_{sw}m_{zs}^{ss}}{r_{1w}}[1 - e^{-r_{1w}(t-t_0)}]. \tag{12.20}$$

By combining Eq. (12.20) with Eqs. (12.9) and (12.14), the MTR in CEST experiments measuring the longitudinal magnetization of the water pool can be derived as

$$\begin{aligned} \mathrm{MTR} &= \frac{M_{0w} - M_{zw}(t_{sat})}{M_{0w}} = -\frac{m_{zw}(t_{sat})}{M_{0w}} \\ &= \frac{k_{sw}}{R_{1w} + k_{ws}} \frac{w_1^2}{w_1^2 + pq} \frac{M_{0s}}{M_{0w}}[1 - e^{-(R_{1w}+k_{ws})t_{sat}}], \end{aligned} \tag{12.21}$$

where $t_{sat} = t - t_0$. For a complement saturation under a strong RF field, $w_1^2/(w_1^2 + pq)$ can be considered as 1. Hence, Eq. (12.21) in this case takes the form of

$$\mathrm{MTR} = \frac{k_{sw}}{R_{1w} + k_{ws}} \frac{M_{0s}}{M_{0w}}[1 - e^{-(R_{1w}+k_{ws})t_{sat}}]. \tag{12.22}$$

12.4 Amide Proton Transfer Imaging and pH-weighted Contrast

The APT imaging is a type of the CEST imaging, in which the amide protons of mobile cellular proteins are labelled by the RF irradiation at the offset of 3.5 ppm from the water resonance frequency [21]. By eliminating the MT effect of the semisolid macromolecules expressed as $\mathrm{MTR}_{\mathrm{asym,MT}}$, the ratio of amide proton transfer (APTR) can be derived

from $\mathrm{MTR_{asym}}$ at 3.5 ppm:

$$\mathrm{APTR} = \mathrm{MTR_{asym}}(3.5\,\mathrm{ppm}) - \mathrm{MTR_{asym,MT}}. \tag{12.23}$$

Since the region of exchangeable protons ends from $\delta > 5$ ppm and $\mathrm{MTR_{asym}}$ become constant in this range as well, we can assume that the MT effect from macromolecules remains unaltered between at 3.5 ppm and in the range above 5 ppm. Hence, the $\mathrm{MTR_{asym,MT}}$ can be substituted by the value $\mathrm{MTR_{asym}}$ at $\delta > 5$ ppm.

From the two-pool model introduced in Section 12.3 for water (pool w) and amide protons (pool s) undergoing the chemical exchange, the APTR follows the solution in Eq. (12.22) under the assumption of the complete amide proton saturation. The back-exchange from the water protons (k_{ws}) to the protons in the solute proteins compared to the longitudinal relaxation rate of water (R_{1w}) is negligible for the endogenous APT according to the rat brain study ($k_{ws} \approx 0.02\ \mathrm{s}^{-1}$ and $R_{1w} \approx 0.7\ \mathrm{s}^{-1}$) [21]. Hence, the APTR is derived as

$$\mathrm{APTR} = \frac{k_{sw}[\text{amide proton}]}{R_{1w}[\text{water proton}]}(1 - e^{-R_{1w}t_{sat}}), \tag{12.24}$$

where R_{1w} is the spin-lattice relaxation rate of the water protons, t_{sat} is the saturation time, [amide proton]/[water proton] stands for the amide concentration, and k_{sw} is the exchange rate of the protons from the amide groups to the water, which is dependent on the pH value.

The amide proton exchange is catalysed by bases ($\mathrm{OH^-}$) [152, 167, 168], when the pH value in the solution is above 5, which is the range of pH in the biological tissue. So the higher the pH is, i.e. the higher the concentration of bases is, the faster the exchange rate k_{sw} is. Hence, the exchange rate k_{sw} in Eq. (12.24) takes the form of

$$k_{sw} = k_{\mathrm{OH^-}}[\mathrm{OH^-}] = k_{\mathrm{OH^-}} \times 10^{pH-pK_w} = 5.57 \times 10^{pH-6.4}, \tag{12.25}$$

where $k_{\mathrm{OH^-}}$ is the base-catalysed exchange rate. Its value of $5.57 \times 10^9\ \mathrm{s}^{-1}$ was assessed by fitting the *in vivo* and postmortem exchange rates versus the pH, using $pK_w = 15.4$ at 37 °C [169].

According to the equations deduced above, the calibration of the pH value requires the additional estimation of T_1 and the amide concentration besides the measurement of the

MTR_{asym}. Zhou et al. [21] determined these parameters for the rat brain and enabled the pH quantification in animal stroke models. However, it is not feasible so far to assess the amide concentration in human brain. The absolute quantification of pH value requires further validation under *in vivo* conditions whereas the pH-weighted contrast provided by the APT imaging method is more reliable given the abundance of amide protons in brain tissue.

Chapter 13

Amide Proton Transfer Imaging for Clinical Studies

The APT imaging has shown its capability of detecting ischemic acidosis in animal stroke models [21, 93]. However, the current imaging technique is limited in clinical stroke applications. In this chapter, we develop a new pulse sequence to overcome the technical limitation and apply it to subacute patients to achieve preliminary results.

13.1 Sequence Design

Since the chemical shift of mobile solute molecules, as an endogenous CEST CA, is as small as a few ppms, a successful CEST experiment demands a high spectral selectivity of the off-resonance saturation and thereby a long irradiation time, which often leads to a high energy deposition in the tissue, i.e. high specific absorption rate (SAR).

The effective saturation can be achieved by a continuous wave RF irradiation. Its implementation in clinical scanners is constrained by the limited length τ_p and the necessary duty-cycle η of RF pulses. The duty cycle is defined as

$$\eta = \tau_p/(\tau_p + \tau_d), \tag{13.1}$$

where τ_d is the interval delay between two saturation pulses. This technical problem can be solved by using a RF pulse train saturation as the substitute of the continuous

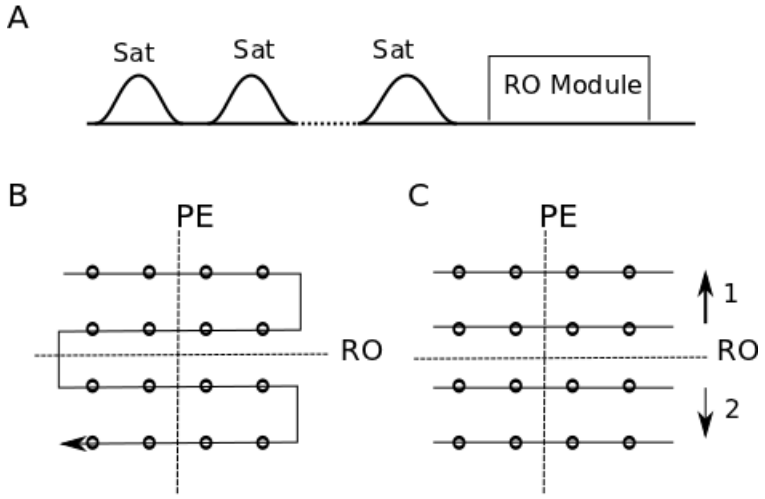

Figure 13.1: A brief illustration of conventional chemical exchange saturation transfer (CEST) sequences, which consist of a saturation pulse train and a readout module with (B) an echo planar imaging (EPI) readout or (C) a segmented turbo fast low angle shot (FLASH) readout. RO indicates readout; PE, phase encoding; Sat, saturation.

wave irradiation [93, 170, 171]. Both theoretical models and *in vivo* experimental data have reported that the effective saturation in MT experiments can be achieved by a pulse train [172–174] .

The best performance of the pulse train saturation is achieved by using the maximum pulse length τ_p, the largest duty cycle η, and a sufficient number of pulses in the train considering the SAR limitation in tissue. In our scanner (TIM Trio, Siemens, Erlangen, Germany), the maximum τ_p and the largest η are 100 ms and 50%, respectively [175]. While performing the pulse train, the scanner is in an idle status for half of the time, which can be used for the data acquisition to reduce the acquisition time.

Sequence designs so far employed in APT imaging studies were conventionally a RF pulse train followed by an EPI readout (Fig. 13.1B) [176, 177] or a segmented turbo fast low angle shot (FLASH) readout (Fig. 13.1C) [175]. Both readout schemes may lead to the loss of APT contrast, since the steady-state longitudinal magnetization may relax back to the equilibrium state due to the T_1 relaxation during the acquisition of central k-space lines after a delay of the saturation.

Additionally, the saturation frequency is often inaccurate due to the inhomogeneity of the main magnetic field [177]. A separate field-map scan is usually acquired for correction, which extents the acquisition time [93].

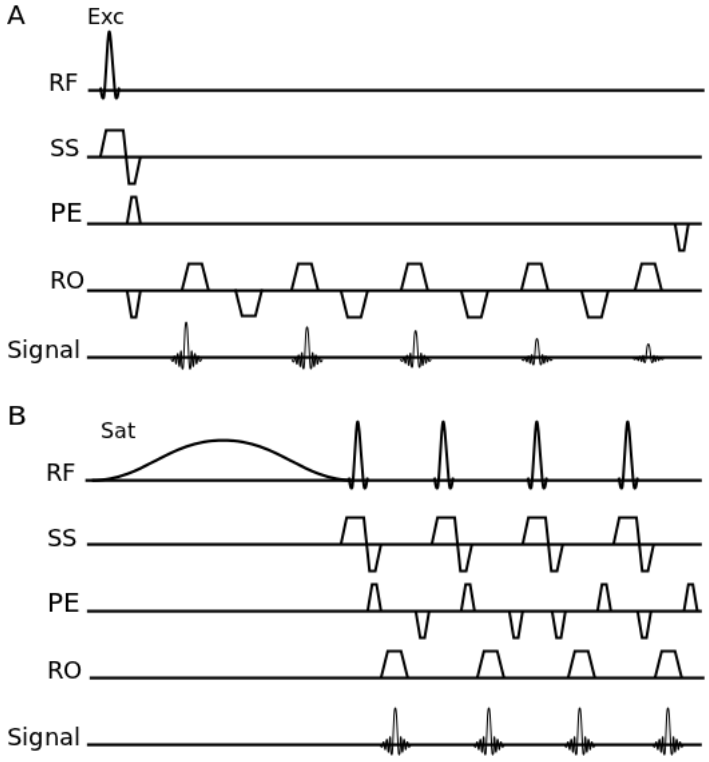

Figure 13.2: The sequence diagram: (A) the reference image acquisition with multiple echoes for field map reconstruction; (B) the chemical exchange saturation transfer (CEST) acquisition with turbo factor of 4. RF indicates radio frequency pulses; SS, slice selection; PE, phase encoding; RO, readout; Sat, saturation; Exc, excitation.

Considering the strict restriction of the scan time and the patient safety in clinical stroke studies, we made use of the idle time during the pulse train and developed a 3D pulse sequence with embedded field map information. As shown in Fig. 13.2, the sequence has two parts: (A) the reference image acquisition without saturation pulses; (B) the CEST image acquisition with off-resonance saturation pulses. To optimize the total acquisition time, a multiple GE readout was implemented in part (A) for measuring the T_2^* decay and computing the field map (Fig. 13.2A). Since there is a hard limit of the duty cycle ($\eta < 50\%$), T_R needed to be at least twice as long as any RF pulse included. A segmented turbo FLASH readout was implemented in the CEST part (B) to save measurement time by reducing the number of repetitions. A turbo factor of 4 is shown in the Fig. 13.2B. The partition-line space was acquired in an "edge-in" manner, i.e. in the order from the longest distance to the center to the shortest one, so that the central lines were recorded when the system had reached the steady state (see Fig. 13.3).

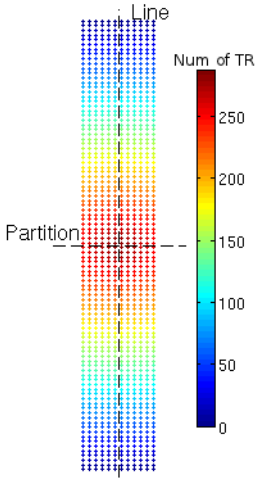

Figure 13.3: "Edge-in" acquisition order in partition-line space (96×12; turbo factor, 4) with the color coding of acquisition time. T_R indicates repetition time.

13.2 Preliminary Results in Clinical Use

The sequence introduced in Section 13.1 was first tested in a phantom and applied to two subacute stroke patients.

13.2.1 Material and methods

Phantom

A phantom with six tubes of 100 mM creatine in 100 mM phosphate-buffered saline at different pH values (5.6, 6.0, 6.3, 6.6, 6.8, and 7.2) was used. To adjust the relaxation times of the solutions toward physiologic ranges, 0.2% v/v Magnevist (Bayer Schering Pharma AG, Berlin, Germany) was added to the solution.

Sequence parameters included: T_R, 200 ms; T_E, 5 ms; saturation pulse duration, 100 ms; saturation pulse flip angle, 500°; range of frequency offset, from -2.5 ppm to 2.5 ppm with an increment of 0.1 ppm, voxel size, $1.5 \times 1.5 \times 5\,\mathrm{mm}^3$.

Patients

The clinical data of two stroke patients examined by the APT sequence are listed in Table 13.1. Sequence parameters included: T_R, 200 ms; T_E, 5 ms; saturation pulse

	Patient 1	Patient 2
Gender	M	F
Age (years)	65	74
NIHSS Administration	2	3
NIHSS Discharge	1	1
Scan Time from Symptom Onset (hours)	26 - 36	11 - 14
Site of Ischemia	Right MCA	Left MCA, Right ACA

Table 13.1: The clinical data of two stroke patients examined by the amide proton transfer (APT) sequence. NIHSS indicates national institutes of health stroke scale; MCA, middle cerebral artery; ACA, anterior cerebral artery.

duration, 100 ms; saturation pulse flip angle, 500°; saturation frequency offset, ±3, ±3.25, ±3.5, ±3.75, ±4 ppm; voxel size, $2 \times 2 \times 5\,\mathrm{mm}^3$; partition, 12; examination time, 6 mins.

Data Processing

The field map was calculated from the phase contrast of the multiple GEs. For each voxel, the Z-spectrum was interpolated and corrected according to the field map.

Since no macromolecules exist in the creatine solution to produce the MT effect, the $\mathrm{MTR}_{\mathrm{asym}}$ value was employed as the pH-weighted contrast in the phantom and calculated according to Eq. (12.2):

$$\mathrm{MTR}_{\mathrm{asym}}(\delta) = \frac{S_{sat}(-\delta) - S_{sat}(+\delta)}{S_0}. \tag{12.2}$$

The APTR value was used for the pH-weighted contrast in patients. According to Eq. (12.23), it can be obtained as the subtraction of the $\mathrm{MTR}_{\mathrm{asym}}$ measured at 3.5 ppm and > 5 ppm. However, in our experimental set-ups, 5 ppm was not covered in the frequency offset range, which was substituted by 4 ppm for data evaluation.

13.2.2 Results

Fig. 13.4A shows the Z-spectra and the $\mathrm{MTR}_{\mathrm{asym}}$ curves of the creatine solution at different pH values. Peaks with different amplitudes are observed at round 1.9 ppm downfield from water, where the amide protons of creatine resonate. The corresponding $\mathrm{MTR}_{\mathrm{asym}}$ map in Fig. 13.4C demonstrates a consistent change of $\mathrm{MTR}_{\mathrm{asym}}$ with the

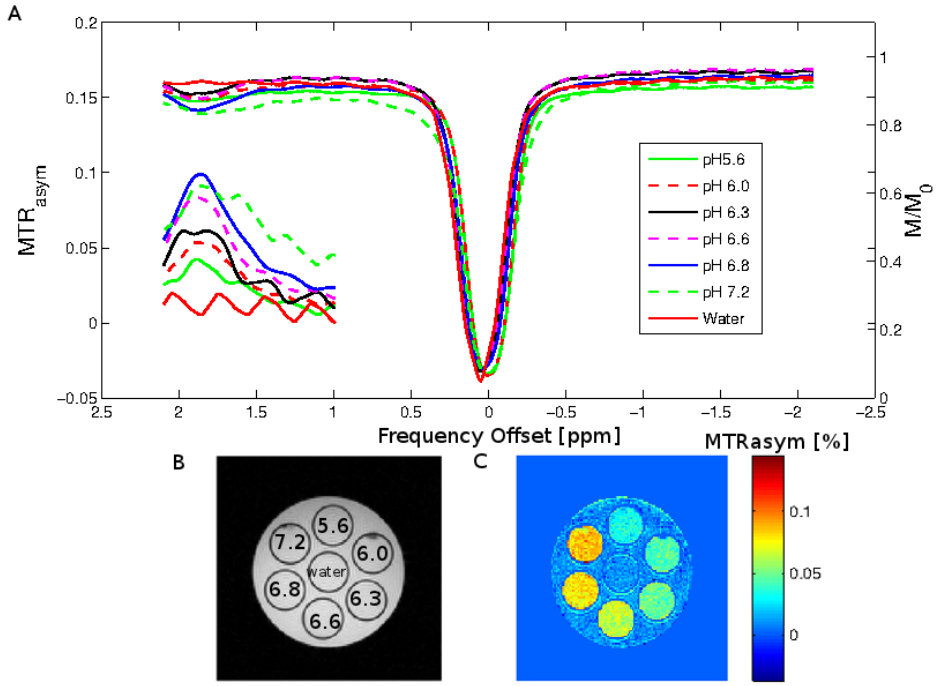

Figure 13.4: The result of phantom measurements. (A) Z-spectra and MTR_{asym} of creatine solution at six different pH values. (B) Reference image without saturation labelled with pH values. (C) The pH-weighted MTR_{asym} map of the phantom.

change in pH.

In patient 1, no predominant lesion growth is displayed by comparing the DWI map on day 2 to the FLAIR on day 5 (Fig. 13.5). The hypointensity of APTR measured on the second day after stroke is observed in the region of final infarction. As shown in Fig. 13.6, the infarction area grows significantly from the first day to the sixth day in patient 2. The hypointensity of the APTR matches the perfusion MTT deficit. This indicates that the tissue receives insufficient blood supply and is at risk of infarction.

13.3 Discussion

Clinical application of APT imaging has been limited, since it requires multiple scans with an off-resonance saturation, which leads to a long measurement time and a high SAR. In our study, we integrated a field-map measurement in the reference scan and introduced a turbo factor to accelerate the data acquisition during the RF off-duty time after each saturation pulse. The edge-in sampling scheme ensured that the central portion

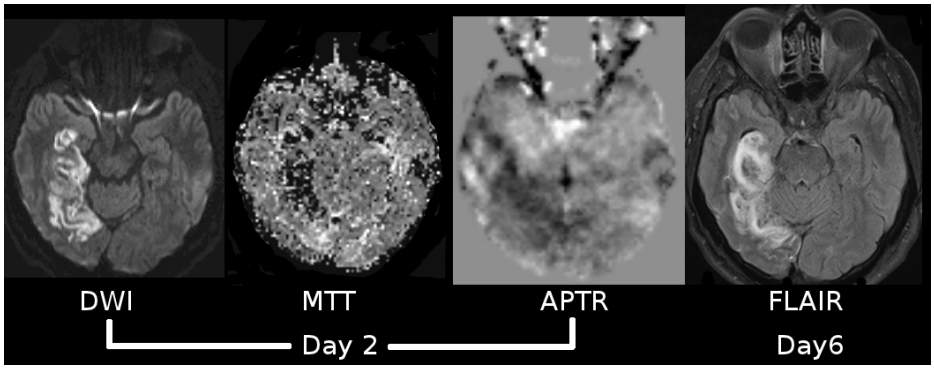

Figure 13.5: Maps of patient 1: diffusion-weighted imaging (DWI), mean transit time (MTT), and amide proton transfer ratio (APTR) measured on the second day, and fluid attenuation inversion recovery (FLAIR) measured on the sixth day after the symptom onset.

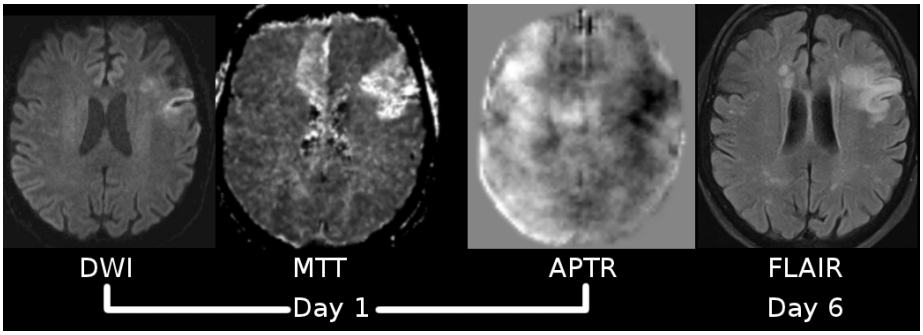

Figure 13.6: Maps of patient 2: diffusion-weighted imaging (DWI), mean transit time (MTT), and amide proton transfer ratio (APTR) measured on the first day, and fluid attenuation inversion recovery (FLAIR) measured on the sixth day after the symptom onset.

of k-space was acquired during the steady state. The acquisition of multiple partitions is necessary for achieving an effective saturation due to the sufficient number of k-space lines. For a small number of partitions or a single slice, it may be necessary to add dummy scans before the data acquisition to ensure the saturation of the center portion of k-space.

We note that the current pulse sequence design may result a potential quantification issue when a turbo factor larger than 2 is used. Multiple lines (e.g. 4 lines as shown in Fig. 13.2B) are acquired with a saturation preparation, but only a single k-space line is acquired in the reference acquisition without the CEST preparation. The basic contrast might slightly differ between both acquisitions due to the effect of using different number of RF pulses. Further investigations are needed to examine the subtle difference by comparing human brain images acquired with both schemes without saturation.

Although the usage of the RF off-duty time accelerates the data acquisition, the current examination time is still too long to integrate into the hyperacute stroke diagnosis. Further time reduction can be achieved by decreasing the offset-frequency samples. Since those samples serve for the correction of the magnetic field inhomogeneity, a better shimming protocol is necessary to be performed before the examination with a reduced number of samples.

Although the pH quantification is not possible without the measurement of T_1 and the amide proton concentration, $\mathrm{MTR}_{\mathrm{asym}}$ and APTR demonstrated the capability of pH value differentiation according to our results in phantom and patients, respectively. Preliminary hypointensities of APTR observed in the ischemic tissue and the infarction indicated a lower pH value, which matched previous animal results [21, 178]. This might be explained by accumulated lactate under ischemic conditions with an abnormal blood supply. However, the reliability of this parameter needs to be tested in a large patient cohort. It still remains unknown whether the ischemic acidosis indicates the final infarction. Therefore, further studies of APT imaging in stroke patients are necessary to explore the ischemic acidosis in more detail.

Part V

Summary and Outlook

Chapter 14

Summary

The aim of this work was to develop and study four novel imaging markers for characterization of the ischemic penumbra by employing two modern MRI techniques: vessel size imaging and APT imaging.

The estimation of the MVD and the mean vessel size, represented as Q and VSI, respectively, was available in vessel size imaging to characterize the morphological properties of microvasculature. In our feasibility study, these two parameters were assessed in nine healthy subjects and the results matched with general anatomical observation, i.e. the VSI in WM and GM was very similar and lower Q was observed in WM than in GM.

As the first study to apply vessel size imaging in acute stroke patients, our work found the reduced Q and increased VSI in the ischemic tissue of 75 patients examined within 24 hours from symptom onset. The Q showed a trend to identify the severity of ischemia in an overall voxel population of 23 patients with longitudinal follow-up scans.

During the study of vessel size imaging, we observed that dynamic changes in the transverse relaxation rates measured by the GE and the SE formed a loop on the $(\Delta R_{2SE}^{3/2}, \Delta R_{2GE})$ plane, rather than a reversible line as expected in the modelling for estimating the VSI. The shape of the loop and the direction of its passage differentiated between healthy brain and pathological tissue, such as tumour and ischemic tissue. By simulating the NMR signal in a vascular tree model of microvasculature, the direction of the loop was found to be influenced mainly by the arterial and venous blood composition, as well as dispersion. To characterize the direction and shape of the loop, we proposed a parameter Λ, as the maximum distance between the ascending and descending branches

of the loop normalized by the change in ΔR_{2GE}. The hyperintensities of Λ were observed in the ischemic tissue and tumour, which might be considered as a novel imaging marker for characterizing the pathology of cerebrovascular network.

The APT imaging provides an *in vivo* estimation of the pH value. However, its clinical application has been limited, since it requires multiple scans with an off-resonance saturation, which leads to a long measurement time and a high SAR. In this work, we designed a sequence integrated a field-map measurement in the reference scan and introduced a turbo factor to accelerate the data acquisition during the RF off-duty time after the saturation. The edge-in sampling scheme ensured that the central portion of k-space was acquired during the steady state. This technique was applied to two stroke patients to enable the pH-weighted APTR mapping for the first time in clinical stroke studies. Preliminary hypointensities of the APTR in the ischemic penumbra and the acute infarction suggested that the ischemic acidosis in the tissue may indicate the fate of infarction.

For vessel size imaging, the work mainly focused on adapting the imaging technique and the post-processing method for clinical acute stroke studies and assessing the response of Q and VSI to acute ischemia in a group of patients. The observation of the loop during processing the experimental data in vessel size imaging encouraged the vascular tree modelling and the simulation of NMR signals in DSC imaging. The parameter Λ was proposed to map the shape and the direction of the loop. Its clinical application was only briefly demonstrated in a few number of tumour and stroke patients.

For APT imaging, the work started with the sequence design, which was implemented in the Siemens-IDEA framework for the application in clinical scanners. Due to the time restriction of acute stroke management, this technique was preliminarily tested in two subacute stroke patients.

Chapter 15

Outlook

Clinical Stroke Application of Vessel Size Imaging

Our study has successfully accomplished dynamic GE and SE measurements in acute stroke patients by using a double-echo EPI sequence. However, this technique limited the time for readout gradients and thus restricted the image matrix to 64×64, resulting a large voxel size of $3.6 \times 3.6 \times 5\,\mathrm{mm}^3$. This resolution provided MTT maps with diagnostic value, but may not be sufficient for the examination of small infarctions. In the future work, employing modern techniques for imaging acceleration, such as parallel acquisition and partial Fourier reconstruction, may overcome this limitation. However, this demands extra implementation work to integrate these techniques into the current sequence and may reduce the image quantity to a great extent. In the application of current version of the imaging sequence, attempts can be made to obtain a smaller voxel size of $2.3 \times 2.3 \times 5\,\mathrm{mm}^3$ by adjusting to a matrix 84×84 and decrease the field-of-view to 192 mm. The reduction of the SNR may be compensated by increasing the dose of the CA.

Potential of Q in Predicting Lesion Growth

The parameter Q showed a trend to identify the severity of ischemia in an overall voxel population in 23 patients with follow-up scans. The potential of Q in predicting lesion growth needs to be further evaluated at a single case level. Apparently, a larger patient cohort with complete follow-up examinations is needed to reach the statistic significance. Given the heterogeneous occurrence and evolution of ischemic infarction, the status of reperfusion and recanalization requires to be clarified for subgrouping the patients. Further analysis may benefit from the differentiation between GM and WM, considering the

heterogeneity of Q in normal brain regions.

Modelling of the Vascular Network

We used a vascular tree model to simulate NMR signals and interpreted the formation of the loop on ($\Delta R_{2SE}^{3/2}$, ΔR_{2GE}) plane. The assumption of symmetric arterial and venous compartments in the morphology and the transportation of microvasculature was made for simplicity, which is not the case in the real vascular network. Further work may continue on approaching a more realistic model by following the data from pathological studies. The extremely long tail in the time-concentration curve seen in our simulation work was not the case for a real bolus passage. A more realistic transport function may be applied to reach an appropriate converging speed.

Possible Applications of the Loop and Λ

The shape of the loop and the direction of its passage differentiated between healthy brain and pathological tissue, which may be of interest in clinical usage. However, the heterogeneity of Λ is a natural feature of the tissue, which may complicate the thresholding between the healthy and pathological tissue. Studies in a large patient cohort may help to evaluate the diagnostic importance of the loop.

Since the voxel dominated by an artery is characterized by a large Λ value, the analysis of the loop may provide useful information for locating the AIF. This needs to be investigated by assessing the correlation between the Λ values and the location of arteries.

Clinical Application of Amide Proton Transfer Imaging

Although our implementation of the APT imaging sequence utilized the RF off-duty time, the scanning time was still too long for acute stroke management. Further time reduction can be achieved by decreasing the number of offset-frequency samples. Since those samples serve for the correction of the magnetic field inhomogeneity, a better shimming protocol is necessary to be performed before the examination. Scheidegger et al. [177] applied the saturation with a frequency-alternated RF irradiation and reported its improved robustness to the magnetic field inhomogeneity. Our sequence design may benefit from this method to reduce the number of off-frequency samples and thus overcome the time restriction in clinical stroke application.

According to our study in two subacute stroke patients, the hypointensity of the APTR

in the ischemic and infarcted tissue indicated a lower pH value. It needs to further investigated in a large patient cohort whether this effect correlates with the tissue fate.

Bibliography

[1] Donnan GA, Fisher M, Macleod M, Davis SM. Stroke. Lancet 2008;371:1612–1623.

[2] Adams H, Brott T, Crowell R, Furlan A, Gomez C, Grotta J, Helgason C, Marler J, Woolson R, Zivin J. Guidelines for the management of patients with acute ischemic stroke. A statement for healthcare professionals from a special writing group of the stroke council, american heart association. Circulation 1994;90:1588–1601.

[3] Adams HP, Brott TG, Furlan AJ, Gomez CR, Grotta J, Helgason CM, Kwiatkowski T, Lyden PD, Marler JR, Torner J, Feinberg W, Mayberg M, Thies W. Guidelines for thrombolytic therapy for acute stroke: A supplement to the guidelines for the management of patients with acute ischemic stroke. a statement for healthcare professionals from a special writing group of the stroke council, american heart association. Circulation 1996;94:1167–1174.

[4] Adams HP, Adams RJ, Brott T, del Zoppo GJ, Furlan A, Goldstein LB, Grubb RL, Higashida R, Kidwell C, Kwiatkowski TG, Marler JR, Hademenos GJ. Guidelines for the early management of patients with ischemic stroke. Stroke 2003;34:1056–1083.

[5] Simoons M, de Jaegere P, van Domburg R, Boersma E, Maggioni A, Franzosi M, Leimberger J, Califf R, Schröder R, Knatterud G, Braunwald E. Individual risk assessment for intracranial haemorrhage during thrombolytic therapy. Lancet 1993;342:1523–1528.

[6] Lauterbur P. Image formation by induced local interactions: Examples employing nuclear magnetic resonance. Nature 1973;242:190–191.

[7] Sorensen AG, Buonanno FS, Gonzalez RG, Schwamm LH, Lev MH, Huang-Hellinger FR, Reese TG, Weisskoff RM, Davis TL, Suwanwela N, Can U, Moreira JA, Copen WA, Look RB, Finklestein SP, Rosen BR, Koroshetz WJ. Hyperacute stroke: Evaluation with combined multisection diffusion-weighted and hemodynamically weighted echo-planar MR imaging. Radiology 1996;199:391–401.

[8] Warach S, Chien D, Li W, Ronthal M, Edelman RR. Fast magnetic resonance diffusionweighted imaging of acute human stroke. Neurology 1992;42:1717–1723.

[9] Schlaug G, Benfield A, Baird A, Siewert B, Lövblad K, Parker R, Edelman R, Warach S. The ischemic penumbra: operationally defined by diffusion and perfusion MRI. Neurology 1999;53:1528–1537.

[10] Schellinger PD, Fiebach JB, Hacke W. Imaging-based decision making in thrombolytic therapy for ischemic stroke. Stroke 2003;34:575–583.

[11] Kidwell CS, Alger JR, Saver JL. Beyond mismatch: Evolving paradigms in imaging the ischemic penumbra with multimodal magnetic resonance imaging. Stroke 2003; 34:2729–2735.

[12] Röther J, Schellinger PD, Gass A, Siebler M, Villringer A, Fiebach JB, Fiehler J, Jansen O, Kucinski T, Schoder V, Szabo K, Junge-Hülsing GJ, Hennerici M, Zeumer H, Sartor K, Weiller C, Hacke W. Effect of intravenous thrombolysis on MRI parameters and functional outcome in acute stroke <6 hours. Stroke 2002; 33:2438–2445.

[13] Astrup J, Siesjö BK, Symon L. Thresholds in cerebral ischemia - the ischemic penumbra. Stroke 1981;12:723–725.

[14] Nicoli F, Lefur Y, Denis B, Ranjeva J, Confort-Gouny S, Cozzone P. Metabolic counterpart of decreased apparent diffusion coefficient during hyperacute ischemic stroke. Stroke 2003;34:82–87.

[15] Guadagno JV, Warburton EA, Jones PS, Day DJ, Aigbirhio FI, Fryer TD, Harding S, Price CJ, Green HA, Barret O, Gillard JH, Baron JC. How affected is oxygen metabolism in DWI lesions? Neurology 2006;67:824–829.

[16] Fiehler J, Knudsen K, Kucinski T, Kidwell CS, Alger JR, Thomalla G, Eckert B, Wittkugel O, Weiller C, Zeumer H, Röther J. Predictors of apparent diffusion coefficient normalization in stroke patients. Stroke 2004;35:514–519.

[17] Sobesky J, Weber OZ, Lehnhardt F, Hesselmann V, Neveling M, Jacobs A, Heiss W. Does the mismatch match the penumbra? Magnetic resonance imaging and positron emission tomography in early ischemic stroke. Stroke 2005;36:980–985.

[18] Jensen J, Chandra R. MR imaging of microvasculature. Magn Reson Med 2000; 44:224–230.

[19] Tropres I, Grimault S, Vaeth A, Grillon E, Julien C, Payen JF, Lamalle L, Decorps M. Vessel size imaging. Magn Reson Med 2001;45:397–408.

[20] Kiselev VG, Strecker R, Ziyeh S, Speck O, Hennig J. Vessel size imaging in humans. Magn Reson Med 2005;53:553–563.

[21] Zhou J, Payen J, Wilson DA, Traystman RJ, van Zijl PCM. Using the amide proton signals of intracellular proteins and peptides to detect pH effects in MRI. Nat Med 2003;9:1085–1090.

[22] del Zoppo GJ, Mabuchi T. Cerebral microvessel responses to focal ischemia. J Cereb Blood Flow Metab 2003;23:879–894.

[23] Dirnagl U, Iadecola C, Moskowitz MA. Pathobiology of ischaemic stroke: an integrated view. Trends Neurosci 1999;22:391–397.

[24] Durukan A, Tatlisumak T. Acute ischemic stroke: Overview of major experimental rodent models, pathophysiology, and therapy of focal cerebral ischemia. Pharmacol Biochem Behav 2007;87:179–197.

[25] Levitt MH. Spin dynamics: basics of nuclear magnetic resonance. John Wiley & Sons, 2008.

[26] Dunn K, Bergman DJ, Latorraca GA. Nuclear magnetic resonance: petrophysical and logging applications. Elsevier, 2002.

[27] Bernstein MA, King KF, Zhou XJ. Handbook of MRI pulse sequences. Elsevier, 2004.

[28] Haacke EM. Magnetic resonance imaging: physical principles and sequence design. J. Wiley & Sons, 1999.

[29] Carr HY, Purcell EM. Effects of diffusion on free precession in nuclear magnetic resonance experiments. Phys Rev 1954;94:630–638.

[30] Meiboom S, Gill D. Modified spin-echo method for measuring nuclear relaxation times. Rev Sci Instrum 1958;29:688–691.

[31] Ogawa S, Lee TM, Kay AR, Tank DW. Brain magnetic resonance imaging with contrast dependent on blood oxygenation. Proc Natl Acad Sci U S A 1990;87:9868–9872.

[32] Rosen BR, Belliveau JW, Vevea JM, Brady TJ. Perfusion imaging with NMR contrast agents. Magn Reson Med 1990;14:249–265.

[33] Lauffer RB. Paramagnetic metal complexes as water proton relaxation agents for NMR imaging: theory and design. Chem Rev 1987;87:901–927.

[34] Strich G, Hagan PL, Gerber KH, Slutsky RA. Tissue distribution and magnetic resonance spin lattice relaxation effects of gadolinium-DTPA. Radiology 1985; 154:723–726.

[35] Koenig SH, Spiller M, Brown III RD, Wolf GL. Relaxation of water protons in the intra and extracellular regions of blood containing Gd(DTPA). Magn Reson Med 1986;3:791–795.

[36] Adams H, Bendixen B, Kappelle L, Biller J, Love B, Gordon D, Marsh E. Classification of subtype of acute ischemic stroke. definitions for use in a multicenter clinical trial. TOAST. trial of org 10172 in acute stroke treatment. Stroke 1993; 24:35–41.

[37] Einhäupl K, Villringer A, Mehraein S, Garner C, Pellkofer M, Haberl R, Pfister H, Schmiedek P, Meister W. Heparin treatment in sinus venous thrombosis. Lancet 1991;338:597–600.

[38] Connor S, Jarosz J. Magnetic resonance imaging of cerebral venous sinus thrombosis. Clin Radiol 2002;57:449–461.

[39] Timsit SG, Sacco RL, Mohr JP, Foulkes MA, Tatemichi TK, Wolf PA, Price TR, Hier DB. Brain infarction severity differs according to cardiac or arterial embolic source. Neurology 1993;43:728–733.

[40] Caplan LR, Wong KS, Gao S, Hennerici MG. Is hypoperfusion an important cause of strokes? If so, How? Cerebrovasc Dis 2006;21:145–153.

[41] Sacco RL, Adams R, Albers G, Alberts MJ, Benavente O, Furie K, Goldstein LB, Gorelick P, Halperin J, Harbaugh R, Johnston SC, Katzan I, Kelly-Hayes M, Kenton EJ, Marks M, Schwamm LH, Tomsick T. Guidelines for prevention of stroke in patients with ischemic stroke or transient ischemic attack. Circulation 2006;113:409–449.

[42] Grau AJ, Weimar C, Buggle F, Heinrich A, Goertler M, Neumaier S, Glahn J, Brandt T, Hacke W, Diener H, on behalf of the German Stroke Data Bank Collaborators. Risk factors, outcome, and treatment in subtypes of ischemic stroke. Stroke 2001;32:2559–2566.

[43] Petty GW, Brown RD, Whisnant JP, Sicks JD, OFallon WM, Wiebers DO. Ischemic stroke subtypes: A population-based study of functional outcome, survival, and recurrence. Stroke 2000;31:1062–1068.

[44] Mergenthaler P, Dirnagl U, Meisel A. Pathophysiology of stroke: lessons from animal models. Metab Brain Dis 2004;19:151–167.

[45] Wang Y, Xu T. Acidosis, acid-sensing ion channels, and neuronal cell death. Mol Neurobiol 2011;44:350–358.

[46] Sherwood TW, Lee KG, Gormley MG, Askwith CC. Heteromeric acid-sensing ion channels (ASICs) composed of ASIC2b and ASIC1a display novel channel properties and contribute to acidosis-induced neuronal death. J Neurosci 2011;31:9723–9734.

[47] Phan TG, Wright PM, Markus R, Howells DW, Davis SM, Donnan GA. Salvaging the ischaemic penumbra: More than just reperfusion? Clin Exp Pharmacol Physiol 2002;29:1–10.

[48] Price CJS, Warburton EA, Menon DK. Human cellular inflammation in the pathology of acute cerebral ischaemia. J Neurol Neurosurg Psychiatr 2003;74:1476–1484.

[49] McColl B, Allan S, Rothwell N. Systemic infection, inflammation and acute ischemic stroke. Neuroscience 2009;158:1049–1061.

[50] Broughton BR, Reutens DC, Sobey CG. Apoptotic mechanisms after cerebral ischemia. Stroke 2009;40:331–339.

[51] Ito U, Hakamata Y, Kawakami E, Oyanagi K. Temporary focal cerebral ischemia results in swollen astrocytic end-feet that compress microvessels and lead to focal cortical infarction. J Cereb Blood Flow Metab 2011;31:328–338.

[52] Gonzalez RG. Acute Ischemic Stroke: Imaging and Intervention. Springer, 2010.

[53] Hatcher MA, Starr JA. Role of tissue plasminogen activator in acute ischemic stroke. Ann Pharmacother 2011;45:364–371.

[54] Asplund K, Glader E, Norrving B, Eriksson M. Effects of extending the time window of thrombolysis to 4.5 hours: observations in the swedish stroke register (riks-stroke). Stroke 2011;42:2492–2497.

[55] Barber PA, Zhang J, Demchuk AM, Hill MD, Buchan AM. Why are stroke patients excluded from t-PA therapy? An analysis of patient eligibility. Neurology 2001; 56:1015–1020.

[56] Barber PA, Parsons MW, Desmond PM, Bennett DA, Donnan GA, Tress BM, Davis SM. The use of PWI and DWI measures in the design of "proof-of-concept" stroke trials. J Neuroimaging 2004;14:123–132.

[57] Hacke W, Albers G, Al-Rawi Y, Bogousslavsky J, Davalos A, Eliasziw M, Fischer M, Furlan A, Kaste M, Lees KR, Soehngen M, Warach S, for The DIAS Study Group. The desmoteplase in acute ischemic stroke trial (DIAS). Stroke 2005;36:66–73.

[58] Furlan AJ, Eyding D, Albers GW, Al-Rawi Y, Lees KR, Rowley HA, Sachara C, Soehngen M, Warach S, Hacke W, for the DEDAS Investigators. Dose escalation of desmoteplase for acute ischemic stroke (DEDAS). Stroke 2006;37:1227–1231.

[59] Guadagno JV, Warburton EA, Aigbirhio FI, Smielewski P, Fryer TD, Harding S, Price CJ, Gillard JH, Carpenter TA, Baron J. Does the acute diffusion-weighted imaging lesion represent penumbra as well as core? A combined quantitative PET/MRI voxel-based study. J Cereb Blood Flow Metab 2004;24:1249–1254.

[60] Heiss W, Sobesky J, Smekal U, Kracht LW, Lehnhardt F, Thiel A, Jacobs AH, Lackner K. Probability of cortical infarction predicted by flumazenil binding and diffusion-weighted imaging signal intensity: A comparative positron emission tomography/ magnetic resonance imaging study in early ischemic stroke. Stroke 2004; 35:1892–1898.

[61] Grandin CB, Duprez TP, Smith AM, Oppenheim C, Peeters A, Robert AR, Cosnard G. Which MR-derived perfusion parameters are the best predictors of infarct growth in hyperacute stroke? Comparative study between relative and quantitative measurements. Radiology 2002;223:361–370.

[62] Kudo K, Sasaki M, Ostergaard L, Christensen S, Uwano I, Suzuki M, Ogasawara K, Shirato H, Ogawa A. Susceptibility of Tmax to tracer delay on perfusion analysis: quantitative evaluation of various deconvolution algorithms using digital phantoms. J Cereb Blood Flow Metab 2011;31:908–912.

[63] Heiss W, Sobesky J, Hesselmann V. Identifying thresholds for penumbra and irreversible tissue damage. Stroke 2004;35:2671–2674.

[64] Butcher K, Parsons M, Baird T, Barber A, Donnan G, Desmond P, Tress B, Davis S. Perfusion thresholds in acute stroke thrombolysis. Stroke 2003;34:2159–2164.

[65] Galinovic I, Brunecker P, Ostwaldt A, Soemmer C, Hotter B, Fiebach JB. Fully automated postprocessing carries a risk of substantial overestimation of perfusion deficits in acute stroke magnetic resonance imaging. Cerebrovasc Dis 2011;31:408–413.

[66] Hotter B, Pittl S, Ebinger M, Oepen G, Jegzentis K, Kudo K, Rozanski M, Schmidt W, Brunecker P, Xu C, Martus P, Endres M, Jungehulsing G, Villringer A, Fiebach J. Prospective study on the mismatch concept in acute stroke patients within the first 24 h after symptom onset - 1000Plus study. BMC Neurol 2009;9:60.

[67] Korosec FR, Frayne R, Grist TM, Mistretta CA. Time-resolved contrast-enhanced 3D MR angiography. Magn Reson Med 1996;36:345–351.

[68] Laub G, Gaa J, Drobnitzky M. Magnetic resonance angiography techniques. Siemens Electromedica 1998;66:68–75.

[69] Wilson DL, Noble JA. An adaptive segmentation algorithm for time-of-flight MRA data. IEEE Trans Med Imag 1999;18:938–945.

[70] Essig M, Hawighorst H, Schoenberg SO, EngenhartCabillic R, Fuss M, Debus J, Zuna I, Knopp MV, van Kaick G. Fast fluidattenuated inversionrecovery (FLAIR) MRI in the assessment of intraaxial brain tumors. J Magn Reson Imaging 1998; 8:789–798.

[71] Husstedt HW, Sickert M, Köstler H, Haubitz B, Becker H. Diagnostic value of the fast-FLAIR sequence in MR imaging of intracranial tumors. Eur Radiol 2000; 10:745–752.

[72] Bachmann R, Reilmann R, Schwindt W, Kugel H, Heindel W, Krämer S. FLAIR imaging for multiple sclerosis: a comparative MR study at 1.5 and 3.0 Tesla. Eur Radiol 2006;16:915–921.

[73] Mori S, Barker PB. Diffusion magnetic resonance imaging: Its principle and applications. Anat Rec 1999;257:102–109.

[74] Villringer A, Rosen BR, Belliveau JW, Ackerman JL, Lauffer RB, Buxton RB, Chao Y, Wedeenand VJ, Brady TJ. Dynamic imaging with lanthanide chelates in normal brain: Contrast due to magnetic susceptibility effects. Magn Reson Med 1988;6:164–174.

[75] Ostergaard L, Sorensen AG, Kwong KK, Weisskoff RM, Gyldensted C, Rosen BR. High resolution measurement of cerebral blood flow using intravascular tracer bolus passages. part II: experimental comparison and preliminary results. Magn Reson Med 1996;36:726–736.

[76] Detre JA, Zhang W, Roberts DA, Silva AC, Williams DS, Grandis DJ, Koretsky AP, Leigh JS. Tissue specific perfusion imaging using arterial spin labeling. NMR Biomed 1994;7:75–82.

[77] Chalela JA, Alsop DC, Gonzalez-Atavales JB, Maldjian JA, Kasner SE, Detre JA. Magnetic resonance perfusion imaging in acute ischemic stroke using continuous arterial spin labeling. Stroke 2000;31:680–687.

[78] Hendrikse J, van Osch MJP, Rutgers DR, Bakker CJG, Kappelle LJ, Golay X, van der Grond J. Internal carotid artery occlusion assessed at pulsed arterial spin-labeling perfusion MR imaging at multiple delay times1. Radiology 2004;233:899–904.

[79] Petersen ET, Zimine I, Ho YL, Golay X. Non-invasive measurement of perfusion: a critical review of arterial spin labelling techniques. Br J Radiol 2006;79:688–701.

[80] Wintermark M, Albers GW, Alexandrov AV, Alger JR, Bammer R, Baron J, Davis S, Demaerschalk BM, Derdeyn CP, Donnan GA, Eastwood JD, Fiebach JB, Fisher M, Furie KL, Goldmakher GV, Hacke W, Kidwell CS, Kloska SP, Kohrmann M, Koroshetz W, Lee T, Lees KR, Lev MH, Liebeskind DS, Ostergaard L, Powers WJ, Provenzale J, Schellinger P, Silbergleit R, Sorensen AG, Wardlaw J, Wu O, Warach S. Acute stroke imaging research roadmap. Stroke 2008;39:1621–1628.

[81] Rivers C, Wardlaw J, Armitage P, Bastin M, Carpenter T, Cvoro V, Hand P, Dennis M. Do acute diffusion- and perfusion-weighted MRI lesions identify final infarct volume in ischemic stroke? Stroke 2006;37:98–104.

[82] Davis SM, Donnan GA. MR mismatch and thrombolysis: Appealing but validation required. Stroke 2009;40:2910.

[83] Fiebach JB, Schellinger PD. MR mismatch is useful for patient selection for thrombolysis: Yes. Stroke 2009;40:2906–2907.

[84] Schabitz W. MR mismatch is useful for patient selection for thrombolysis: No. Stroke 2009;40:2908–2909.

[85] Zhang ZG, Zhang L, Tsang W, Soltanian-Zadeh H, Morris D, Zhang R, Goussev A, Powers C, Yeich T, Chopp M. Correlation of VEGF and angiopoietin expression with disruption of Blood-Brain barrier and angiogenesis after focal cerebral ischemia. J Cereb Blood Flow Metab 2002;22:379–392.

[86] Liu D, Wu L, Breyer R, Mattson MP, Andreasson K. Neuroprotection by the PGE2 EP2 receptor in permanent focal cerebral ischemia. Ann Neurol 2005;57:758–761.

[87] Qu K, Chen CP, Halliwell B, Moore PK, Wong PT. Hydrogen sulfide is a mediator of cerebral ischemic damage. Stroke 2006;37:889–893.

[88] Veltkamp R, Rajapakse N, Robins G, Puskar M, Shimizu K, Busija D. Transient focal ischemia increases endothelial nitric oxide synthase in cerebral blood vessels. Stroke 2002;33:2704–2710.

[89] Bosomtwi A, Jiang Q, Ding GL, Zhang L, Zhang ZG, Lu M, Ewing JR, Chopp M. Quantitative evaluation of microvascular density after stroke in rats using MRI. J Cereb Blood Flow Metab 2008;28:1978–1987.

[90] Lin C, Chang C, Cheung W, Lin M, Chen J, Hsu CY, Chen J, Lin T. Dynamic changes in vascular permeability, cerebral blood volume, vascular density, and size after transient focal cerebral ischemia in rats: evaluation with contrast-enhanced magnetic resonance imaging. J Cereb Blood Flow Metab 2008;28:1491–1501.

[91] Hsu Y, Yang W, Lim K, Liu H. Vessel size imaging using dual contrast agent injections. J Magn Reson Imaging 2009;30:1078–1084.

[92] Höhn-Berlage M, Okada Y, Kloiber O, Hossmann KA. Imaging of brain tissue pH and metabolites. a new approach for the validation of volume-selective NMR spectroscopy. NMR Biomed 1989;2:240–245.

[93] Sun PZ, Benner T, Kumar A, Sorensen AG. Investigation of optimizing and translating pHsensitive pulsedchemical exchange saturation transfer (CEST) imaging to a 3T clinical scanner. Magn Reson Med 2008;60:834–841.

[94] Boxerman JL, Hamberg LM, Rosen BR, Weisskoff RM. MR contrast due to intravascular magnetic susceptibility perturbations. Magn Reson Med 1995;34:555–566.

[95] Kiselev VG, Posse S. Analytical theory of susceptibility induced NMR signal dephasing in a cerebrovascular network. Phys Rev Lett 1998;81:5696–5699.

[96] Yablonskiy DA, Haacke EM. Theory of NMR signal behavior in magnetically inhomogeneous tissues: the static dephasing regime. Magn Reson Med 1994;32:749–763.

[97] Kiselev VG, Posse S. Analytical model of susceptibility-induced MR signal dephasing: effect of diffusion in a microvascular network. Magn Reson Med 1999; 41:499–509.

[98] Kiselev VG. On the theoretical basis of perfusion measurements by dynamic susceptibility contrast MRI. Magn Reson Med 2001;46:1113–1122.

[99] Wu EX, Tang H, Jensen JH. High-resolution MR imaging of mouse brain microvasculature using the relaxation rate shift index Q. NMR Biomed 2004;17:507–512.

[100] Jensen JH, Lu H, Inglese M. Microvessel density estimation in the human brain by means of dynamic contrast-enhanced echo-planar imaging. Magn Reson Med 2006; 56:1145–1150.

[101] Ungersma SE, Pacheco G, Ho C, Yee SF, Ross J, Bruggen Nv, Jr Peale FVVP, Ross S, Carano RAD. Vessel imaging with viable tumor analysis for quantification of tumor angiogenesis. Magn Reson Med 2010;63:1637–1647.

[102] Valable S, Lemasson B, Farion R, Beaumont M, Segebarth C, Remy C, Barbier EL. Assessment of blood volume, vessel size, and the expression of angiogenic factors in two rat glioma models: a longitudinal in vivo and ex vivo study. NMR Biomed 2008;21:1043–1056.

[103] Zwick S, Strecker R, Kiselev V, Gall P, Huppert J, Palmowski M, Lederle W, Woenne EC, Hengerer A, Taupitz M, Semmler W, Kiessling F. Assessment of vascular remodeling under antiangiogenic therapy using DCE-MRI and vessel size imaging. J Magn Reson Imaging 2009;29:1125–1133.

[104] Ebinger M, Brunecker P, Jungehulsing GJ, Malzahn U, Kunze C, Endres M, Fiebach JB. Reliable perfusion maps in stroke MRI using arterial input functions derived from distal middle cerebral artery branches. Stroke 2010;41:95–101.

[105] Gall P, Emerich P, Kjølby B, Kellner E, Mader I, Kiselev V. On the design of filters for fourier and oSVD-based deconvolution in bolus tracking perfusion MRI. Magn Reson Mater Phy 2010;23:187–195.

[106] Ostergaard L, Chesler DA, Weisskoff RM, Sorensen AG, Rosen BR. Modeling cerebral blood flow and flow heterogeneity from magnetic resonance residue data. J Cereb Blood Flow Metab 1999;19:690–699.

[107] Zaro-Weber O, Moeller-Hartmann W, Heiss W, Sobesky J. MRI perfusion maps in acute stroke validated with 15O-water positron emission tomography. Stroke 2010; 41:443–449.

[108] Dennie J, Mandeville JB, Boxerman JL, Packard SD, Rosen BR, Weisskoff RM. NMR imaging of changes in vascular morphology due to tumor angiogenesis. Magn Reson Med 1998;40:793–799.

[109] Griswold MA, Jakob PM, Heidemann RM, Nittka M, Jellus V, Wang J, Kiefer B, Haase A. Generalized autocalibrating partially parallel acquisitions (GRAPPA). Magn Reson Med 2002;47:1202–1210.

[110] Jochimsen TH, Ivanov D, Heinke W, Turner R, Möller HE, Reichenbach JR. Whole-brain mapping of venous vessel size in humans using the hypercapnia-induced BOLD effect. Neuroimage 2010;51:765–774.

[111] Cavaglia M, Dombrowski SM, Drazba J, Vasanji A, Bokesch PM, Janigro D. Regional variation in brain capillary density and vascular response to ischemia. Brain Res 2001;910:81–93.

[112] Zhao F, Wang P, Hendrich K, Ugurbil K, Kim S. Cortical layer-dependent BOLD and CBV responses measured by spin-echo and gradient-echo fMRI: insights into hemodynamic regulation. Neuroimage 2006;30:1149–1160.

[113] Powers WJ. Cerebral hemodynamics in ischemic cerebrovascular disease. Ann Neurol 1991;29:231–240.

[114] Le Bihan D, Poupon C, Amadon A, Lethimonnier F. Artifacts and pitfalls in diffusion MRI. J Magn Reson Imaging 2006;24:478–488.

[115] Murray AD, Staff RT, Shenkin SD, Deary IJ, Starr JM, Whalley LJ. Brain white matter hyperintensities: Relative importance of vascular risk factors in nondemented elderly people. Radiology 2005;237:251–257.

[116] Xu C, Schmidt WUH, Villringer K, Brunecker P, Kiselev V, Gall P, Fiebach JB. Vessel size imaging reveals pathological changes of microvessel density and size in acute ischemia. J Cereb Blood Flow Metab 2011;31:1687–1695.

[117] Grandin CB, Duprez TP, Smith AM, Mataigne F, Peeters A, Oppenheim C, Cosnard G. Usefulness of magnetic resonance-derived quantitative measurements of cerebral blood flow and volume in prediction of infarct growth in hyperacute stroke. Stroke 2001;32:1147–1153.

[118] Darby DG, Barber PA, Gerraty RP, Desmond PM, Yang Q, Parsons M, Li T, Tress BM, Davis SM. Pathophysiological topography of acute ischemia by combined diffusion-weighted and perfusion MRI. Stroke 1999;30:2043–2052.

[119] Galinovic I, Ostwaldt A, Soemmer C, Bros H, Hotter B, Brunecker P, Schmidt WU, Jungehülsing J, Fiebach JB. Search for a map and threshold in perfusion MRI to accurately predict tissue fate: a protocol for assessing lesion growth in patients with persistent vessel occlusion. Cerebrovasc Dis 2011;32:186–193.

[120] Campbell BCV, Christensen S, Foster SJ, Desmond PM, Parsons MW, Butcher KS, Barber PA, Levi CR, Bladin CF, Donnan GA, Davis SM. Visual assessment of perfusion-diffusion mismatch is inadequate to select patients for thrombolysis. Cerebrovasc Dis 2010;29:592–596.

[121] Calamante F, Christensen S, Desmond PM, Østergaard L, Davis SM, Connelly A. The physiological significance of the time-to-maximum (Tmax) parameter in perfusion MRI. Stroke 2010;41:1169–1174.

[122] Jochimsen TH, Möller HE. Increasing specificity in functional magnetic resonance imaging by estimation of vessel size based on changes in blood oxygenation. Neuroimage 2008;40:228–236.

[123] Donahue KM, Krouwer HG, Rand SD, Pathak AP, Marszalkowski CS, Censky SC, Prost RW. Utility of simultaneously acquired gradient-echo and spin-echo cerebral blood volume and morphology maps in brain tumor patients. Magn Reson Med 2000;43:845–853.

[124] Ogawa S, Menon R, Tank D, Kim S, Merkle H, Ellermann J, Ugurbil K. Functional brain mapping by blood oxygenation level-dependent contrast magnetic resonance imaging. a comparison of signal characteristics with a biophysical model. Biophys J 1993;64:803–812.

[125] van Osch MJP, Vonken EPA, Wu O, Viergever MA, van der Grond J, Bakker CJG. Model of the human vasculature for studying the influence of contrast injection speed on cerebral perfusion MRI. Magn Reson Med 2003;50:614–622.

[126] Mouridsen K, Friston K, Hjort N, Gyldensted L, Østergaard L, Kiebel S. Bayesian estimation of cerebral perfusion using a physiological model of microvasculature. Neuroimage 2006;33:570–579.

[127] Gall P, Petersen E, Golay X, Kiselev V. Delay and dispersion in DSC perfusion derived from a vascular tree model predicts ASL measurements. In ISMRM 16th Annual Scientific Meeting Proceedings. Toronto, Canada, 2008 p. 627.

[128] Gall P, Kiselev V. On the form of the residue function for brain tissue. In ISMRM-ESMRMB Joint 18th Annual Scientific Meeting Proceedings. Stockholm, Sweden, 2010 p. 1795.

[129] Gall P, Guether M, Kiselev V. Model of blood transport couples delay and dispersion and predicts ASL bolus measurements. In ISMRM-ESMRMB Joint 18th Annual Scientific Meeting Proceedings. Stockholm, Sweden, 2010 p. 1736.

[130] Turner R. How much cortex can a vein drain? Downstream dilution of activation-related cerebral blood oxygenation changes. Neuroimage 2002;16:1062–1067.

[131] Murray CD. The physiological principle of minimum work. Proc Natl Acad Sci U S A 1926;12:207–214.

[132] Serrador JM, Picot PA, Rutt BK, Shoemaker JK, Bondar RL. MRI measures of middle cerebral artery diameter in conscious humans during simulated orthostasis. Stroke 2000;31:1672–1678.

[133] Lauwers F, Cassot F, Lauwers-Cances V, Puwanarajah P, Duvernoy H. Morphometry of the human cerebral cortex microcirculation: General characteristics and space-related profiles. Neuroimage 2008;39:936–948.

[134] Pawlik G, Rackl A, Bing RJ. Quantitative capillary topography and blood flow in the cerebral cortex of cats: an in vivo microscopic study. Brain Res 1981;208:35–58.

[135] King RB, Deussen A, Raymond GM, Bassingthwaighte JB. A vascular transport operator. Am J Physiol Heart Circ Physio 1993;265:2196–2208.

[136] Leggett R, Williams L. A proposed blood circulation model for reference man. Health Phys 1995;69:187–201.

[137] Gall P, Mader I, Kiselev VG. Extraction of the first bolus passage in dynamic susceptibility contrast perfusion measurements. Magn Reson Mater Phy 2009;22:241–249.

[138] Ito H, Kanno I, Iida H, Hatazawa J, Shimosegawa E, Tamura H, Okudera T. Arterial fraction of cerebral blood volume in humans measured by positron emission tomography. Ann Nucl Med 2001;15:111–116.

[139] Henkelman RM, Stanisz GJ, Graham SJ. Magnetization transfer in MRI: a review. NMR Biomed 2001;14:57–64.

[140] Solomon I. Relaxation processes in a system of two spins. Phys Rev 1955;99:559–565.

[141] Solomon I, Bloembergen N. Nuclear magnetic interactions in the HF molecule. J Chem Phys 1956;25:261–266.

[142] Forsen S, Hoffman RA. Study of moderately rapid chemical exchange reactions by means of nuclear magnetic double resonance. J Chem Phys 1963;39:2892–2901.

[143] Edzes HT, Samulski ET. The measurement of cross-relaxation effects in the proton NMR spin-lattice relaxation of water in biological systems: Hydrated collagen and muscle. Journal of Magnetic Resonance (1969) 1978;31:207–229.

[144] Hoffman RA. Transient and steady-state overhauser experiments in the investigation of relaxation processes. analogies between chemical exchange and relaxation. J Chem Phys 1966;45:2049–2060.

[145] Wolff SD, Balaban RS. Magnetization transfer contrast (MTC) and tissue water proton relaxation in vivo. Magn Reson Med 1989;10:135–144.

[146] Fralix TA, Ceckler TL, Wolff SD, Simon SA, Balaban RS. Lipid bilayer and water proton magnetization transfer: Effect of cholesterol. Magn Reson Med 1991;18:214–223.

[147] Koenig SH. Cholesterol of myelin is the determinant of graywhite contrast in MRI of brain. Magn Reson Med 1991;20:285–291.

[148] Dousset V, Grossman RI, Ramer KN, Schnall MD, Young LH, Gonzalez-Scarano F, Lavi E, Cohen JA. Experimental allergic encephalomyelitis and multiple sclerosis: lesion characterization with magnetization transfer imaging. Radiology 1992; 182:483–491.

[149] Bozzali M, Franceschi M, Falini A, Pontesilli S, Cercignani M, Magnani G, Scotti G, Comi G, Filippi M. Quantification of tissue damage in AD using diffusion tensor and magnetization transfer MRI. Neurology 2001;57:1135–1137.

[150] Ridha B, Symms M, Tozer D, Stockton K, Frost C, Siddique M, Lewis E, MacManus D, Boulby P, Barker G, Rossor M, Fox N, Tofts P. Magnetization transfer ratio in Alzheimer disease: Comparison with volumetric measurements. AJNR Am J Neuroradiol 2007;28:965–970.

[151] Hanyu H, Asano T, Iwamoto T, Takasaki M, Shindo H, Abe K. Magnetization transfer measurements of the hippocampus in patients with Alzheimer's disease, vascular dementia, and other types of dementia. AJNR Am J Neuroradiol 2000; 21:1235–1242.

[152] Liepinsh E, Otting G. Proton exchange rates from amino acid side chains implications for image contrast. Magn Reson Med 1996;35:30–42.

[153] Ceckler T, Maneval J, Melkowits B. Modeling magnetization transfer using a three-pool model and physically meaningful constraints on the fitting parameters. J Magn Reson 2001;151:9–27.

[154] Anderson WA, Freeman R. Influence of a second radiofrequency field on high-resolution nuclear magnetic resonance spectra. J Chem Phys 1962;37:85–113.

[155] Iino M. Dynamic properties of bound water studied through macroscopic water relaxations in concentrated protein solutions. BBA-Protein Struct M 1994;1208:81–88.

[156] Denisov VP, Halle B. Hydrogen exchange and protein hydration: The deuteron spin relaxation dispersions of bovine pancreatic trypsin inhibitor and ubiquitin. J Mol Biol 1995;245:698–709.

[157] Wolff SD, Balaban RS. NMR imaging of labile proton exchange. Journal of Magnetic Resonance (1969) 1990;86:164–169.

[158] Guivel-Scharen V, Sinnwell T, Wolff S, Balaban R. Detection of proton chemical exchange between metabolites and water in biological tissues. J Magn Reson 1998; 133:36–45.

[159] Ward K, Aletras A, Balaban R. A new class of contrast agents for MRI based on proton chemical exchange dependent saturation transfer (CEST). J Magn Reson 2000;143:79–87.

[160] Sherry AD, Woods M. Chemical exchange saturation transfer contrast agents for magnetic resonance imaging. Annu Rev Biomed Eng 2008;10:391–411.

[161] Zhang S, Merritt M, Woessner DE, Lenkinski RE, Sherry AD. PARACEST agents: modulating MRI contrast via water proton exchange. Acc Chem Res 2003;36:783–790.

[162] Aime S, Barge A, Delli Castelli D, Fedeli F, Mortillaro A, Nielsen FU, Terreno E. Paramagnetic Lanthanide(III) complexes as pH-sensitive chemical exchange saturation transfer (CEST) contrast agents for MRI applications. Magn Reson Med 2002;47:639–648.

[163] McConnell HM. Reaction rates by nuclear magnetic resonance. J Chem Phys 1958; 28:430–431.

[164] Wu X. Lineshape of magnetization transfer via cross relaxation. J Magn Reson 1991;94:186–190.

[165] Henkelman RM, Huang X, Xiang Q, Stanisz GJ, Swanson SD, Bronskill MJ. Quantitative interpretation of magnetization transfer. Magn Reson Med 1993;29:759–766.

[166] Zhou J, Wilson DA, Sun PZ, Klaus JA, Zijl PCv. Quantitative description of proton exchange processes between water and endogenous and exogenous agents for WEX, CEST, and APT experiments. Magn Reson Med 2004;51:945–952.

[167] Englander SW, Downer NW, Teitelbaum H. Hydrogen exchange. Annu Rev Biochem 1972;41:903–924.

[168] Mori S, Abeygunawardana C, Berg JM, van Zijl PCM. NMR study of rapidly exchanging backbone amide protons in staphylococcal nuclease and the correlation with structural and dynamic properties. J Am Chem Soc 1997;119:6844–6852.

[169] Covington AK, Robinson RA, Bates RG. The ionization constant of deuterium oxide from 5 to 50. J Phys Chem 1966;70:3820–3824.

[170] Dixon WT, Hancu I, Ratnakar SJ, Sherry AD, Lenkinski RE, Alsop DC. A multislice gradient echo pulse sequence for CEST imaging. Magn Reson Med 2010; 63:253–256.

[171] Mougin O, Coxon R, Pitiot A, Gowland P. Magnetization transfer phenomenon in the human brain at 7 T. Neuroimage 2010;49:272–281.

[172] Zhou J, Zijl PCv. Chemical exchange saturation transfer imaging and spectroscopy. Prog Nucl Mag Res Sp 2006;48:109–136.

[173] Sled JG, Pike G. Quantitative interpretation of magnetization transfer in spoiled gradient echo MRI sequences. J Magn Reson 2000;145:24–36.

[174] Ropele S, Stollberger R, Hartung H, Fazekas F. Estimation of magnetization transfer rates from PACE experiments with pulsed RF saturation. J Magn Reson Imaging 2000;12:749–756.

[175] Schmitt B, Zai M, Zhou J, Bachert P. Optimization of pulse train presaturation for CEST imaging in clinical scanners. Magn Reson Med 2011;65:1620–1629.

[176] Sun PZ, Benner T, Copen WA, Sorensen AG. Early experience of translating pH-weighted MRI to image human subjects at 3 Tesla. Stroke 2010;41:147–151.

[177] Scheidegger R, Vinogradov E, Alsop DC. Amide proton transfer imaging with improved robustness to magnetic field inhomogeneity and magnetization transfer asymmetry using saturation with frequency alternating RF irradiation. Magn Reson Med 2011;66:1275–1285.

[178] Sun PZ, Zhou J, Huang J, van Zijl P. Simplified quantitative description of amide proton transfer (APT) imaging during acute ischemia. Magn Reson Med 2007; 57:405–410.

Acknowledgement

I would like to thank my supervisor PD. Dr. Jochen Fiebach for providing me the opportunity to finish my thesis in his group, supporting me with delightful discussions and inspiring ideas, and encouraging me to establish contacts and explore new research topics.

I also would like express my appreciation to my mentor Prof. Dr. Harald Möller, who directs me with his profound insights, and supports me with constructive suggestions and abundant resources.

Dr. Valerij Kiselev is another expert that I would like to express my thanks. From him, I did not only learn professional knowledge, but also a strict attitude towards science. It was always a pleasure to talk with such a brilliant mind.

I would like to thank all colleagues in both working groups in Berlin and Leipzig. There were so many enjoyable moments with them to discuss, chat, have lunch, and drink coffee and tea.

I would like to say a "thank you" to my parents for being always supportive. I would not have started my PhD project without their encouragement.

Special thanks go to Marco. I can not appreciate more to have his love around me for every minute during my PhD project.

Lebenslauf

Mein Lebenslauf wird aus datenschutzrechtlichen Gründen in der elektronischen Version meiner Arbeit nicht veröffentlicht.

Publications

Journal Papers

Xu C, Schmidt WUH, Villringer K, Brunecker P, Kiselev VG, Gall P and Fiebach JB. Vessel size imaging reveals pathological changes of microvessel density and size in acute ischemia. Journal of Cerebral Blood Flow and Metabolism 2011;31:1687-1695.

Xu C, Schmidt WUH, Galinovic I, Villringer K, Hotter B, Ostwaldt A, Denisova N, Kellner E, Kiselev VG, Fiebach JB. The potential of microvessel density in prediction of infarct growth: a two-month experimental study in vessel size imaging. Cerebrovascular Diseases. 2012;33:303-309

Xu C, Kiselev VG, Möller HE, Fiebach JB. Dynamic hysteresis between gradient echo and spin echo attenuations in dynamic susceptibility contrast imaging. Magnetic Resonance in Medicine. 2012 (In Press)

Hotter B, Pittl S, Ebinger M, Oepen G, Jegzentis K, Kudo K, Rozanski M, Schmidt WU, Brunecker P, **Xu C**, Martus P, Endres M, Jungehülsing GJ, Villringer A, Fiebach JB. Prospective study on the mismatch concept in acute stroke patients within the first 24 h after symptom onset - 1000Plus study. BMC Neurology. 2009;9:60.

Conference Abstracts

Xu C, Labadie C, Pampel A, Fiebach JB, Möller HE. Development of a 3D CEST Pulse Sequence with Embedded Field Map and Low SAR for pH-Weighted Contrast in

Stroke Patients. The 20th Scientific Meeting of the International Society for Magnetic Resonance in Medicine (ISMRM) 2012, Melbourne, Australia. Poster.

Xu C, Kiselev VG, Brunecker P, Möller HE, Fiebach, JB. Analysis of loops formed by dynamic ratio of $\Delta R_{2GE}/\Delta R_{2SE}^{3/2}$ in DSC perfusion imaging. In 28th Scientific Meeting of the European Society for Magnetic Resonance in Medicine and Biology (ESMRMB) 2011, Leipzig, Germany. Oral.

Xu C, Kiselev VG, Brunecker P, Fiebach JB. Dynamic ratio $\Delta R_{2GE}/\Delta R_{2SE}^{3/2}$ in DSC perfusion imaging reveals the relative arterial and venous blood volume fraction. In 19th Annual Scientific Meeting of International Society for Magnetic Resonance in Medicine (ISMRM) 2011, Montreal, Canada. Oral.

Xu C, Schmidt W, Villringer K, Marzahn U, Galinovic I, Laubisch D, Krause T, Maul S, Steinicke R, Bahnemann M, Fiebach JB. Pathological microvascular morphology in ischemic penumbra revealed by vessel size imaging. In 21th European Stroke Conference 2011, Hamburg, Germany. Oral.

Xu C, Schmidt W, Brunecker P, Kiselev P, Gall P, Bodammer N, Fiebach JB.The assessment of vessel size index and its application in patients with ischemic stroke. 18th ISMRM-ESMRMB Joint Annual Scientific Meeting 2010, Stockholm, Sweden. Poster.

Xu C, Schmidt W. The assessment of vessel size imaging and its application in patients with ischemic stroke. In 91th Deutscher Röntgenkongress 2010, Berlin, Germany. Oral.

Xu C, Schmidt W, Brunecker P, Kunze C, Kiselev VG, Gall P, Fiebach JB. Vessel size imaging in patients with acute ischemic Stroke. In 20th European Stroke Conference 2010, Stockholm, Sweden. Oral.

Selbständigkeitserklärung

Ich, Chao Xu, erkläre, dass ich die vorgelegte Dissertation mit dem Thema: "Exploring Novel Magnetic Resonance Imaging Markers for Ischemic Stroke in the Application of Vessel Size Imaging and Amide Proton Transfer Imaging" selbst verfasst und keine anderen als die angegebenen Quellen und Hilfsmittel benutzt, ohne die (unzulässige) Hilfe Dritter verfasst und auch in Teilen keine Kopien anderer Arbeiten dargestellt habe.

Berlin, 19.04.2012 Chao Xu